SCIENCE CHINA
Technological Sciences

•Review•

May 2024 Vol.67 No.5: 1317–1363
https://doi.org/10.1007/s11431-023-2556-1

Application of ultrasonic fatigue technology in very-high-cycle fatigue testing of aviation gas turbine engine blade materials: A review

ZHAO JiuCheng[1,2,3], WAN Jie[1,2], ZHANG ShiZhong[2,3], YAN ChuLiang[2,4] & ZHAO HongWei[1,2,3*]

[1] *Key Laboratory of CNC Equipment Reliability Ministry of Education, Jilin University, Changchun 130025, China;*
[2] *School of Mechanical & Aerospace Engineering, Jilin University, Changchun 130025, China;*
[3] *Chongqing Research Institute of Jilin University, Chongqing, 401120, China;*
[4] *School of Aeronautic Science and Engineering, Beihang University, Beijing 102206, China*

Received June 6, 2023; accepted November 20, 2023; published online April 26, 2024

The need for very-high-cycle fatigue (VHCF) testing up to 10^{10} cycles of aviation gas turbine engine blade materials under combined mechanical loads and complex environments has encouraged the development of VHCF testing instrumentation and technology. This article begins with a comprehensive review of the existing available techniques that enable VHCF testing. Recent advances in ultrasonic fatigue testing (UFT) techniques are highlighted, containing their new capabilities and methods for single load, multiaxial load, variable amplitude fatigue, and combined cycle fatigue. New techniques for conducting UFT in high-temperature, humid environments, and corrosive environments are summarized. These developments in mechanical loading and environmental building techniques provide the possibility of laboratory construction for real service conditions of blade materials. New techniques that can be used for *in situ* monitoring of VHCF damage are summarized. Key issues in the UFT field are presented, and countermeasures are collated. Finally, the existing problems and future trends in the field are briefly described.

aviation gas turbine engine, blade materials, ultrasonic fatigue, very-high-cycle fatigue, high-temperature, complex stress, *in situ* testing

Citation: Zhao J C, Wan J, Zhang S Z, et al. Application of ultrasonic fatigue technology in very-high-cycle fatigue testing of aviation gas turbine engine blade materials: A review. Sci China Tech Sci, 2024, 67: 1317–1363, https://doi.org/10.1007/s11431-023-2556-1

1 Introduction

The rotor blade is the core component that determines the performance of an aero-engine, which is subjected to very tough service conditions [1–3]. As shown in Figure 1, the service conditions of the rotor blade include the huge centrifugal force caused by the high-speed rotation, the bending and torsional load that superimposed on the centrifugal force due to the high-speed air blowing, the high-frequency vibration (up to 1 kHz–2 kHz) attributed to the aerodynamic factors and mechanical reasons, the high-temperature environment caused by the fuel combustion, and the hot and humid environment, the corrosive environment, etc. The failure of the rotor blades is attributed to the coupling effect of the extreme environment and complex conditions mentioned above.

With the development of aviation science and technology, the failure mode of rotor blades has transformed from low-cycle fatigue (LCF) to high-cycle fatigue (HCF) and then to very-high-cycle fatigue (VHCF) [4]. In the 1950s, creep

*Corresponding author (email: hwzhao@jlu.edn.cn)

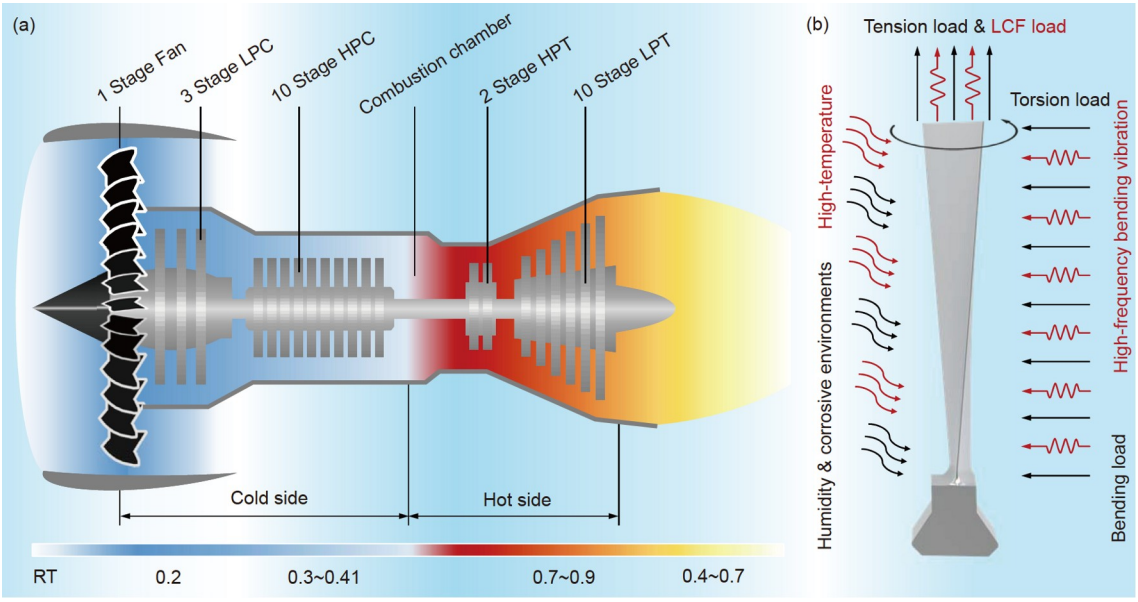

Figure 1 (a) Schematic diagram of the aviation gas turbine engine, where LPC and HPC represent the low-pressure compressor and high-pressure compressor, respectively, and HPT and LPT represent the high-pressure turbine and low-pressure turbine, respectively. 0–1 indicates the degree of approaching the maximum temperature. The highest temperature occurs in the combustion chamber at the front end of the high-pressure turbine; (b) schematic diagram of the service conditions of aviation gas turbine engine blades. The blades are subjected to combined tension-bending-torsion loads and high-frequency vibration loads, as well as a high-temperature/humidity environment and corrosive environment.

failure was the main cause of blade failure in rotor blades due to weak material preparation capability. In the 1970s, with the widespread use of creep-resistant alloys, LCF (fatigue life N_f of 10^2 to 10^5 cycles) became the main cause of blade failure [5]. With the development of the Engine Structural Integrity Program (ENSIP) [6] and the proposed damage tolerance design procedure [7], in the 1990s, HCF (fatigue life N_f of 10^5 to 10^7 cycles) was retained as the main mode of blade failure. As mentioned in a 1996 review by Cowles [8], the percentage of HCF failures in US military aviation gas turbine engine components was up to 24%. The service life of blades is up to 10^9–10^{12} cycles owing to the high-frequency and low-amplitude vibration caused by broadband airflow excitation [3]. However, the infinite life design criterion of 10^7 cycles as a safe life was still widely used in aircraft blade design until the 1990s [6]. Several important literature from 1983 to 1986 [9–12] found that the stress-life (S-N) curves still exhibit a decreasing trend at lifetimes greater than 10^7 cycles, revealing that there is no so-called infinite lifetime in metals. These significant findings indicated that the infinite life design criterion for blades was neither safe nor reliable. At this time, VHCF (fatigue life N_f greater than 10^7 cycles) began to enter the picture. In the late 2000s and early 2010s, ENSIP increased the life requirement of aircraft engine components from 10^7 cycles to 10^9 cycles [13]. In the last three decades, the proper assessment of the VHCF behavior of blade materials under extreme environments and complex conditions has become a hot issue of continuous concern for the majority of engineering designers.

From the viewpoint of time and cost, conducting VHCF studies with conventional techniques is impractical. The need for VHCF performance testing of blade materials has put forward the interest in the development of new testing techniques that are capable of loading to the 10^{10} cycles range. Up to now, there are about five available VHCF testing techniques. A rotational bending fatigue technique that can load multiple specimens at a time was proven to be available for VHCF testing [14]. Ultra-high frequency electrohydraulic resonant fatigue techniques with frequencies up to 1000 Hz have been developed [15] and show good prospects for application in the VHCF field. In addition, the electromagnetic resonant high-frequency technique [16], vibration-based fatigue technique [17], and UFT technique are also widely used in VHCF testing. When the advantages and disadvantages of the above techniques are compared, the UFT technique has become an irreplaceable technique for VHCF testing of blade materials due to its high efficiency and low energy consumption [18].

The ultrasonic fatigue testing (UFT) technique started in 1950, Mason and Baerwald [19] developed the UFT technique using the piezoelectric electrostriction principle, operating at frequencies of 15 to 22 kHz. In 1959, Neppairs [20] pioneered the utilization of the UFT technique for conducting fatigue performance tests on materials. After almost 70 years of development, UFT technology has made good progress. UFT machines with different functions have been developed to simulate the complex loads and extreme environments to which materials are subjected in blade components. UFT machines with integrated static loaders

have been developed to conduct axial tension-compression tests over a wide range of stress ratios. Three-point bending fatigue [21] and cantilever bending fatigue techniques [22,23] have been developed to simulate the high-frequency bending vibrations of blade materials experienced in service. The development of torsional fatigue [24] and fretting fatigue techniques [25] has further extended the capabilities of UFT technology. Biaxial bending fatigue [26], combined tension-torsion fatigue [27], and combined tension-bending fatigue techniques [28,29] have been developed in recent years to provide the possibility of fatigue performance testing of blade materials under complex stresses. In addition, Mayer et al. [30] and Zhao et al. [29] laboratory have developed variable amplitude (VA) and combined cyclic fatigue (CCF) machines capable of simulating unsteady airflow excitation (VA excitation) as well as LCF-HCF combined fatigue loads to which the blade materials are subjected. In terms of environmental testing, UFT machines have been developed for high-temperature [29,31], humidity environments [32,33], and corrosive environments [34] in succession. In this century, recent developments in UFT techniques have been reported in reviews by Bathias [25], Stanzl-Tschegg [18], and Mayer [35], including multiaxial fatigue, VA fatigue, fatigue in different environments, and VHCF damage monitoring methods.

This review focuses on reporting the application of UFT technology in the VHCF testing of aviation gas turbine engine blade materials, which is one of the most critical application fields of UFT technology. Following this introduction, the second part of this review compares viable testing techniques in the VHCF testing field for blade materials and highlights the superiority of the UFT technique. Subsequently, this review provides an overview of recent advances in UFT technology in terms of mechanical loading, environmental building, and *in situ* monitoring, as shown in Figure 2. New methods achieved in UFT for constant amplitude fatigue are reported in detail, including single load fatigue and multiaxial fatigue. VA loading and combined cyclic fatigue (CCF) techniques are presented. Then, UFT techniques in the environment are reported, including high-temperature, humidity environment, and corrosive environments. *In situ* testing techniques for VHCF damage, both visualized and non-visualized, are presented. Furthermore, three existing key issues and countermeasures in UFT

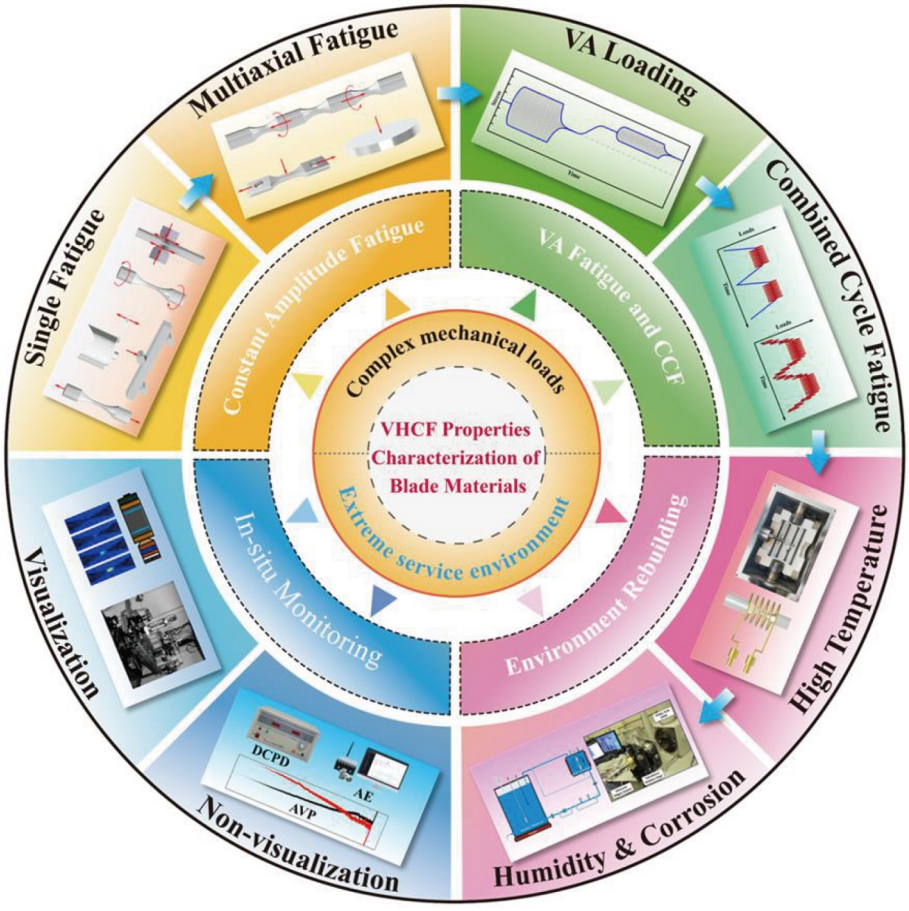

Figure 2 The recent advances of UFT technology in mechanical loading, environmental rebuilding, and *in situ* monitoring are outlined. Where VA denotes variable amplitude, CCF denotes combined cycle fatigue, DCPD denotes direct current voltage drop, AE denotes acoustic emission, and AVP denotes vibration properties analysis.

techniques are presented. Finally, the review is summarized and a brief outlook is presented. It is hoped that this review will provide some valuable technical guidance for VHCF performance testing of aero-engine blades and other core field components.

2 Comparison of VHCF testing techniques

2.1 Rotation bending fatigue

The rotating bending fatigue (RBF) machine was the first fatigue machine in the world. It was developed by German Wöhler [36] in 1858, and played an important role in the study of the fatigue performance of railroad axles from 1858 to 1870. In 1983, Naito et al. [9] discovered the stepped S-N curve as well as the "fish-eye" feature of carburized steel by RBF machine, which laid the beginning of VHCF research. The advantages of RBF machines, such as low price, simple structure, maintenance-free, and low energy consumption, have led to a renewed interest in the VHCF testing of materials. A series of important studies in the VHCF field by Shiozawa's group [37–41] and Sakai's group [9,10,42–45] from the 1980s to the present have been conducted based on RBF machines.

Conventional RBF machines generally consist of a rotating unit, loading unit, and cooling unit, and can also be integrated with high-temperature environment [46] and corrosive environment [47] systems as desired. As shown in Figure 3, the specimen is mounted as a cantilever or four-point type, and a constant bending moment is generated by hanging weights. The specimen is driven by the rotating unit to generate the bending moment with sinusoidal variation at high speed, which enables the purpose of rotational bending loading. The test is conducted until the specimen breaks or reaches the run-out cycle to trigger the stop signal and automatic stop. The stress in the specimen can be derived from theoretical calculations or determined by applying strain gauges [48]. It is worth stating that an RBF machine has been developed to test 48 specimens simultaneously [14], which greatly improves the efficiency of VHCF data acquisition.

Inevitably, there are some disadvantages to this type of machine. First, RBF machines provide a single-loading mode. Furthermore, its unique loading method puts the specimen in a dynamic, unbalanced state, resulting in unavoidable vibrations, which restricts the upper limit of the motor speed. Typically, the rotation speed does not exceed 12,000 r min^{-1}. Therefore, the frequency range is limited to 0.1 to 200 Hz. Even with a test frequency of 200 Hz, it will take 58 days to realize the Giga-cycle fatigue (10^9 cycles) test. In addition, cracks extend into the specimen when conducting rotational bending tests, and contacting the rotating specimen is difficult, which makes either optical or conventional electrical methods for crack detection difficult to realize. Therefore, some adaptations had to be made to the existing machine to achieve the above-mentioned purpose. These drawbacks limit, to some extent, their application in VHCF testing of blade materials.

2.2 Resonant high-frequency fatigue

VHCF or even Giga-cycle fatigue (GCF) testing using conventional test techniques is extremely challenging, and the huge costs associated with months or even years of testing time are unacceptable. The requirement for high frequency and low energy consumption has stimulated the development of resonant high-frequency fatigue testing technology. Resonant fatigue testing techniques have existed for more than a century and a brief review of them is given by Nicholas [4] in his monograph. Based on experience, the author divides resonant fatigue testing techniques into three categories [49]. (1) Type I: The machine and the specimen form a mass/spring resonance system. The specimen is considered only as an elastic part, not functioning at its natural frequency. Such as electromagnetic and electro-hydraulic resonance fatigue machines. (2) Type II: The machines are not in resonance, but they provide vibrating loads to drive specially designed specimens into high-frequency resonance modes, such as non-contact resonant fatigue machines (acoustically driven

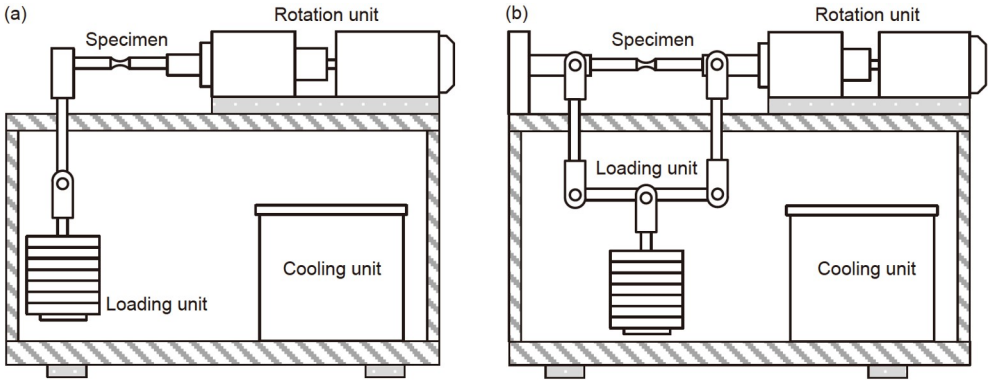

Figure 3 Rotating bending fatigue machine. (a) Cantilever bending loading method; (b) four-point bending loading method.

[50] or electrostatically driven [51,52]) and vibration-based fatigue machines. (3) Type Ⅲ: The machine and specimen are properly designed to allow working close to the same natural frequency, most typically an ultrasonic fatigue testing (UFT) machine.

2.2.1 Electromagnetic and electrohydraulic resonance fatigue

The technique of driving the combination of machine/sample into resonance by magnetic excitation dates back to before the Second World War [53]. After more than 100 years of development, there are now mature commercial electromagnetic resonant fatigue machines that are capable of stable operation in the frequency range of 40 to 300 Hz. A schematic diagram of a common electromagnetic resonance fatigue machine is shown in Figure 4(a). The specimen acts as an elastic element and forms a spring/mass resonance system with the machine, as shown in Figure 4(b). The excitation magnet based on the electromagnetic resonance principle generates a periodic electromagnetic excitation force with a certain frequency and intensity, which acts on the spring/mass resonance system. When the frequency of the excitation force is the same as the system's frequency, the system resonates and thus enlarges the weak amplitude to reach the experimental purpose. The mechanism consisting of preload crosshead, worm, and preload ring is driven by a DC motor to preload the specimen to achieve fatigue test under arbitrary stress ratio R.

Milošević et al. [54] developed a high-frequency tension-compression fatigue machine capable of stable operation at close to 834 Hz. The machine consists of the mass, hydraulic sleeve, base, and specimen. Highly rigid mounting of the specimen using a hydraulic sleeve. The machine constitutes a spring/mass system stimulated by an electrodynamic vibrator to generate high-frequency tension/compression vibration patterns. In the resonance case, the excitation acceleration signal is enlarged several times. Therefore, it is possible to construct high stresses in the gauge-section of the specimen. Nicholas [16] reported two fatigue machines based on the electromagnetic resonance principle. The first machine applied a static load with a cylinder mounted in a rigid test frame and provided high-frequency oscillatory excitation by an electrodynamic shaker. The second machine applies the mean stress through a conventional hydraulic cylinder and provides high-frequency loads using magnetostrictive high-frequency actuators. A very large mass is used as an isolation block, which is very compliant for low-frequency or static mean loads but is stiff for high-frequency loads. Both of the above techniques have proven to be suitable for VHCF testing.

It is worth stating that the above machines can only provide VHCF testing in a single load mode. A series of improvements have been made to such machines to enable the testing of blade materials [55,56], blade-like specimens [57], or full-size blade components [58–64] under combined cycle fatigue (CCF). These new machines are based on the electromagnetic resonance principle and have in common that: (1) An electronic or hydraulic drive is added to apply the periodic variable tension force. (2) Increased induction coils create a high-temperature environment locally. (3) Blade

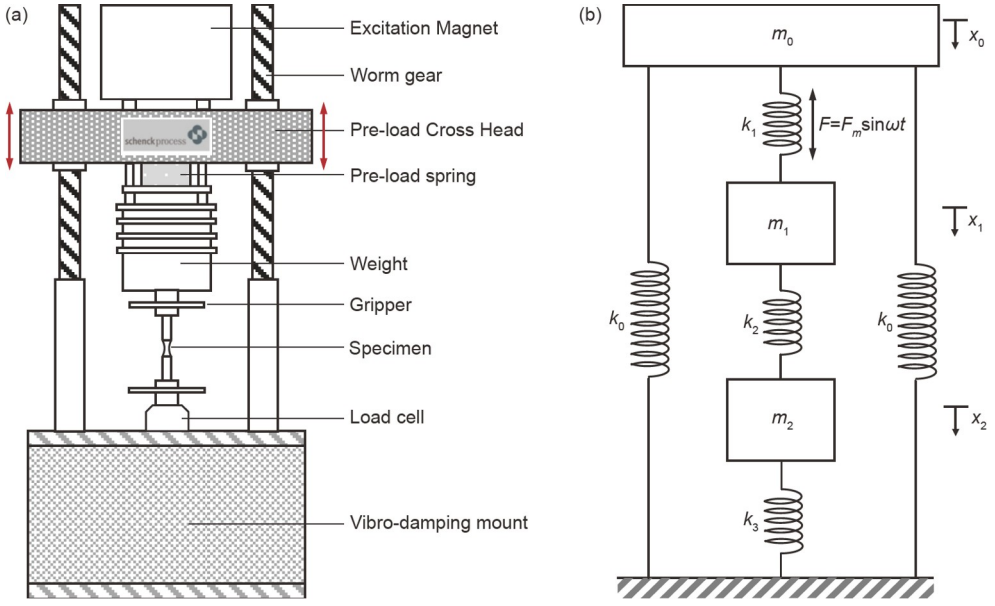

Figure 4 (Color online) (a) Schematic diagram of an electromagnetic resonant fatigue machine and (b) the corresponding mass/spring resonant system. Where m_0 denotes the reference mass of the frame and shaker, m_1 denotes the reference mass of the weights, and m_2 denotes the reference mass of the specimen and sensor. k_0 denotes the frame stiffness, k_1 denotes the stiffness of the preload ring, k_2 denotes the stiffness of the specimen, and k_3 denotes the stiffness of the sensor.

material specimens, blade-like specimens, or full-size blades are clamped in specially designed fixtures and excited by the shaker to generate high-frequency bending vibrations. These new machines are capable of imposing typical CCF blocks [56], as well as the CCF test blocks as specified in the European PREMCCY (Predictive Methods for Combined Cycle Fatigue in Gas Turbine Blades) program [65]. It should be noted, however, that these machines all have two orthogonal loading axes. When conducting such tests, the slenderness ratio of the specimen needs to be carefully designed to avoid interference with the load in the tensile direction due to the coupling effect of the load during the bending excitation [2].

In summary, the biggest advantage of these machines is their low energy consumption, which is only 0.5 kW. In addition, these machines are capable of providing rich load types such as tension, bending, and torsion. Moreover, the advantage of a resonant machine for which the specimen is part of the system is that the spring constant of the specimen changes when fatigue damage accumulates to a certain level, thus bringing the system out of resonance, providing the possibility of checking the specimen before catastrophic fracture [66]. However, the relatively low frequency limits its application in VHCF testing of blade materials.

The first electrohydraulic resonance fatigue (EHRF) machine dates back to 1957. EHRF machines generally contain core components such as servo actuators, servo valves, load cells, and displacement sensors. The high-pressure fluid from the pump station flows into the electro-hydraulic servo valve, which controls the input and output of hydraulic fluid in the two chambers of the hydraulic cylinder piston to generate cyclic motion for fatigue loading purposes. The frequency of these machines is typically 20 Hz and up to 50 Hz. Morgan and Milligan [15] developed an EHRF machine capable of stable operation at 1000 Hz in 1997. A schematic diagram of this type of machine is shown in Figure 5. These newer machines use voice coil servo valves instead of conventional servo valves. The voice coil servo valve uses an electric pilot stage that is driven in the same way as an audio speaker. In addition to good durability, these valves offer an excellent high-frequency response and higher flow rates for high-frequency loading purposes. Additionally, the need for high-frequency testing has led to the adoption of high-frequency controllers and hydrostatic support hydraulic cylinders for these machines. To improve the dynamic stiffness of the load frame to avoid resonance, these machines feature a lower base, shorter posts and forced crossheads, and additional tie bars at the top of the posts compared with conventional 250 kN frames. As a result, an amplitude of ±0.1 mm at 1000 Hz and a dynamic load of 20 kN can be achieved.

Zimmermann and Christ [67] reported the power response and control accuracy characteristics of these high-frequency

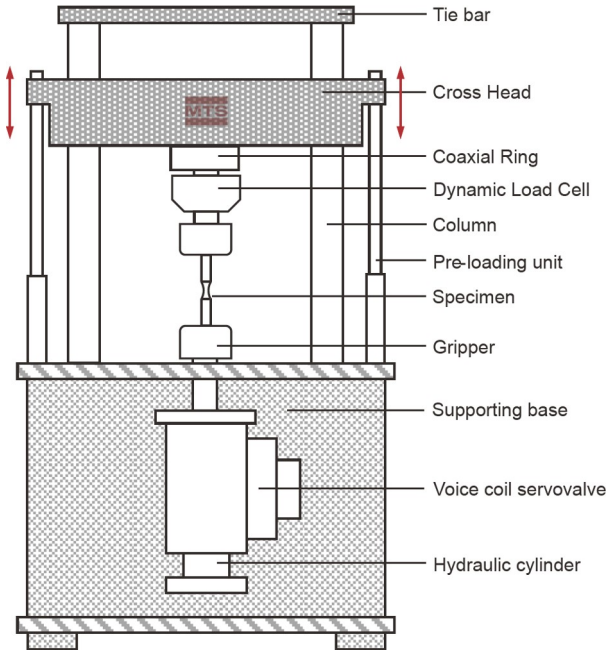

Figure 5 (Color online) 1 kHz electrohydraulic fatigue testing system.

machines. Constant amplitude tests conducted at 100 Hz steps for aluminum and duplex steels achieved the best control accuracy at 760 Hz. Deviations in this frequency range were found to be less than 3% of the nominal amplitude value. A series of studies by Ritchie et al. [68–70] further demonstrated the effectiveness of such machines in the VHCF testing field. However, high energy consumption and poor maintainability have restricted the widespread use of such machines in VHCF testing.

2.2.2 Vibration-based fatigue

The non-contact resonant fatigue test machine in Type II provides small loads and is only suitable for tiny-size specimens. This section of the article focuses on the most widely used test technique in VHCF testing of blade materials - vibration-based fatigue (VBF). The concept of VBF was first proposed by George et al. [17] in 2004. VBF is a method for high-frequency fatigue testing by exciting specially designed specimens to resonance through a shaker, allowing multiple vibration patterns and complex stress states by selecting resonance modes and optimizing specimen geometry [17]. Figure 6 shows a schematic of the VBF machine. Conducting a VBF test involves three key steps. (1) Topology optimization design based on finite element analysis (FEA) to ensure that the specimen achieves the desired frequency, vibration pattern, and stress state (uniaxial stress or biaxial stress, etc.). (2) Strain and laser velocity or displacement calibration process using strain gauges and laser vibrometers. Establishing a relationship between strain in the fatigue region and the velocity/displacement of the calibrated laser position allows for more precise control of the stress or strain

vibration amplitude in the specimen during the fatigue test. It is worth stating that in VBF testing, the digital image correlation (DIC) does not accumulate damage during strain measurement because it is non-contact compared with strain gauges. Consequently, Hill [71] used DIC for the construction of strain-velocity calibration curves as an alternative to strain gauges. (3) Determination of failure criterion. In VBF testing, the specimen does not exhibit catastrophic failure, even if there is a crack. Therefore, it is critical to determine the failure criterion of the specimen. Failure is generally determined by monitoring the frequency drop because crack initiation and propagation change the stiffness of the specimen, which affects its natural frequency. Table 1 summarizes some of the commonly used frequency drop thresholds when conducting VBF tests for the reader's reference.

Depending on the shape of the specimen, the VBF can be simply divided into two categories. In the first category, the specimen is a cantilevered square plate or a cantilevered variable section plate. In the method involving cantilevered square plates, a mode commonly referred to as the "double-stripe" mode, which generates uniaxial bending stresses of 1600 Hz along the free edge of the plate, is in use, and is suitable for VHCF testing [17,80,81]. Furman et al. [80] presented a method for optimizing the dimensions of such square plate specimens (called standard bending specimens) in detail in a recent paper. To reduce the material cost, Bruns et al. [72] proposed a hybrid Insert-Plate system. An insert was used at the edge of the standard bending specimen without changing its dimensions and vibration pattern. The maximum stress occurs in the insert. The insert fails at each fatigue test, while the plate can be reused. The use of this idea significantly reduces the material cost compared with standard bending specimens, but there is a certain degree of reduction in test frequency. In the second category, the specimen is a slender cantilever beam. The test is based on the first or second-order bending vibration of the specimen. Compared with higher-order vibration patterns, first or second-order vibration patterns are easier to conduct in fatigue testing. Yun et al. [82] proposed a specimen with a rectangular slender beam and a rounded chamfer near the clamped

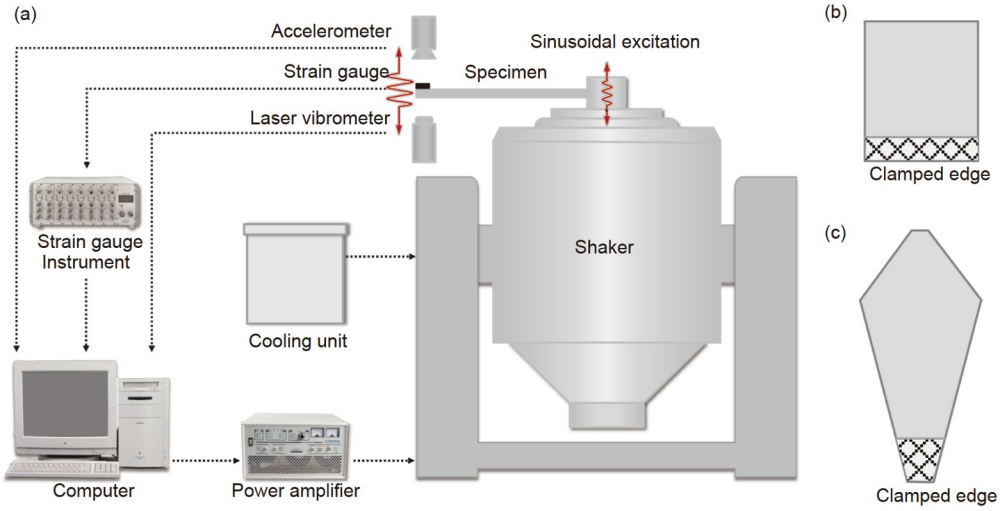

Figure 6 (Color online) (a) Schematic diagram of the vibration-based fatigue test setup. Schematic diagram of specimen shapes for (b) uniaxial and (c) biaxial fatigue.

Table 1 Frequency drop threshold in vibration-based fatigue

Test methods	Specimen shape	Materials	Test frequency (Hz)	Frequency drop Threshold (%)	Reference
Vibration-based fatigue (VBF)	Square plate	Steel/Al 6061-T6/Ti-6Al-4V	1600	0.5	George et al. [17] (2004)
	Hybrid insert-plate system	Al 6061-T6	1080–1100	0.1	Bruns et al. [72] (2015)
	Annular disc	Ti-6Al-4V	210	5	Xu et al. [73] (2017)
	Square plate	Al 2024-T3	300–400	5	Hu et al. [74] (2014)
	Cantilever rectangular plate	SLM/WBD Ti-6Al-4V	800	2	Ellyson et al. [75,76] (2017)
	Y-shaped specimen	AS8U3	700–800	1.2–2.5	Česnik et al. [77] (2012), Capponi et al. [78] (2017)
	Irregular sheet specimen	Ti-6Al-4V	258	2.01	Xu et al. [79] (2018)

end, with the maximum stress occurring at the rounded chamfer near the clamped end. A test frequency of about 700 Hz can be achieved with this type of specimen. To keep the maximum stress away from the clamped end, Ellyson et al. [75,76] proposed a cantilevered rectangular beam specimen with a shallow notch in 2017. A test frequency of up to 800 Hz can be achieved with this specimen. The specimen proposed in HB 5277-2021 (Vibration fatigue test method of engine blades and materials) can achieve the same purpose, but only at a frequency of 240 Hz. In 2022, Xu et al. [83] proposed a novel specimen capable of reaching a bending vibration frequency of 1700 Hz in the test. The shape and lengthwise dimensions of the specimen are similar to those proposed by Ellyson et al. [75,76] but with two important improvements. The thickness of the specimen is thicker and three through-holes are provided at the end of the specimen, which further increases the resonant frequency of the specimen.

Conducting VBF tests generates uniaxial and biaxial stress data in full reverse bending mode. Moreover, the test frequency of several kHz perfectly covers the vibration frequency of the blade during the real service. A further advantage is the ability to identify the initial fatigue crack within the specimen by the observed change in resonant frequency. Therefore, the VBF machine is widely used for VHCF performance testing of blade materials, blade-like specimens, and full-size blades.

2.2.3 Ultrasonic fatigue

The ultrasonic fatigue testing (UFT) technique was first developed by Mason in 1950 [19]. The technique was first applied to determine the stress-life curve of materials by Neppiras [20] in 1959. The technique was first applied to fatigue crack propagation tests by Mitsche et al. [84] in 1973 and was able to measure the crack propagation rate down to 10–12 m per cycle. After more than 70 years of development, the laboratories of Willertz (USA), Stanzl (Austria), Bathias (France), Ishii (Japan), Puskar (Slovakia), Hong (China), and Wang (China) are now the leading laboratories in this field.

Different from any of the above-mentioned loading methods, the UFT machine is tested using the propagation of mechanical waves in a solid [25]. In the vibration system consisting of the booster, horn, and UF specimen, the vibration frequency is adjusted to the resonance point to form a time-invariant resonance system. In axial tensile UF, for example, the longitudinal wave propagates in the ultrasonic system in a tensile-compressive manner, amplified by the booster and horn to reach the maximum stress amplitude in the specimen center for cyclic loading tests. Up to now, the development of UFT machines has been relatively mature. Conventional machines generally contain the following parts.

(1) Ultrasonic generator. The ultrasonic generator with a power of 5–500 W converts the electrical signal of 50 Hz into a high-frequency electrical signal of 20 kHz (or even 40 kHz), which mainly contains the following functions. (i) The electrical signal size (1 to 10 V) can be varied by a voltage regulator to change the vibration amplitude. Both constant amplitude (CA) loading and VA loading procedures are allowed. (ii) Set pulse loading time and pause time that allows executing pulse-pause loading procedure. (iii) Control of resonant frequency. The excitation frequency is matched with the actual frequency of the ultrasonic load chain. A phase-locked loop circuit and a voltage-controlled oscillator are used to keep the phase shift of the displacement signal of the specimen and the ultrasonic power signal constant so that the cyclic frequency and the actual resonant frequency coincide better than ±0.1 Hz. It can also monitor the crack initiation of the specimen through the change in cycle frequency and automatically terminate the test when the cycle frequency exceeds the frequency limit.

(2) Ultrasonic transducer. Based on the principle of piezoelectric electrostriction, a weak electrical signal of 20 kHz is converted into a mechanical wave of the same frequency (usually a longitudinal or shear wave).

(3) Booster and horn. Usually, a Ti or Al-7075-T6 solid variable cross-section cylindrical rod amplifies the weak mechanical vibrations at the output of the transducer with an amplification ratio of typically 5 to 10. More details about the design of the booster and horn can be found in ref. [85].

(4) UF specimen. In the case of an axial tension UF specimen, the specimen is an axisymmetric cylindrical rod or rectangular piece. Typically, the cross-section of the specimen is reduced at the center to increase the ultrasonic waves passing through it thus reaching a higher stress amplitude. More details about UF specimen design can be found in refs. [86,87].

(5) Measurement and closed-loop control unit. It is worth noting that the cyclic stress amplitude in the UFT cannot be measured directly. Generally, a laser doppler vibrometer is used to measure the end displacement of the UF specimen, and a dynamic strain gauge is used to determine the strain amplitude in the gauge section. The stress amplitude is further determined according to Hooke's law. Once the displacement amplitude-stress relationship is established, the test can be conducted.

In addition to the basic components described above, additional devices can be configured as desired. For example, static and low-frequency loading devices, specimen cooling devices, environmental construction devices, and damage *in situ* monitoring devices, etc. More detailed information will be presented later in the article. Readers interested in the development of such machines will find more information in the literature [88] or Bathias' book [89].

2.3 Comparison of VHCF testing techniques

The significant need for accurate assessment of the VHCF performance of blade materials makes the ideal VHCF testing technique should meet a series of criteria, i.e., higher loading frequency, good maintainability, low energy consumption, load pattern richness, testing in the environment, *in situ* monitoring of damage, testing of blade/blade-like specimens, specimen temperature rise, standardization level, etc. Table 2 and Figure 7 compare the characteristics of different VHCF testing techniques.

To make an accurate comparison of the different VHCF testing techniques, metrics to evaluate the above-mentioned criteria were developed. Since the blade fatigue life falls into the VHCF regime (up to 10^{10} cycles), the test frequency becomes one of the most critical criteria. Test frequency below 100 Hz is considered poor, and frequencies between 100 and 300 Hz, 300 Hz to thousands of Hz, and greater than 20 kHz are considered fair, good, and excellent, respectively. For example, to realize 10^{10} cycles of VHCF testing, it would take 5787, 1157, 116, and 5.8 days at frequencies of 20, 100, 1000, and 20 kHz, respectively. Another remarkable criterion is the maintenance of the tested machines. Those running maintenance-free are considered excellent; those requiring occasional maintenance and frequent maintenance are considered good and fair, respectively, while those requiring constant maintenance are considered poor. In addition, the energy consumption of the test machine is also critical. Energy consumption is reflected as a combination of test power and test time. Technologies based on hydraulic drive methods and forced vibration are considered poor, electromagnetic resonance high-frequency testing technologies are considered average, vibration-based testing technologies are considered good, and ultrasonic technologies based on piezoelectric electrostrictive resonance are considered excellent.

The complex loads and extreme environments during the service of blade materials raise high requirements for the richness of load patterns and the integration of environmental construction devices for VHCF testing technology. Test techniques that can achieve multiple loads-multiaxial loads are considered excellent, those capable of only multiaxial loads and only multiple loads are considered good and fair, respectively, and those capable of only a single load are considered poor. Those integrating multiple environment-building devices are considered excellent, those integrating one or two environment-building devices are considered good, and those hardly integrating environment-building devices are considered poor.

The requirements for the feasibility of *in situ* monitoring during VHCF testing are presented for the monitoring of specimen damage and failure during the test. Those integrating multiple *in situ* monitoring methods are considered excellent, those that can integrate one or two *in situ* monitoring methods are considered average, and those that cannot integrate with situ monitoring methods are considered poor. The ability to conduct blade/blade-like specimen testing is also an important criterion. The ability to conduct full-scale blade testing is considered excellent, the ability to conduct scaled-down model testing is considered good, the ability to conduct blade-like specimen testing is considered average, and the ability to conduct material testing only is considered poor. Specimen temperature rise is a major challenge in high-frequency/ultra-high-frequency testing. Higher temperature rise may lead to deviation of test results or even experimental failure. The evaluation of the specimen temperature rise is referred to the criteria provided by Shabani et al. [90], i.e., a temperature rise greater than 20°C under cooling conditions is considered poor, a temperature rise less than 20°C under cooling conditions is considered fair, a temperature rise greater than 20°C without cooling conditions is considered good, and a temperature rise less than 20°C without cooling conditions is considered excellent. Whether standards have been established on testing techniques and test methods is also a comparable criterion, which, to a certain extent, reflects the perfection of the technology. Those that already have standards are considered excellent, and those without standards are considered poor.

Table 2 Comparison of VHCF testing techniques (in VHCF testing of blade materials)[a)]

VHCF testing techniques	Test frequency	Maintenance	Energy consumption	Test mode	Testing in the environment	*In situ* Monitoring	Blade component testing	Temperature rise of the specimen	Standardization
Rotation bending fatigue	★	★★★★	★	★	★★★	★	★	★★★★	★★★★
Electro-magnetic resonance fatigue	★★	★★	★★★	★★	★★★	★★★	★★★	★★★	★★★★
Electro-hydraulic resonance fatigue	★★	★	★	★★	★★★	★★★	★★★	★★★★	★★★★
Vibration-based fatigue (Shaker)	★★★	★★	★★★	★★★★	★★	★	★★★★	★★★	★★★★
Ultrasonic fatigue	★★★★	★★★★	★★★★	★★★★	★★★★	★★★★	★	★	★★

a) ★ means *Poor*, ★★ means *Average*, ★★★ means *Good*, ★★★★ means *Excellent*.

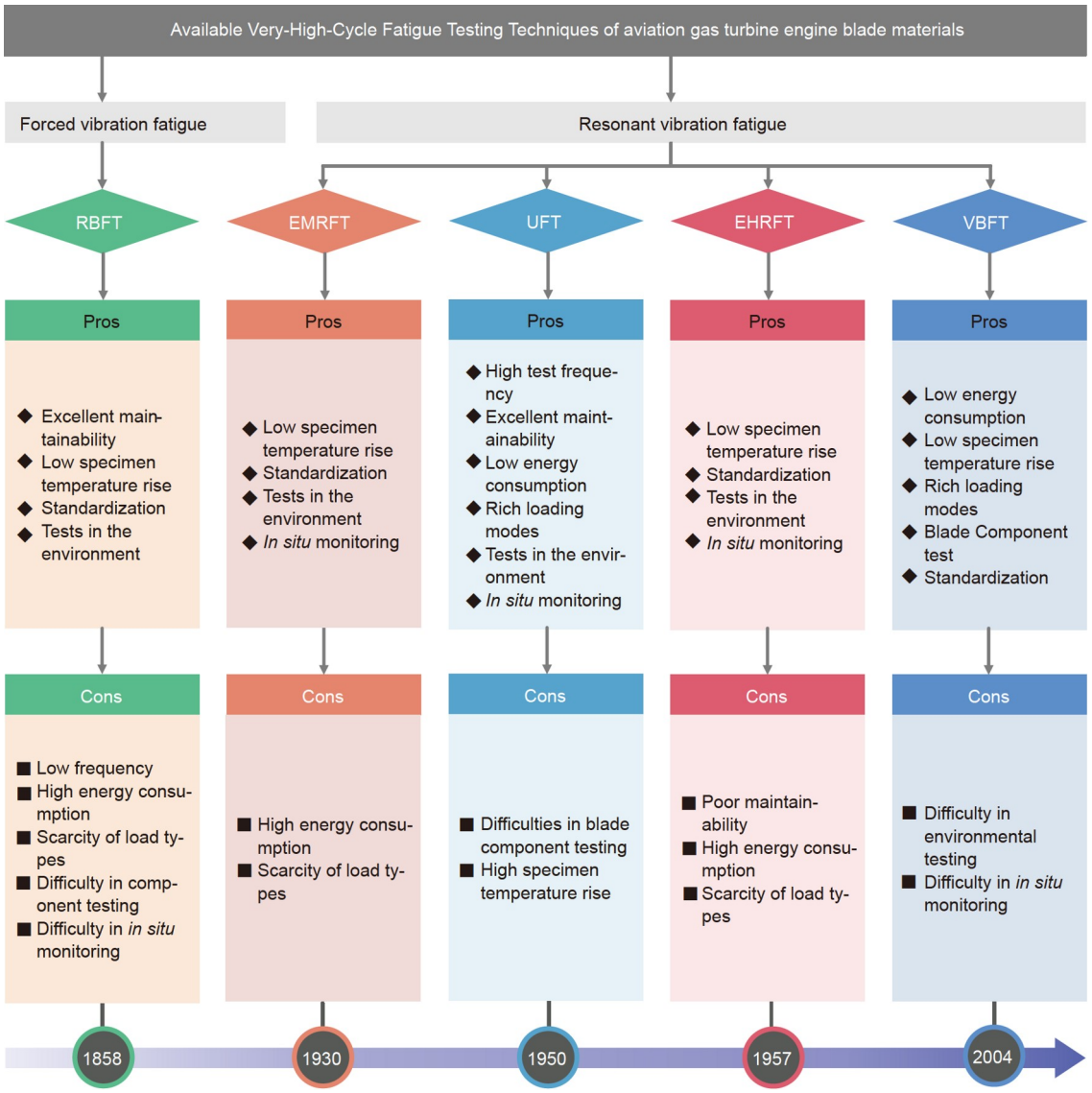

Figure 7 (Color online) Advantages and disadvantages of different VHCF testing techniques. RBFT indicates rotational bending fatigue test, EMRFT indicates electromagnetic resonance fatigue test, EHRFT indicates electrohydraulic resonance fatigue test, VBFT indicates vibration-based fatigue test, and UFT indicates ultrasonic fatigue test.

3 Ultrasonic fatigue testing techniques under complex loads

In the past three decades, the need for VHCF testing of blade materials under complex loads has promoted the rapid development of UFT technology, which is no longer limited to axial tension-compression. UFT techniques have been established with rich load types, such as axial tension-tension, three-point bending, cantilever bending, torsion, and fretting fatigue. In addition, preliminary progress has been made in multiaxial UFT techniques in recent years.

3.1 Axial tensile fatigue

3.1.1 Specimen design theory

Axial tension UFT is conducted based on the transfer of one-dimensional longitudinal waves [89]. Axial tension UF specimens are axially symmetric cylindrical rods or rectangular pieces with reduced cross sections in the gauge section to reach higher stress levels. Figure 8 summarizes the geometry of several existing axial tension UF specimens. To resonate at ultrasonic frequencies, the specimen dimensions need to be carefully designed to create a mechanical wave standing in the lengthwise direction. Taking the most common hourglass-type UF specimen as an example, according to the longitudinal free vibration theory of a one-dimensional slender rod, the free vibration equation of the specimen is [86,89]

$$\frac{\partial^2 U(x,t)}{\partial x^2}+\frac{1}{A(x)}\frac{\mathrm{d}A(x)}{\mathrm{d}x}\frac{\partial U(x,t)}{\partial x}+k^2U(x,t)=0, \tag{1}$$

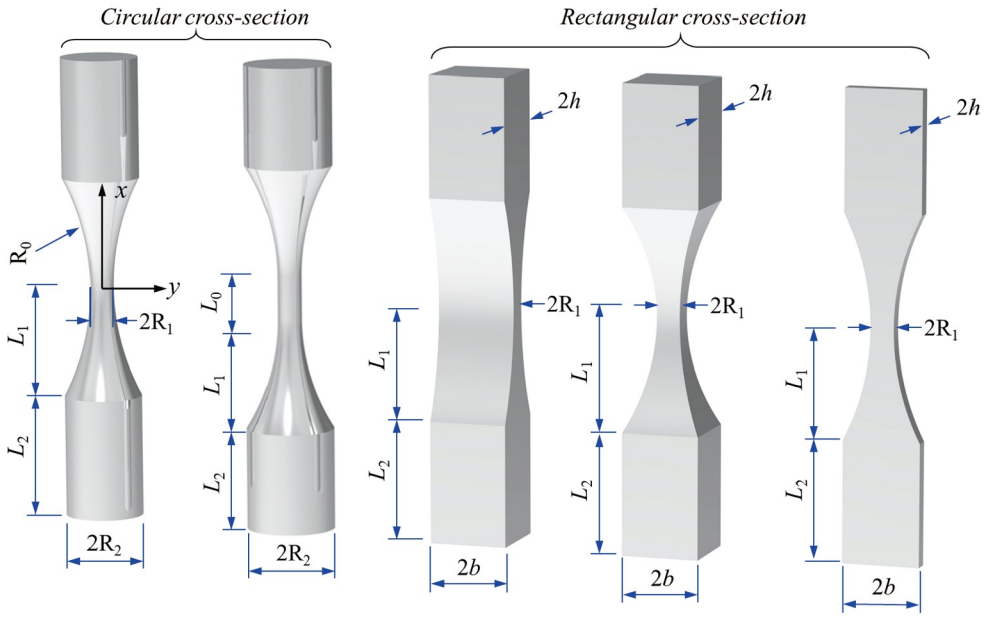

Figure 8 (Color online) Three-dimensional view of a typical axial tension ultrasonic specimen.

where $U(x,t)$ is the longitudinal excitation displacement, $U(x,t)=U(x)\sin(2\pi ft)$. $A(x)$ is the cross-sectional area of the specimen at position x. k is the material constant, $k=2\pi f\sqrt{\rho/E}$, f is the resonant frequency, ρ is the density of the specimen material, and E is Young's modulus. For hourglass specimens, the end is cylindrical and the profile of the gauge section is catenary. The catenary equation is $y=a\cosh(\alpha x)$. When $x=0$, $y=R_1$, and when $x=L_1$, $y=R_2$. Therefore, the catenary equation is determined as $y=R_1\cosh(\alpha x)$, $\alpha=\text{arch}(R_2/R_1)/L_1$. The equation for the cross-sectional area of the specimen is

$$\begin{cases} A(x)=\pi R_2^2, & L_1 \quad |x| \quad L_1+L_2, \\ A(x)=\pi R_1^2\cosh^2(\alpha x), & |x| \quad L_1. \end{cases} \tag{2}$$

Solving eq. (1) yields the longitudinal free vibration displacement of the specimen as

$$\begin{cases} U(x)=A_0\cos[k(L-x)], & L_1 \quad |x| \quad L_1+L_2, \\ U(x)=A_0\varphi(L_1,L_2)\dfrac{\sinh(\beta x)}{\cosh(\alpha x)}, & |x| \quad L_1. \end{cases} \tag{3}$$

The resonant length L_2 of the specimen is

$$L_2=\frac{1}{k}\arctan\left\{\frac{1}{k}\left[\frac{\beta}{\tanh(\beta L_1)}-\alpha\tanh(\alpha L_1)\right]\right\}, \tag{4}$$

where $\alpha=\text{arch}(R_2/R_1)/L_1$, $\beta=(\alpha^2-k^2)^{1/2}$. The strain distribution $\varepsilon(x)$ in the gauge section of the specimen can be expressed as

$$\varepsilon(x)=\frac{\partial U(x)}{\partial x}=A_0\varphi(L_1,L_2) \cdot\frac{\beta\cosh(\beta x)\cosh(\alpha x)-\alpha\sinh(\beta x)\sinh(\alpha x)}{\cosh^2(\alpha x)}, \tag{5}$$

where $\varphi(L_1, L_2)=[\cos(kL_2)\cosh(\alpha L_1)/\sinh(\beta L_1)]$. The maximum strain $\varepsilon_{\max}$ and the maximum stress $\sigma_{\max}$ appear in the center gauge section of the specimen, respectively,

$$\varepsilon_{\max}=A_0\beta\varphi(L_1,L_2), \tag{6}$$

$$\sigma_{\max}=EA_0\beta\varphi(L_1,L_2). \tag{7}$$

3.1.2 *Axial tension UFT instrument*

Axial tension UFT machines are very widely used in VHCF testing of blade materials, and they provide more conservative fatigue data than other load types. The original axial tension UFT machine contained an ultrasonic transducer, booster, horn, and a computer control system. The UF specimen is fixed at one end at the lower end of the horn and the other end is free. This configuration is capable of achieving axial tension fatigue in fully reversed mode. Improvements have been made to this type of machine to take the average stress effects into account and to construct a Goodman curve for the material. As shown in Figure 9, an additional booster and horn are connected at the lower end of the specimen, which enables the addition of a displacement node in the load chain. The ultrasonic components are connected to the tensile tester via displacement nodes at the upper and lower booster for superimposing average stress with sinusoidal ultrasonic vibration loads.

3.2 Three-point bending fatigue

3.2.1 *Specimen design theory*

Different from the axial tension UFT, the three-point bending UFT works based on the principle of transverse bending vibration [21]. For the rectangular specimen shown in Figure 10, the micro-section at position x is selected for force analysis in the case of transverse forced vibration.

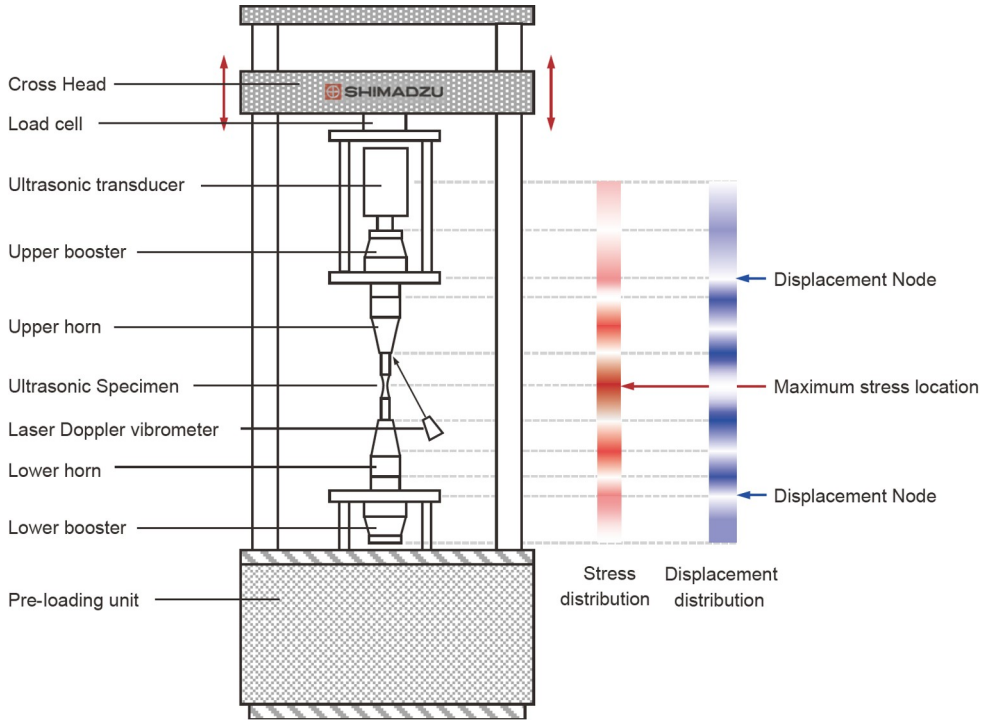

Figure 9 (Color online) Axial tension UFT machines. The red band indicates the stress distribution and the blue band indicates the displacement distribution.

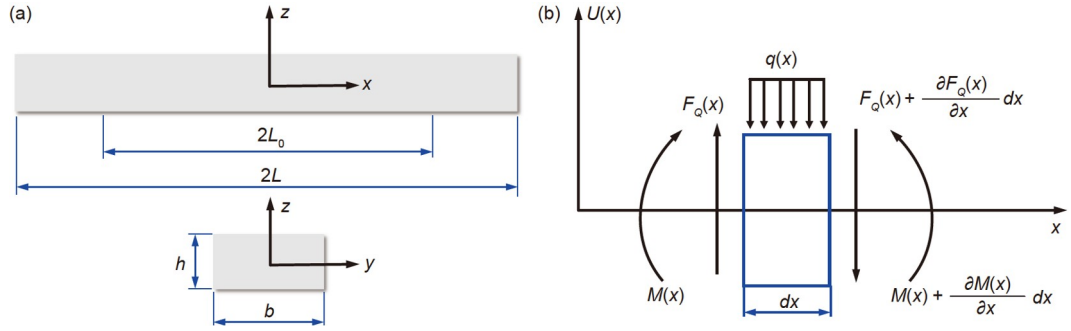

Figure 10 (Color online) (a) Shape of the three-point bending ultrasonic specimen; (b) the micro-section at position x was selected for force analysis in the case of transverse forced vibration.

As shown in Figure 10(b), the force balance equation and moment balance equation of the selected micro-section are

$$q(x)-\frac{\partial F_q}{\partial x}\mathrm{d}x+\rho A\mathrm{d}x\frac{\partial^2 U(x,t)}{\partial t^2}=0, \tag{8}$$

$$\frac{\partial M}{\partial x}\mathrm{d}x+F_q\mathrm{d}x=0. \tag{9}$$

The equation of the deflection curve of the slender beam is

$$EI\frac{\partial^2 U(x,t)}{\partial t^2}=-M(x), \tag{10}$$

where $q(x)$ is the uniform load applied to the micro-section and ρ is the density of the specimen material. E is Young's modulus, F_q is the shear force, and $M(x)$ is the bending moment. $U(x,t)$ is the excitation displacement and I is the area moment of inertia. Combining eqs. (8), (9), and (10), the transverse free vibration equation for a homogeneous equal-section beam is [21]

$$EI\frac{\partial^4 U(x,t)}{\partial t^4}+\rho hb\frac{\partial^2 U(x,t)}{\partial t^2}=0. \tag{11}$$

Separating variables for $U(x,t)$, $U(x,t)=U(x)\sin(2\pi ft)$, and f is the excitation frequency (20 kHz in this case). Thus, after some manipulations, eq. (11) can be written as

$$\frac{\partial^4 U(x)}{\partial t^4}-k^4U(x)=0. \tag{12}$$

The general solution of eq. (12) is

$$U(x)=C_1\sin(kx)+C_2\cos(kx)+C_3\sinh(kx)+C_4\cosh(kx). \tag{13}$$

Based on the boundary conditions and the resonance

requirements of the specimen, it is obtained that

$$\begin{cases} U(x) = U(-x), \\ U''(x)\big|_{x=\pm L} = 0, \\ U'''(x)\big|_{x=\pm L} = 0, \\ U(0) = A_0, \\ U(L_0) = 0. \end{cases} \tag{14}$$

Based on this, the transverse vibration displacement amplitude of the three-point bending UF specimen is

$$U(x) = U_0\left(\frac{\cosh kL}{\cos kL + \cosh kL}\right) \cdot\left(\cos kx + \frac{\cos kL}{\cosh kL}\cos kx\right). \tag{15}$$

The resonant lengths L and L_0, respectively, are

$$L = 0.506925\left(\frac{Eh^2}{\rho f^2}\right)^{1/4}, \tag{16}$$

$$L_0 = 0.27966\left(\frac{Eh^2}{\rho f^2}\right)^{1/4}. \tag{17}$$

The maximum stress $\sigma_{\max}$ in the specimen is

$$\sigma_{\max} = \frac{EhU_0k^2}{2}\left(\frac{chkL - \cos kL}{chkL + \cos kL}\right). \tag{18}$$

3.2.2 *Three-point bending UFT instrument*

The first three-point bending UF machine was developed in Bathias' laboratory [21,25], which was initially developed for testing certain aluminum alloy-based metal-matrix composites, ceramics, titanium-aluminum alloys, and other brittle materials used in the automotive industry. As shown in Figure 11, the three-point bending UF machine adds the tip and three-point bending support to the conventional ultrasonic components. A small size, low-density tip is mounted as an additional mass at the end of the horn which is used to excite specially designed rectangular specimens to produce transverse bending vibrations. The above components are mounted on the INSTRON 1122 to enable static bending loading. The machine is capable of loading up to 10^5–10^{10} cycles at 20 kHz with a stress ratio of 0.1 to 0.5.

In 2012, Backe et al. [91–94] developed a machine suitable for three-point bending UFT of composite CFRP. In general, the machine is almost the same as the one developed in Bathias' laboratory. However, due to the differences between CFRP and conventional materials, some specific technical details need to be noted. (1) Since CFRE exhibits orthogonal anisotropy, Young's modulus, shear modulus, and Poisson's ratio of the material in different directions need to be determined by axial tension and three-point bending tests. When these parameters are determined, the dimensions of the specimens can be derived by the FEA method. (2) Since polymers show higher viscoelastic damping than metal materials, a combination of the pulse-pause technique and compressed air cooling had to be used to avoid damage at high temperature. Moreover, real-time monitoring of the overall temperature of the specimen during the test was necessary, thus requiring the addition of a thermal infrared camera. (3) The integrated 3D scanning vibrometer performs high-resolution strain measurements in three orthogonal directions during UFT. From the measured shear and tensile strains, the corresponding stresses can be derived according to Hooke's law for orthotropic anisotropic materials. Laser Doppler vibrometry (LDV) is also an effective alternative in such tests [95]. In a subsequent study, Balle and Backe [96] added an *in situ* CT device to the above configuration, which allowed the observation of progressive fatigue damage on the polished edges of CFRP specimens.

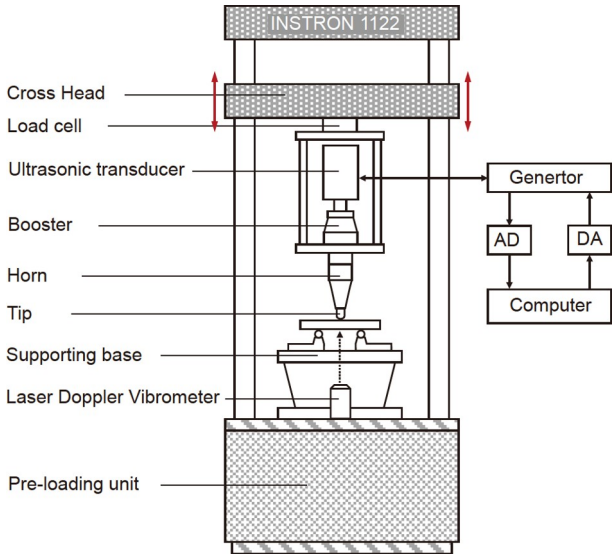

Figure 11 Schematic diagram of the three-point bending UFT machine.

Although this loading technique has proven to be effective in three-point bending VHCF performance testing of metal materials and some composite materials. However, some drawbacks need to be noted. First, since the specimen is not a fixed part of the ultrasonic resonance system, static prebending is applied to the specimen to ensure permanent contact between the loading device and the specimen during the whole test. Therefore, three-point bending UFT machines make it difficult to achieve full reverse bending. Moreover, the permanent contact generates considerable heat at the bending spans, especially in composite materials. In addition, this machine is not suitable for low-strength and low-stiffness materials. For materials with poor fretting fatigue properties, failure may occur at bending spans [28].

3.3 Cantilever bending fatigue

Cantilever bending UF is a novel UFT technique that

developed in recent years to obtain a large amount of vibration bending VHCF data of materials at $R=-1$ in an acceptable time. This type of fatigue is divided into two categories according to the difference in vibration modes of the specimens: (1) Fatigue based on first-order bending vibration and (2) fatigue based on second-order bending vibration.

3.3.1 *Specimen design theory*

In a previous study, Wan et al. [97] proposed a method for vibration analysis of variable-section Timoshenko beams considering internal damping, which is a semi-analytical method to directly reveal the relationship between external excitation and response. This method proved to be effective in the design of cantilever bending fatigue specimens. When conducting the cantilever bending UF test, consider a variable-section beam as shown in Figure 12.

For a base-excited Timoshenko beam considering internal damping as shown in Figure 12, the dynamics model can be expressed as [97]

$$\widehat{U}\left[\frac{\partial^2}{\partial t^2}\mathbf{u}(x,t)\right]+\widehat{C}\left[\frac{\partial}{\partial t}\mathbf{u}(x,t)\right]+\widehat{K}[\mathbf{u}(x,t)]=\mathbf{F}(x,t), \tag{19}$$

where $\boldsymbol{u}(x,t)$ is the state vector, $\boldsymbol{u}(x,t)=[y(x,t)\ \theta(x,t)]^{\mathrm{T}}$. $\mathbf{F}(x,t)$ is the load excited by base motion, $\mathbf{F}(x,t)=[\rho S(x)H_0\Omega^2 e^{j\Omega t}\ 0]^{\mathrm{T}}$. $\widehat{U}[\cdot]$, $\widehat{C}[\cdot]$, and $\widehat{K}[\cdot]$ are linear homogeneous differential operators for which the expressions are [98,99]

$$\widehat{U}[\cdot]=\begin{bmatrix}\rho S(x) & 0\\ 0 & \rho I(x)\end{bmatrix}, \tag{20}$$

$$\widehat{C}[\cdot]=\beta_s\begin{bmatrix}-\frac{\partial}{\partial x}\left[\mu S(x)G\frac{\partial}{\partial x}(\cdot)\right] & \frac{\partial}{\partial x}[\mu S(x)G(\cdot)]\\ -\mu S(x)G\frac{\partial}{\partial x}(\cdot) & -\frac{\beta_{\mathrm{b}}}{\beta_s}\frac{\partial}{\partial x}\left[EI(x)\frac{\partial}{\partial x}(\cdot)\right]+\mu S(x)G(\cdot)\end{bmatrix}, \tag{21}$$

$$\widehat{K}[\cdot]=\begin{bmatrix}-\frac{\partial}{\partial x}\left[\mu S(x)G\frac{\partial}{\partial x}(\cdot)\right] & \frac{\partial}{\partial x}[\mu S(x)G(\cdot)]\\ -\mu S(x)G\frac{\partial}{\partial x}(\cdot) & -\frac{\partial}{\partial x}\left[EI(x)\frac{\partial}{\partial x}(\cdot)\right]+\mu S(x)G(\cdot)\end{bmatrix}, \tag{22}$$

where E and G are Young's modulus and shear modulus of the beam material, respectively, and ρ is the density of the beam, β_{s} and β_{b} are the shear viscosity coefficient and bending viscosity coefficient of the internal damping beam, respectively. $I(x)$ is the area moment of inertia at x, $I(x)=w(x)h^3(x)/12$. $S(x)$ is the cross-sectional area of the beam at x, $S(x)=h(x)w(x)$. $w(x)$ and $h(x)$ are the width and height of the beam at x, respectively. μ is the Timoshenko shear coefficient of the beam, $\mu=10(1+\nu)/(12+11\nu)$, ν is the Poisson's ratio. For the beam in Figure 12, the natural frequencies and their mode shape function are obtained under free vibration (i.e., $\mathbf{F}(x,t)=\mathbf{0}$). In this case, the transfer matrix method (TMM) is introduced for solving eq. (19). The integrated transfer matrix $\mathbf{G}$ of the above beam can be expressed as

$$\begin{aligned}\mathbf{G}&=\mathbf{G}_N(\Delta L)\left[\prod_{r=1}^{N-1}\mathbf{G}_{r+1}^{-1}(0)\mathbf{G}_{\mathrm{r}}(\Delta L)\right]\mathbf{G}_1^{-1}(0)\\&=\begin{bmatrix}g_{11} & g_{12} & g_{13} & g_{14}\\ g_{21} & g_{22} & g_{23} & g_{24}\\ g_{31} & g_{32} & g_{33} & g_{34}\\ g_{41} & g_{42} & g_{43} & g_{44}\end{bmatrix},\end{aligned} \tag{23}$$

where

$$\mathbf{G}_i(x_i)=\begin{bmatrix}e^{-\frac{\delta_i}{2}x_i}\mathbf{V}_i(x_i)\\ e^{-\frac{\delta_i}{2}x_i}\mathbf{V}_i(x_i)\mathbf{J}_i^{-1}\mathbf{N}_i\\ EI_i e^{\frac{\delta_i}{2}x_i}\mathbf{V}_i(x_i)\mathbf{H}_{i,1}\mathbf{J}_i^{-1}\mathbf{N}_i\\ \mu GS_i e^{\frac{\delta_i}{2}x_i}\mathbf{V}_i(x_i)\left(\mathbf{H}_{i,1}-\mathbf{J}_i^{-1}\mathbf{N}_i\right)\end{bmatrix}, \tag{24}$$

in which

$$\mathbf{V}_i(x_i)=\begin{bmatrix}\sin(k_i x_i) & \cos(k_i x_i) & \sinh(p_i x_i) & \cosh(p_i x_i)\end{bmatrix}, \tag{25}$$

$$\mathbf{J}_i^{-1}=\begin{bmatrix}\delta_i/2 & -k_i & 0 & 0\\ k_i & \delta_i/2 & 0 & 0\\ 0 & 0 & \delta_i/2 & p_i\\ 0 & 0 & p_i & \delta_i/2\end{bmatrix}^{-1}, \tag{26}$$

$$\mathbf{H}_{i,1}=\begin{bmatrix}-\delta_i/2 & -k_i & 0 & 0\\ k_i & -\delta_i/2 & 0 & 0\\ 0 & 0 & -\delta_i/2 & p_i\\ 0 & 0 & p_i & -\delta_i/2\end{bmatrix}, \tag{27}$$

$$\mathbf{N}_i=\begin{bmatrix}-\frac{\delta_i^2}{4}-k_i^2+\frac{\rho\omega^2}{\mu G} & 0 & 0 & 0\\ 0 & -\frac{\delta_i^2}{4}-k_i^2+\frac{\rho\omega^2}{\mu G} & 0 & 0\\ 0 & 0 & -\frac{\delta_i^2}{4}+p_i^2+\frac{\rho\omega^2}{\mu G} & 0\\ 0 & 0 & 0 & -\frac{\delta_i^2}{4}+p_i^2+\frac{\rho\omega^2}{\mu G}\end{bmatrix}. \tag{28}$$

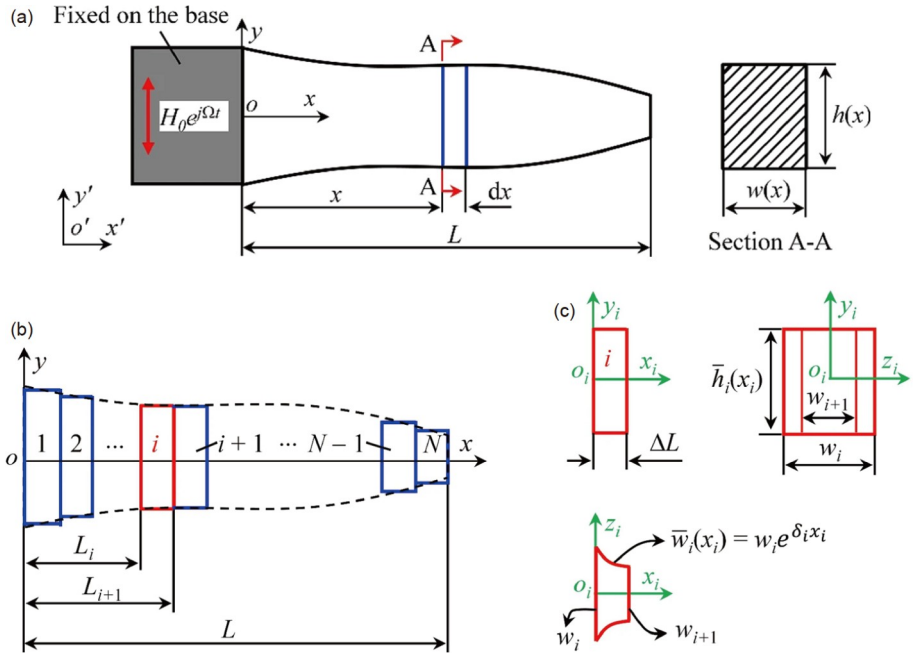

Figure 12 (Color online) (a) Shows a schematic diagram of a variable-section cantilever beam under base excitation [97]; (b) replacing the variable section beam into N elements with constant height and variable width [97]; (c) shows the *i*th element [97]. Copyright©2022, Springer.

For a cantilever beam undergoing UFT testing, the frequency equation can be written as

$$g_{33}g_{44} - g_{34}g_{43} = 0. \tag{29}$$

Based on eq. (29), the natural frequency of each order of the cantilever beam can be obtained. By introducing the modal superposition method, the displacement amplitude $Y_a(x, \Omega)$ of the beam in the absolute coordinate system can be obtained as

$$Y_a(x,\Omega) = \left| \sum_{n=1}^{N_n} \frac{\eta_n \Omega^2 Y_n(x)}{\omega_n^2 - \Omega^2 + 2\xi_n \Omega \omega_n j} + 1 \right| H_0. \tag{30}$$

The corresponding normal strain amplitude $\varepsilon_a(x, \Omega)$ is

$$\varepsilon_a(x,\Omega) = \left| \sum_{n=1}^{N_m} \frac{\eta_n \Omega^2}{\omega_n^2 - \Omega^2 + 2\xi_n \Omega \omega_n j} \frac{d\Theta_n}{dx} \right| h_a(x) H_0. \tag{31}$$

The UFT is conducted in the elastic phase, ignoring the possible plasticity. For linearly elastic materials, the normal stress amplitude $\sigma_a(x, \Omega)$ of the beam based on Hooke's law is derived as follows

$$\sigma_a(x,\Omega) = \left| \sum_{n=1}^{N_m} \frac{\eta_n \Omega^2}{\omega_n^2 - \Omega^2 + 2\xi_n \Omega \omega_n j} \frac{d\Theta_n}{dx} \right| h_a(x) E H_0. \tag{32}$$

3.3.2 *Based on first-order bending vibration*

To simulate the vibration-bending stresses of blade materials more accurately, Cheng et al. [22] developed a vibration-bending UFT machine. As shown in Figure 13(a), the machine has no difference from the conventional axial tension UFT machine. The only difference is that a specimen as shown in Figure 13(b) is used. The thick end of the specimen is fixed to the lower end of the horn by screws, which is similar to a cantilever beam. This fixed mode allows the longitudinal vibration provided by the ultrasonic component to be transformed into the transverse bending vibration of the specimen. The first-order vibration mode of the cantilever beam was utilized, and the maximum stress occurred at the arc near the fixed end, as shown in Figure 13(c). Song et al. [100] developed a double cantilever beam specimen, but with the same principle as the single cantilever beam specimen described above, as shown in Figure 13(d) and (e). According to the author's experience, the locking torque of the screw should be carefully adjusted to minimize the contact damping between the specimen clamping surface vs. the horn and the bolt end face when conducting this type of test. Otherwise, there will be a very significant temperature rise here. Cheng et al. [22] and Jiao et al. [101] used cold nitrogen and compressed cold air to suppress the specimen temperature rise, respectively. Jiao et al. [101] investigated the vibration bending VHCF performance of the compressor rotor blade material TC17 Titanium alloy based on this machine with loading cycles up to 10^9. They found that the S-N curve of TC17 Titanium alloy showed a continuous decreasing trend and there was no conventional fatigue limit. Moreover, no "fish-eye" feature was observed even in the VHCF regime, and the crack initiation location appeared on the surface of the specimen.

3.3.3 *Based on second-order bending vibration*

The stress distribution in the gauge section of the specimen

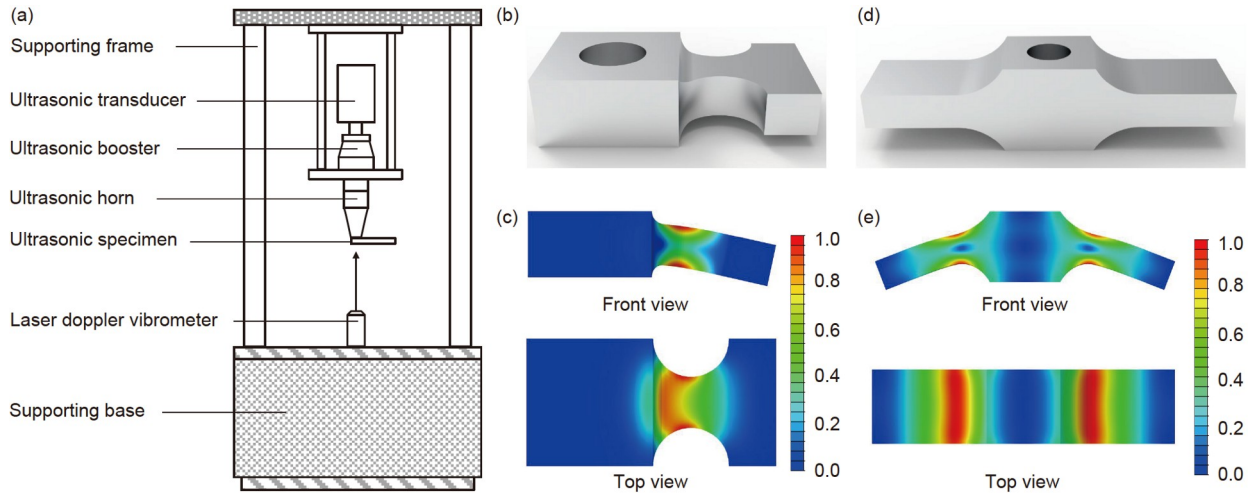

Figure 13 (Color online) (a) Schematic diagram of the UFT machine based on first-order bending vibration; (b) the shape of a single cantilever UF specimen based on the first-order bending vibration and (c) the stress distribution cloud in the specimen; (d) the shape of the double-cantilever UF specimen based on the first-order bending vibration and (e) the stress distribution cloud in the specimen.

based on the first-order bending vibration is very heterogeneous. Due to the presence of stress concentration, the maximum stress appears at the end of the specimen. To solve this problem and obtain a more uniform stress field, Ghadimi et al. [102] and Yang et al. [23] proposed UF specimens based on second-order bending vibration. Ghadimi et al. [102] developed a small thin plate bending UF specimen. The specimen was fixed between the horn and the full wavelength rod. A spacer is placed on the top of the specimen to maintain a distance between the upper surface of the specimen and the lower surface of the horn end. Different from the UF specimens based on the first-order bending vibration, the maximum stresses in the second-order bending vibration UF specimens appear in the parallel section away from the end. Tests on Inconel 718 alloy verified the feasibility of the method, with fracture locations occurring in the theoretical maximum stress region. The UF specimen designed by Yang et al. [23] is fixed at the horn end by two screws to form a cantilever beam structure, which also utilizes the second-order bending vibration mode of the beam. The free end of the specimen is set up as an hourglass type to ensure that the maximum stress occurs in the middle parallel section. In addition to more uniform stress distribution in the gauge section, the UF specimen based on second-order bending vibration provides a rotation angle equal to zero at the clamping end, which prevents the fretting fatigue that may occur here. In addition, the heat generated in the connection area due to friction is significantly reduced [23]. The maximum temperature in the specimen is only 35.4°C, even without any cooling measures.

Recently, Wan et al. [49] proposed a novel specimen shape and the optimization method of its dimensions based on the above theory. As shown in Figure 14, the specimen is clamped as a cantilever beam, which also works based on the second-order bending vibration pattern. VHCF experiments conducted with TC4 alloy verified the superiority of this specimen. A very uniform stress distribution was observed in the gauge section of the specimens, and all specimens were fractured at the expected locations. In addition, the specimen showed a relatively weak temperature increase in the gauge section.

In summary, the first advantage of the cantilever bending UFT technique is that the maximum stress occurs at the surface of the specimen and the heat generated can be transferred to the air in time. The deflection vibration of the specimen is also a forced convection process. Therefore, the specimens in this type of experiment have a very low-temperature rise in the gauge section, providing the possibility for continuous loading. The second advantage is that this load type is closer to the real vibration-bending mode of the blade material. Failure under first-order and second-order bending vibration is considered the most typical failure mode of blades [103].

3.4 Torsion fatigue

3.4.1 Specimen design theory

The first torsion UFT machine was developed by Stanzl-Tschegg et al. [104] in 1993. Unlike the longitudinal wave transfer in axial tension UFT, the design principle of this type of machine is based on the propagation of shear waves along different polar momentum rods. Therefore, all theoretical calculations of the ultrasonic component are conducted based on the one-dimensional motion equation of the shear wave. The one-dimensional torsional dynamics differential equation is [24]

$$J_{\mathrm{p}}(x)\frac{\partial^2\theta(x,t)}{\partial t^2}=\frac{G}{\rho}\frac{\partial}{\partial x}\left[J_{\mathrm{p}}(x)\frac{\partial\theta(x,t)}{\partial x}\right], \tag{33}$$

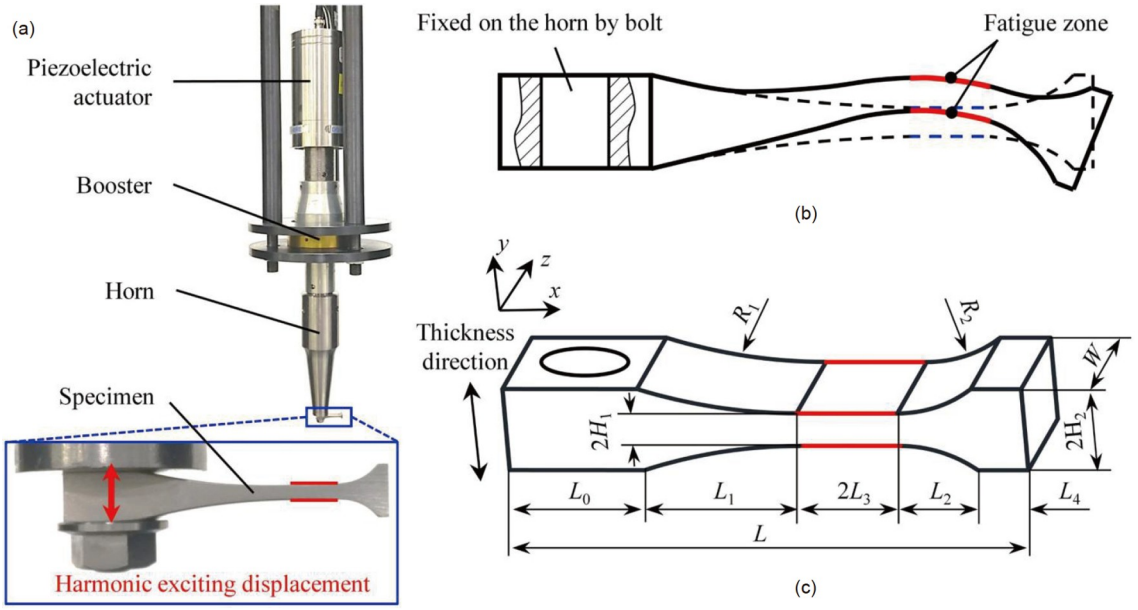

Figure 14 (Color online) The cantilevered ultrasonic specimens proposed by Wan et al. [49]. (a) Experimental configuration; (b) second-order bending vibration pattern of the specimen; (c) geometry of the specimen. Copyright©2023, Elsevier.

where ρ is the density of the specimen material and G is the shear modulus. $J_p(x)$ is the polar moment of inertia at position x, $J_p(x)=(\pi/2)R^4(x)$. $\theta(x,t)$ is the torsion angle that shows a sinusoidal variation with time, $\theta(x,t)=\theta(x)\sin(2\pi ft)$. Therefore, eq. (33) can be rewritten as

$$\frac{d^2\theta(x)}{dx^2}+4\frac{d(\ln R(x))}{dx}\frac{d\theta(x)}{dx}+k^2\theta(x)=0. \tag{34}$$

For the hourglass-type ultrasonic torsion specimen shown in Figure 15, when $L_2|x|\leqslant(L_1+L_2)$, the profile equation is $R(x)=R_2$. When $|x|\leqslant L_1$, the profile equation is $R(x)=R_1[\cosh(\alpha x)]$, where $\alpha=(1/L_2)\operatorname{arccosh}\left(R_2^2/R_1^2\right)$.

According to the boundary conditions and continuity conditions, eq. (30) is solved to derive the angular amplitude of specimen torsion $\theta(x)$

$$\begin{cases}\theta(x)=\theta_0\cos[k(L_1+L_2-x)],\\ L_1<|x|\leqslant(L_1+L_2),\\ \theta(x)=\theta_0\varphi(L_1,L_2)\dfrac{\sinh(\beta x)}{\cosh(\alpha x)},\\ |x|\leqslant L_1,\end{cases} \tag{35}$$

where $\beta=\sqrt{\alpha^2-k^2}$, $\varphi(L_1,L_2)=[\cos(kL_2)\cosh(\alpha L_1)]/\sinh(\beta L_1)$. The resonance length L_2 of the specimen is

$$L_2=\frac{1}{k}\arctan\left[\frac{1}{k}\left|\frac{\beta}{\tanh(\beta L_1)}-\alpha\tanh(\alpha L_1)\right|\right]. \tag{36}$$

The shear strain amplitude $\gamma(x)$ of the specimen is

$$\gamma(x)=\theta_0R_1\varphi(L_1,L_2)\frac{\sqrt{\cosh(\alpha x)}}{\cosh^2(\alpha x)}\cdot[\beta\cosh(\beta x)\cosh(\alpha x)-\alpha\sinh(\beta x)\sinh(\alpha x)]. \tag{37}$$

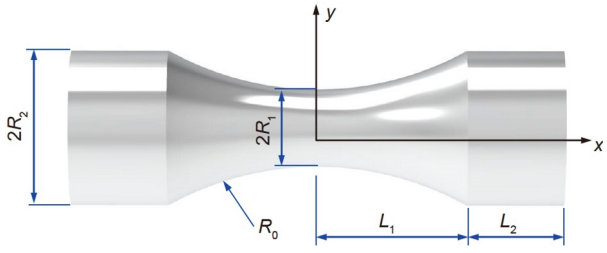

Figure 15 (Color online) Three-dimensional schematic diagram of a torsion ultrasonic fatigue specimen.

According to the generalized Hooke's law, the corresponding shear stress amplitude $\tau(x)=G\gamma(x)$. For torsion UF specimens, the maximum shear stress τ_{max} occurs at the surface of the specimen at the center gauge section.

$$\tau_{max}=G\theta_0R_1\varphi(L_1,L_2)\beta. \tag{38}$$

3.4.2 *Direct type*

The first torsion UFT machine was developed by Stanzl-Tschegg et al. [104] in 1993. Unlike the longitudinal wave transfer in axial tension UFT, the design principle of this type of machine is based on the propagation of shear waves along different polar momentum rods. Therefore, all theoretical calculations of the ultrasonic component are conducted based on the one-dimensional motion equation of the shear wave. Figure 16(a) and (b) show the torsion UFT machine developed by Mayer [24] in 2006. Due to the difference in the loading principle, all ultrasonic components needed to be redesigned while retaining only the electrical control system of the axial tension UFT machine. The redesigned transducer can convert the 21 kHz electrical signal from the ultrasonic

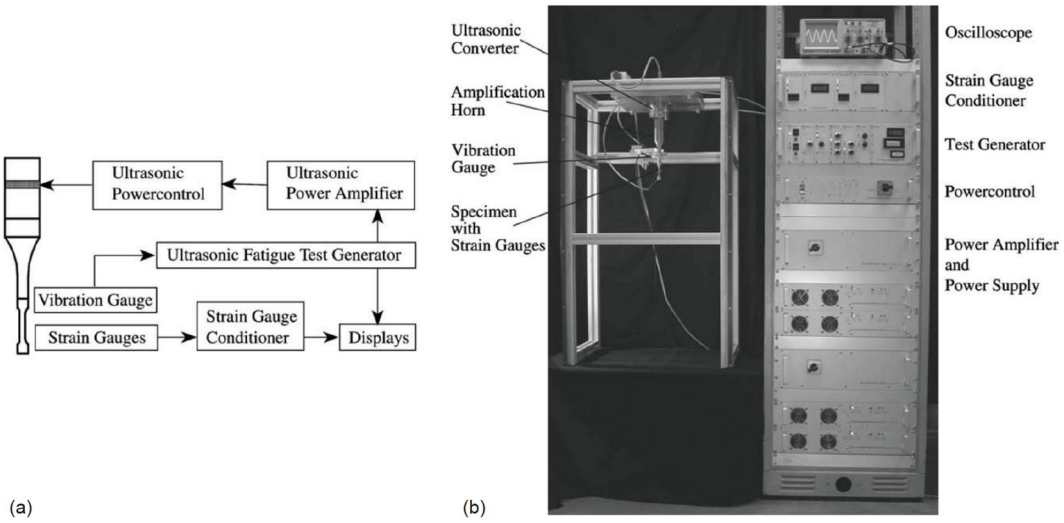

Figure 16 (a) Principle diagram and (b) physical image of the torsion UFT machine (R=–1) [24]. Copyright©2006, Elsevier.

generator into a shear vibration of the same frequency. The booster and horn were designed as a first-order torsional vibration variable-section cylindrical rod with 21 kHz to transmit torsional vibrations with amplification. Similar to the shape of the tensile UF specimen, the torsional UF specimen is generally a cylindrical rod with a reduced cross-section in the middle to achieve further amplification of the torsional amplitude. Interestingly, the lengths of all torsional ultrasonic components (including booster, horn, and specimen) are significantly smaller than those of axial tensile ultrasonic components, because shear waves are shorter and more sensitive to changes in cross-section than longitudinal waves [24]. Similar to the other types of UF tests mentioned above, the temperature rise of the specimen during the test is still a critical factor that cannot be ignored, and a pulsed pause or compressed cold air is used to maintain the temperature rise in an acceptable range.

In 2015, Mayer et al. [105] further developed a torsion UFT machine capable of superimposing static torsional loads to achieve torsion UF testing at positive stress ratios. The machine is based on a conventional torsion UFT machine modified with the addition of a horn and booster at the lower end of the specimen. A large diameter disc is installed at the booster displacement node and a static torsional load is superimposed on the specimen by a turntable-pulley mechanism. The change in stress ratio is achieved by varying the mass of the weight, resulting in a stress ratio range of –1 to 0.5. Tests on materials such as 2024-T351 aluminum alloy [24], VDSiCr spring steel [105,106], and SWOSC-V [107] verified the feasibility of the above machine for torsional VHCF tests up to 10^9. In 2021, Karr et al. [108] developed a torsion UFT machine that can be used in a vacuum environment and enabled monitoring of fatigue crack propagation processes in a vacuum environment with an integrated objective lens and CCD camera.

3.4.3 *Indirect type*

"A body vibrating on Y mode can be the source of power to get X mode on another body", Marinesgarcia et al. [109] developed a novel torsional UFT machine based on this idea. As shown in Figure 17, the actuator components of the machine contain the transducer, horn 1, and horn 2. Note that the dimensions of the transducer and horn1 are designed based on the wave equation for the longitudinal vibration of a variable-section rod to transmit and amplify the axial vibration. The dimension design of horn 2 is based on the one-dimensional motion equation of the shear wave to transmit and amplify the torsional vibration. Horn 1 and horn 2 are coupled at 90° by a connecting pin to realize the conversion of axial tension vibration to torsional vibration. Since the torsional wave is not directly generated by the transducer, it is referred to as an indirect torsion UFT machine. It is worth stating that there are two problems with the original machine. (1) The output shear stress is too small. (2) Significant stress concentrations at the pin and horn pinholes, resulting in premature pin failure. Considering the above problems, Petit et al. [110] optimized the original machine through FEA. The optimized basic parameters include the size of horn 2, pin diameter, chamfering of pinhole edges, and horn holes. The optimized machine can apply shear stress of 650 MPa to high-strength steel specimens and the machine does not fail after up to 10^9 cycles. A major advantage of the indirect machine is that, based on the existing axial tension UFT machine, only one mechanical part (horn 2) needs to be replaced to realize the torsional UFT purpose, which saves money for the new machine development. Secondly, indirect machines can generate higher shear stress levels in the specimen compared with direct machines because linear

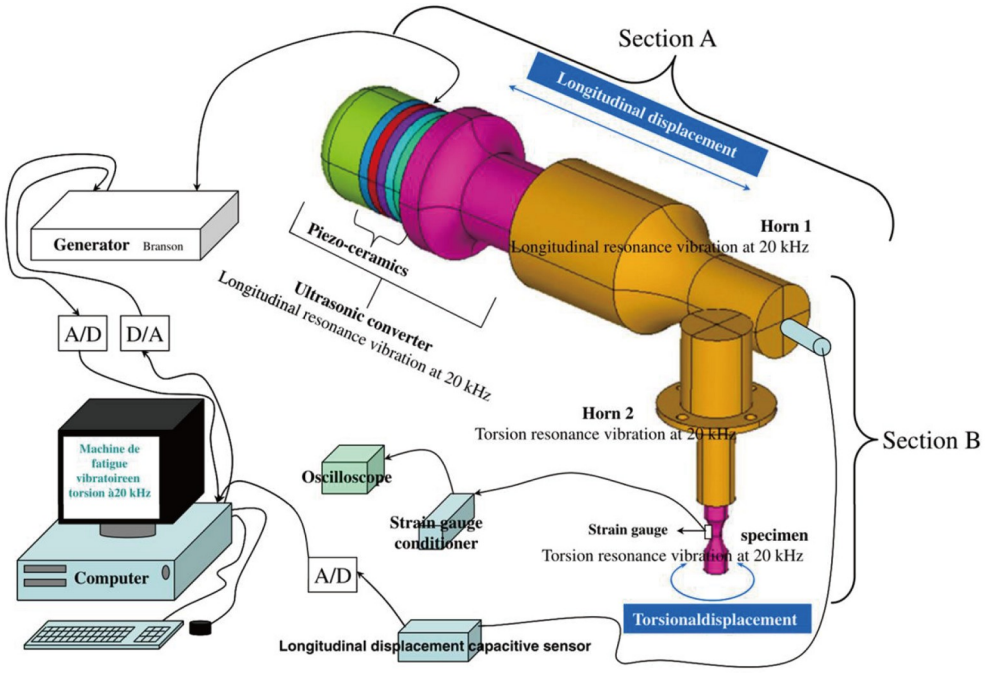

Figure 17 (Color online) Schematic diagram of the indirect type torsion UFT machine [109]. Copyright©2007, Elsevier.

transducers are more powerful than angular transducers [110].

3.5 Fretting fatigue

When mechanical vibrations occur between two clamped surfaces, fretting phenomena occur due to the stress concentration on the contact surfaces. This fretting phenomenon can lead to wear of the contact surfaces and trigger the initiation of small surface cracks under certain conditions [111]. Cracks caused by fretting effects have a more significant impact on the VHCF properties of the material than internal defects since most of the lifetime in the VHCF is devoted to crack initiation rather than crack propagation [112]. One of the most typical fretting fatigue areas in aviation gas turbine engines is the connection between the blade rabbet and the disc tongue-and-groove [113–115], which may experience fretting fatigue failure after up to 10^{10} cycles. Fretting fatigue in the HCF regime has been widely studied by many researchers and it has been confirmed that fretting wear significantly affects the HCF lifetime of the material [116,117]. However, the mechanism of material fretting fatigue within the VHCF regime has not been fully understood.

To study the fretting effect on the VHCF properties of the material, testing machines at ultrasonic frequencies were developed. In 1982, Mason [118] first used UFT machines for the study of fretting fatigue. In 2006, Bathias reported the first fretting UFT machine in a review [25]. As shown in Figure 18(a), this type of machine developed by Bathias et al. generally consists of the axial tension ultrasonic component and the normal contact force loading mechanism. Figure 18 (b) shows the stress of the specimen in fretting UFT. Fretting fatigue is the superposition of fatigue and fretting processes. The specimen attached to the horn end is excited to longitudinal vibration, which provides the required stress amplitude for fatigue while also providing a small relative motion. Under the action of the smaller relative motion and the appropriate normal force, the specimen surface undergoes a fretting fatigue process. Teng et al. [119], Huang et al. [120] and Filgueiras et al. [111] studied based on such machines and found that high-strength steels showed a significant decrease in VHCF life by a factor of 1 to 1.5 under the action of fretting.

In a subsequent study, Zhai et al. [121] made a series of improvements to the above machine to meet the high-temperature fretting UFT needs. The most important improvement includes the development of a temperature-building module. The specimen is heated by an induction heating furnace. The temperature is measured by an infrared thermometer and fed back to the power controller. The power controller achieves closed-loop control of the temperature by adjusting its output power. The furnace heats the specimen to a maximum temperature of 1000°C. Moreover, the temperature variation in the specimen during the stable loading stage can be controlled to ±5°C. A study by Zhai et al. [121] using this machine showed that the fretting VHCF strength of the nickel-based superalloy Nimonic 80A at 600°C is only

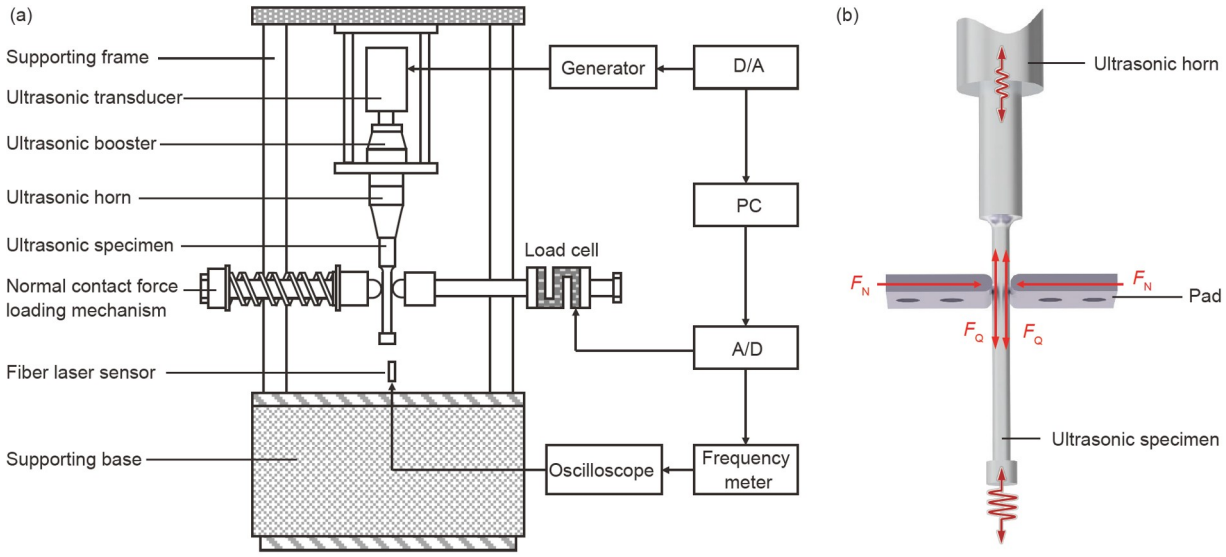

Figure 18 (Color online) (a) Schematic diagram of the fretting UFT machine; (b) the forces in the specimen during fretting fatigue F_N is the normal contact force and F_Q is the friction force.

about 300 MPa.

Considering that fretting fatigue in aircraft blades and impellers occurs during bending vibrations, the evaluation of the above components using only the axial tension fretting UF technique is not sufficient. To investigate the effect of fretting wear on the bending VHCF properties of the material, Song et al. [100,122] developed a specimen system. The specimen system consists of a plate specimen and two titanium clamps arranged symmetrically at the top and bottom of the specimen. The specimen system is screw mounted on the lower surface of the horn and is excited to bending vibration. During the test, small relative displacements between the specimen and the titanium clamps led to fretting wear. In this case, the specimen system had to be cooled using greenhouse water. A study by Song et al. [100] based on this system showed that fretting wear significantly weakened the bending VHCF performance of FV520B steel.

3.6 Multiaxial fatigue

Fatigue failure of blades is not the result of single stress but of multiaxial stresses, such as biaxial bending, combined tension-torsion, combined tension-bending, and combined bending-torsion [4,123,124], etc. Although good progress has been made in the development of electronic and electrohydraulic servo multiaxial fatigue machines, test time limitations prevent them from being applied to VHCF testing of blade materials. Achieving multiaxial fatigue at ultrasonic frequency is difficult, and existing ultrasonic fatigue testing techniques mainly focus on single loads such as tension-compression, cantilever bending, and three-point bending, which severely limit the accumulation of multiaxial VHCF fatigue performance data for blade materials. Therefore, the development of multiaxial UFT machines has attracted great interest in recent years.

3.6.1 Biaxial bending fatigue

Biaxial bending is one of the common multiaxial fatigue modes of the aviation gas turbine engine blade [17]. In recent years, Brugger et al. [26] have developed machines capable of conducting biaxial bending tests at ultrasonic frequencies. As shown in Figure 19, the machine is very similar to the three-point bending UFT machine. The only difference is that a disc specimen and ring span are used. The disc UF specimen is determined by only two parameters: the thickness and the diameter. Therefore, with the target of reaching a first-order natural frequency of 20 kHz for the biaxial bending mode, the dimension of the specimen can be easily derived by optimizing the thickness and diameter with the FEA method. It is worth noting that Nikitin et al. [125] have developed a theoretical method to determine the disc dimension and the stress components. The radius of the ring bending span is determined by the location of the specimen vibration node. Three centring pins were used to ensure that the specimen was centered and removed before conducting the ultrasonic test.

In this type of test, the specimen temperature rise is more significant than the three-point bend UFT due to the larger contact area between the specimen and the ring bending span. Brugger et al. [26] used compressed cold air for specimen cooling and an infrared camera for continuous monitoring of the specimen temperature. After 2.5×10^6 cycles, the temperature of the specimen increased by nearly 60°C. The drastic temperature rise is a drawback of this type of UF model.

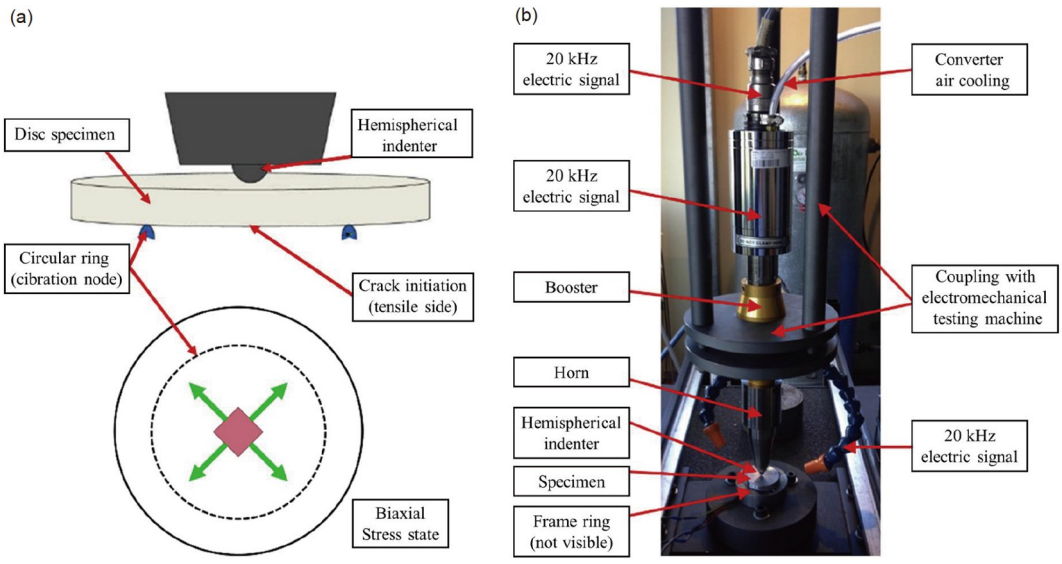

Figure 19 (Color online) (a) and (b) show the biaxial bending UFT machine, modified from [26]. Copyright©2017, Elsevier.

3.6.2 Combined tension-torsion fatigue

The action of centrifugal force and high-speed airflow blowing, coupled with the special twist shape of the blade, make the combination of tension stress and torsion stress in the blade. In 2016, Vieira et al. [27] developed a novel multiaxial UFT machine capable of conducting combined tension-torsion (CTT) tests at an ultrasonic frequency to the VHCF regime. The successful development of this machine involved two key issues. (1) The first one is the design of the horn. The dimensions of the horn are designed based on the wave equation for the longitudinal vibration of a variable-section rod to propagate the axial vibration. An iterative process was then performed on the horn with FEA methods to transform a portion of the longitudinal waves into torsional waves. The optimized horn has an overall tapered shape and is machined with two sets of oblique slits responsible for generating ultrasonic torsional waves. The degree of slanting of the oblique slits will significantly affect the ratio of axial to torsional vibrations in the final output. (2) The second is the specimen design. Different from the axial tension UF and torsion UF specimens, the CTT-UF specimens have a triple hourglass shape. The design idea of this specimen is to make the specimen generate mixed axial tensile and torsional vibration modes at 20 kHz by iterative design with the FEA software. da Costa et al. [126] showed that different tensile/shear stress ratios in the range of 0.35 to 0.8 can be achieved by optimizing the length of the end parallel section, the length of the middle parallel section, and the diameter of the second throat without changing the horn dimensions.

Figure 20 shows a schematic diagram of the CTT-UFT machine. As shown in Figure 20(b), the special horn is capable of providing both axial vibration U and torsional vibration θ. The CTT-UF specimen is excited by the horn to produce axial and torsional vibrations with the same frequency, and the two are superimposed together to form a biaxial stress state. As can be seen from the color bands in Figure 20(b), the maximum torsional angle and axial vibration amplitude occur at the upper and lower ends of the specimen, and the maximum axial and shear stresses occur at the main throat. As shown in Figure 20(c), two notches were machined on the lower end of the specimen and the rotational amplitude was measured by a two-channel POLYTEC vibrometer. The axial vibration amplitude at the end of the specimen is estimated by the vibrometer. As shown in Figure 20(d), strain gauge rosettes are glued to the main throat of the specimen to estimate the multiaxial strain state, and are converted to stresses by generalized Hooke's law. The relationship between the output power vs. the principal stress and shear stress needs to be calibrated before the test. In addition, the relationship between the output power and the tension-shear stress ratio also needs to be calibrated. Once these relationships are established, the test can be conducted.

3.6.3 Combined tension-bending fatigue

Combined tension-bending (CTB) is the most typical stress pattern for blade materials, which is attributed to the large centrifugal forces caused by the high rotational speeds (tens of thousands of rotations) and the bending forces caused by high-speed airflow excitation during the service of the blade. In the current stage, engineering designers generally use bending vibration tests to obtain the bending vibration fatigue strength of the blade at R=−1 and then apply Haigh diagram corrections to take into account the centrifugal force (tension force) effects [4,127]. From a mechanical point of view, this approach seems to be correct. This is because, for a

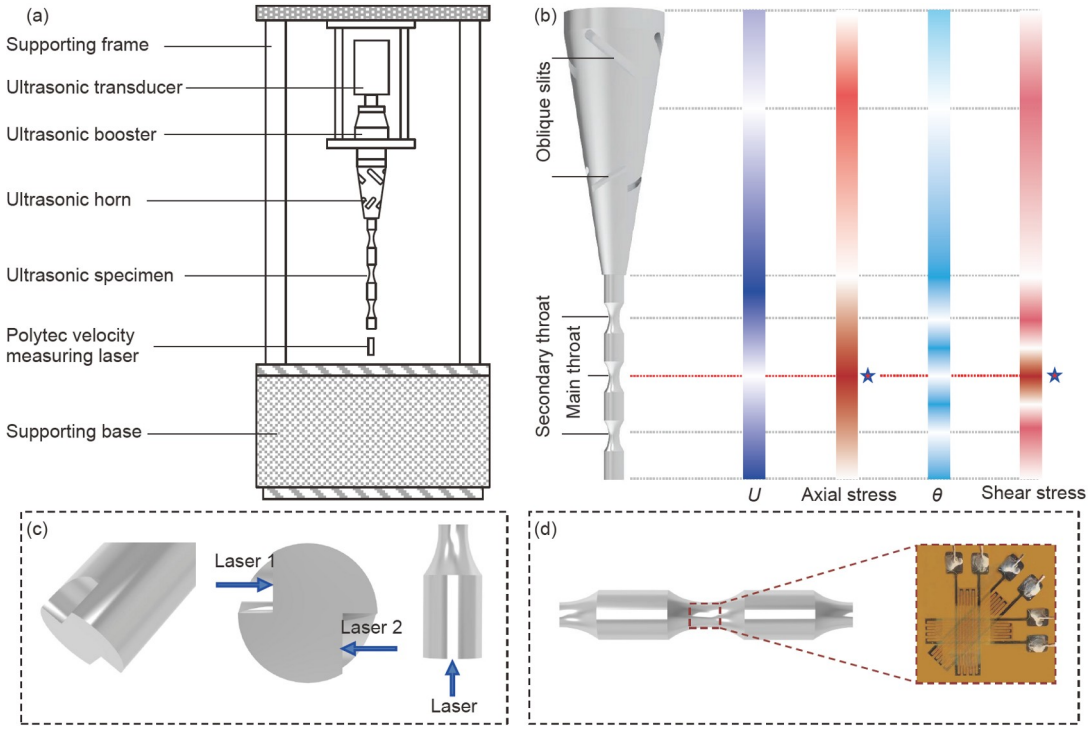

Figure 20 (Color online) (a) Schematic diagram of the CTT-UFT machine; (b) the distribution of axial displacement U, axial stress, torsion angle θ, and shear stress in the horn and specimen. The pentagrams mark the locations where the maximum axial and shear stresses occur; (c) shows the measurement of torsion angle θ and axial amplitude U; (d) the calibration of the multiaxial stress in the main throat is conducted with triaxial 45° strain gauge rosettes.

slender blade, both tensile and bending loads generate normal stresses. However, many studies have demonstrated that materials under CTB loads exhibit different deformation behavior [2,128], crack propagation processes [129,130], and failure modes [28,131] from those under single tension or bending. It is worth stating that some studies have shown that even specimens with the same material and dimensions exhibit different fatigue strengths in tension and bending [132]. In addition, gradient theory, volume theory, and weakest link theory (Weibull theory) also indicate that the effects of tension and bending on fatigue are not equivalent. These findings have raised concerns among blade designers. The necessity of developing a combined tension-bending fatigue (CTBF) machine was proposed by Nicholas [4] back in 2006.

The first reported combined tension-bending fatigue (CTBF) tests date back to 1962 [133,134]. However, machines capable of conducting CTBF tests at 20 kHz have not been reported until 2020 [28]. The CTB-UFT machine developed by Bao et al. [28] contains a universal testing machine, an ultrasonic component, and a tensile unit. The tensile unit is fixed to the universal testing machine base and the CTB-UF specimen is clamped at both ends. The axial tensile load is applied through the bolt on the right side to simulate the centrifugal load on the blade. The size of the CTB-UF specimen has been specially designed to ensure that it is excited to 20 kHz bending vibration when clamped at both ends. Detailed information about CTB-UF specimen design can be referred in ref. [135]. Figure 21(a) shows the CTB-UFT machine developed by Zhao et al. [29]. A servo-electric cylinder is used to provide the static bending load. The ultrasonic component fixed at the end of the servo-electric cylinder provides bending vibration at 20 kHz. A hydraulic cylinder assembly arranged symmetrically in the horizontal direction provides the tensile load. For a detailed description of the machine, please refer to [29]. The same specimen type as that of Bao is used. Since the CTB-UF specimen is fixed at both ends during the test, it does not produce a significant temperature rise as in the three-point bending mode. The specimen temperature rise can be easily controlled to below 20°C by compressing cold air or low temperature nitrogen. Considering the complexity of CTB-UFT, the author provides a detailed experimental procedure for the reader's reference (see Figure 21(b)). It is worth stating that good agreement has been obtained between the CTB-UFT test results of these two CTB-UFT machines for the Ti-6Al-4V alloy. The axial tensile load does not significantly affect the HCF and VHCF life of the material, but has a significant effect on the location of fatigue crack initiation. Compared with the three-point bending test, the application of axial tension load reduced the stress gradient in the specimen, resulting in a shift of the crack initiation point to the interior of the specimen in CTB-UFT.

It is worth stating that in addition to the three multiaxial

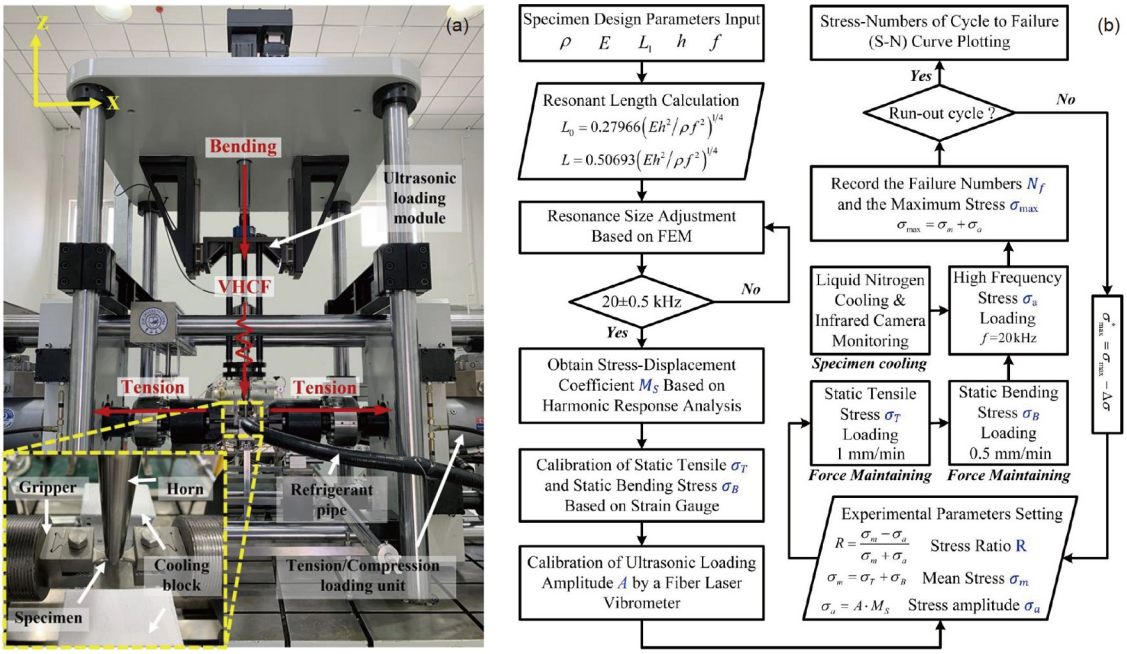

Figure 21 (Color online) (a) The CTB-UFT machine developed by the author [29]; (b) flow chart for conducting CTB-UFT [29]. Copyright©2021, IEEE.

UFT machines focused on in this review, several novel multiaxial UFT machines have been developed in recent years to achieve biaxial tension and combined tension-shear [136–139].

4 Variable amplitude and combined cycle fatigue

In addition to the different types of uniaxial/multiaxial fatigue described above, there are two typical fatigue modes in blades. Variable amplitude (VA) fatigue is one of them and almost all technical components operating in a vibrating environment experience VA fatigue rather than constant amplitude fatigue. The second type is combined cycle fatigue (CCF). The variation of blade centrifugal force during takeoff-landing of the aircraft leads to the axial LCF process, while the high-frequency low-amplitude bending vibration caused by the continuous airflow excitation leads to the HCF and VHCF processes in the bending direction of the blade. The superposition of the two triggers the CCF failure of the blade material. The above fatigue failure modes have contributed to the development of VA fatigue and CCF testing techniques.

4.1 Variable amplitude (VA) loading

In the 1930s, researchers realized that the ideal CA load could not fully replace the real service conditions of an engineered component. The earliest studies of VA load date back to 1938, when engineers working in aeronautics studied the VA characteristics of in-service stress cycles [140]. In 1939, Gassner [141] presented the first VA loading sequence for aerospace component testing. The earliest study of VA loading in the VHCF regime dates back to 1986 when Stanzl et al. [12] studied the VHCF performance of AISI C1020 steel under two Gaussian-distributed random loading sequences using ultrasonic equipment. The stress ratio R=−1 and the loading cycles range from 3×10^6 to 3×10^9 cycles. As in Figure 22(a), the conventional UFT performs a pulse-pause loading process where all the pulse-loading spectrum blocks have the same stress amplitude. As shown in Figure 22(b), when executing the VA procedure, the ultrasonic component varies the stress amplitude of the pulse-loading spectrum blocks according to the predetermined VA sequence. In 2014, Mayer et al. [30] developed a VA-VHCF test technique capable of superimposing static loads to perform VA tests at the ultrasonic frequency with R≠−1. As shown in Figure 22(d), the ultrasonic component is fixed to the frame of the MTS 810 servo-hydraulic system by a highly rigid assembly to realize the superposition of ultrasonic fatigue load and static load. Mayer et al. [30] also provided a test spectrum for VA-UFT performed at different stress ratios R with this machine, as shown in Figure 22(c). Both the stress ratio R and ultrasonic stress amplitude remain constant during a pulse time, but both change in the next pulse time according to the set program. VA-UFT is computer-controlled and the main processes are: (1) Pre-tension loading. Pre-tension values are determined by the computer based on the specimen gauge section size, the stress ratio R, and ultrasonic stress amplitude during the upcoming pulse time. Pre-tension is applied in a ramped manner for a set

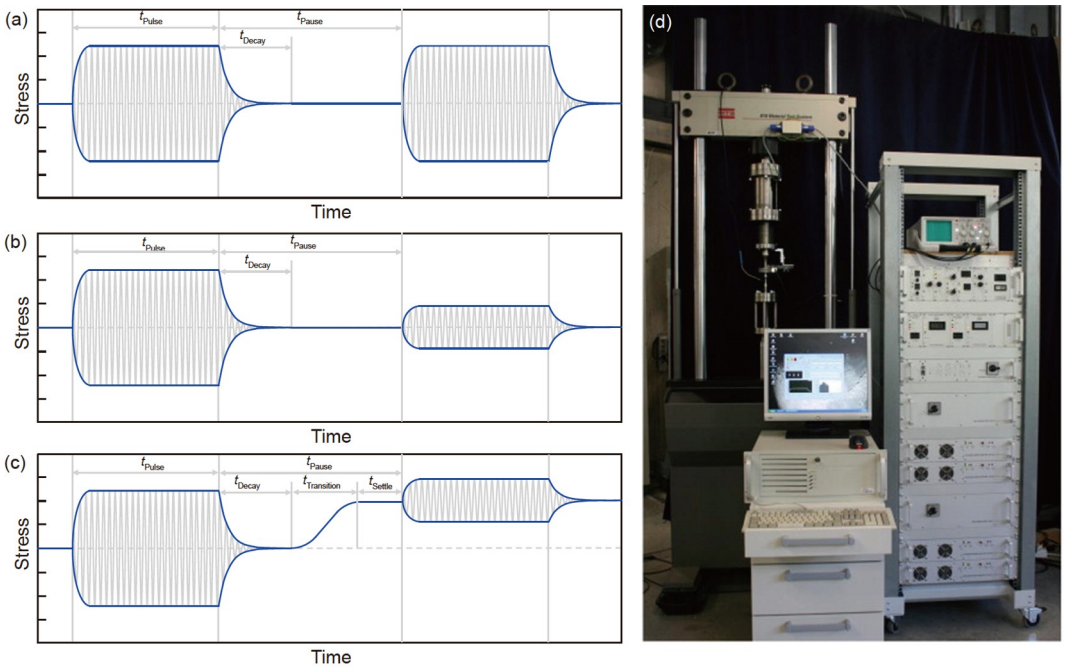

Figure 22 (Color online) (a) Ultrasonic pulse spectrum block for CA loading; (b) ultrasonic pulse spectrum block with VA loading at R=−1; (c) ultrasonic pulse spectrum block with VA loading at $R\neq-1$; (d) UFT machines performing variable stress ratio VA loading [30]. Copyright©2014, Elsevier.

transition time $t_{Transition}$. A settling time t_{Settle} is set to prevent overshoot of the load. The operating status of the static load system and whether the load reaches the correct value are checked by the computer during t_{Settle}. (2) Ultrasonic stress loading. After the pre-tension reaches the correct value, keep the pre-tension constant while starting the ultrasonic pulse at the set amplitude to excite the specimen to produce axial resonance. Monitoring and control of the vibration amplitude with the computer. (3) Measure all vibration amplitudes during the pulse time t_{Pulse} and decay time t_{Pause} time. (4) Finally, the acquired vibration amplitudes are classified into categories of 0.1% width and counted. Repeat (1) to (4) until all set loading procedures are completed. The results of VA-VHCF tests conducted by Mayer et al. [30] on aluminum alloy 2024-T351 at R=−1, 0.1, and 0.5 showed that using CA or VA data from HCF to predict VA lifetime in VHCF can be significantly biased. Although numerous studies have focused on the effect of VA on the HCF behavior of the material. However, the effect of a large number of low amplitude cycles in VA on the VHCF properties of the material has not been fully understood yet, and it is necessary to accumulate experimental data based on this type of machine.

4.2 Combined cycle fatigue

In general, fatigue caused by the superposition of low-frequency loads on high-frequency loads can be referred to as combined cyclic fatigue (CCF) [142,143]. It is worth stating that European aircraft engine manufacturers and some research institutes have launched the European PREMECCY (PREdictive MEthods for the Combined CYcle fatigue in gas turbines) program [65] in 2011 to enhance the CCF life prediction methods for aircraft blade materials. Existing studies have focused on CCF conducted using conventional servo-hydraulic machines with loading cycles generally less than 10^7 [144,145]. Studies on CCF based on electromagnetic resonance machines have been presented in Subsbusection 2.2.1 of this paper, but limited by the test frequency (generally close to 1000 Hz), the maximum loading cycles generally do not exceed 10^8 [57]. In 2001, Matikas [146] developed a novel machine to study the CCF of materials. Similar to the machine in Figure 22, an ultrasonic component is integrated into the frame of a commercial servo-hydraulic fatigue machine to achieve superposition of LCF fatigue with HCF and even VHCF with maximum loading cycles of up to 10^9–10^{12}. The CCF test spectrum specified in the European PREMCCY program [65] can be imposed by this machine. In 2014–2016, Arcari et al. [147] and Stanzl-Tschegg et al. [148,149] developed a CCF test technique capable of superimposing VA loads (VA-CCF test technique) based on the machine in Figure 22 at the University of Natural Resources and Life Sciences, Vienna, BOKU. They superimposed low-frequency loads of different waveforms (0.1–20 Hz) and CA/VA ultrasonic spectrum blocks that represent real load spectrums experienced during aircraft engine service due to gust, buffet, flutter, or other types of vibration processes. Figure 23 shows several typical VA-CCF test spectrums with ultrasonic spectrum blocks superimposed on low-frequency loads [148,149]. A series of experiments by Stanzl-Tschegg et al. [148,149] using the

above typical VA-CCF test spectrum on 7075-T651 alloy showed that the interaction between loads has a significant effect on the fatigue life and the presence of crack initiation-expansion processes, with VA-CCF fatigue life is significantly lower than that under CA. At present, experimental data under VA-CCF are very scarce and still in the data accumulation stage.

Although the interaction between LCF and VHCF can be well investigated in the VHCF regime using the above-mentioned machines. However, the CCF based on these machines generally focuses on axial tension compression, which is difficult to equate to the real service conditions of the blade materials. In 2021, the author developed a machine capable of conducting combined tension-bending CCF (CTB-CCF) at ultrasonic frequency [2,29]. This machine is capable of superimposing LCF in the tensile direction and HCF/VHCF loads in the bending direction, which is closer to the service conditions of the blade materials. Table 3 compares the CCF machine developed by the authors with other VA machines or CCF machines. As shown in Figure 24(a) and (b), two hydraulic cylinder assemblies are symmetrically installed in the horizontal direction of the machine, capable of providing low-frequency axial tension-compression loads in the frequency range of 0.1 to 50 Hz. A servo-electric cylinder assembly is mounted above the machine to provide static bending loads. The ultrasonic component is connected in series at the end of the servo-cylinder assembly to provide ultrasonic bending excitation force. Two modes of the CCF test spectrum were used, as shown in Figure 24(c). The specimen designed by Wang et al. [135] was used during the

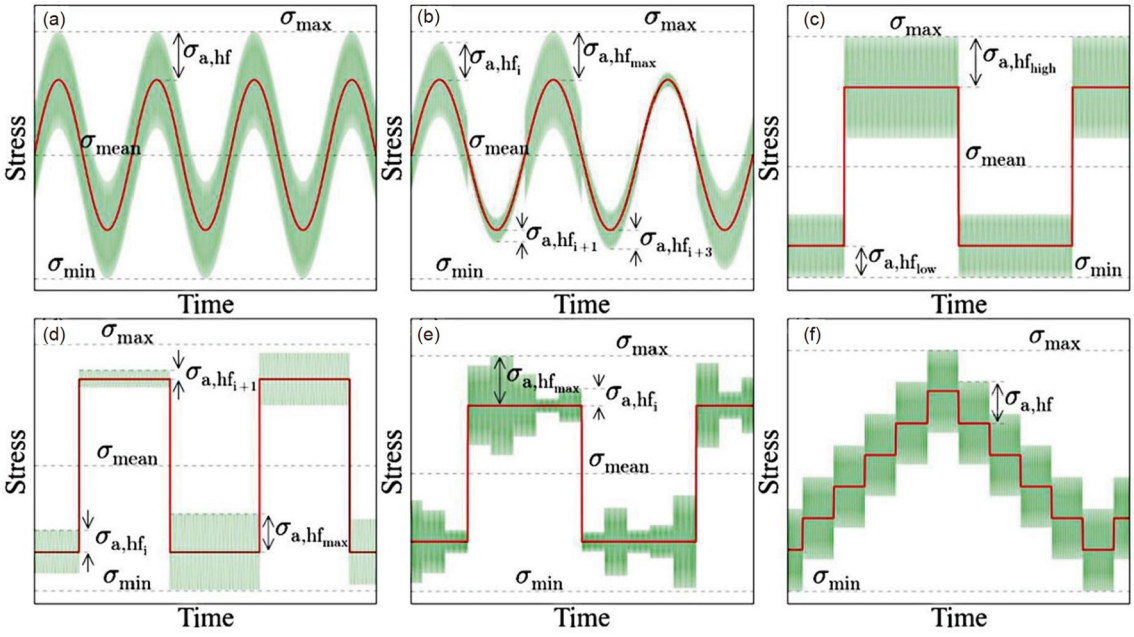

Figure 23 (Color online) (a)–(f) Typical VA-CCF test spectrums with ultrasonic spectrum blocks superimposed on the low-frequency curve [148,149]. Copyright©2015, Elsevier; Copyright©2016, Elsevier.

Table 3 Comparison of the CCF machine developed by the author with other VA machines or CCF machines[a)]

Test actuator	Reference	Test frequency (Hz)	Test method	Specimen type	CA or VA	CCF test
Electrohydraulic actuator + shaker	Li et al. [57] Hu et al. [55] Han et al. [58]	1000, 5000, 80	CTB	Materials specimen, blade-like specimen, full-size blade components	CA	Yes
Electrohydraulic actuator + ultrasonic	Matikas [146]	20 k	AT	Materials specimen	CA	Yes
Electrohydraulic actuator + ultrasonic	Mayer et al. [30]	20 k	AT	Materials specimen	VA	Yes
Ultrasonic + electrodynamic Actuator + manual	Bao et al. [28]	20 k	CTB	Materials specimen	CA	No
Electrohydraulic actuator + ultrasonic + electrodynamic actuator	Zhao et al. [29] (the author)	20 k	CTB	Materials specimen	CA (VA Under Development)	Yes

a) CTB indicates combined tension-bending, AT indicates axial tension, CA indicates constant amplitude, VA indicates variable amplitude, and CCF indicates combined cycle fatigue.

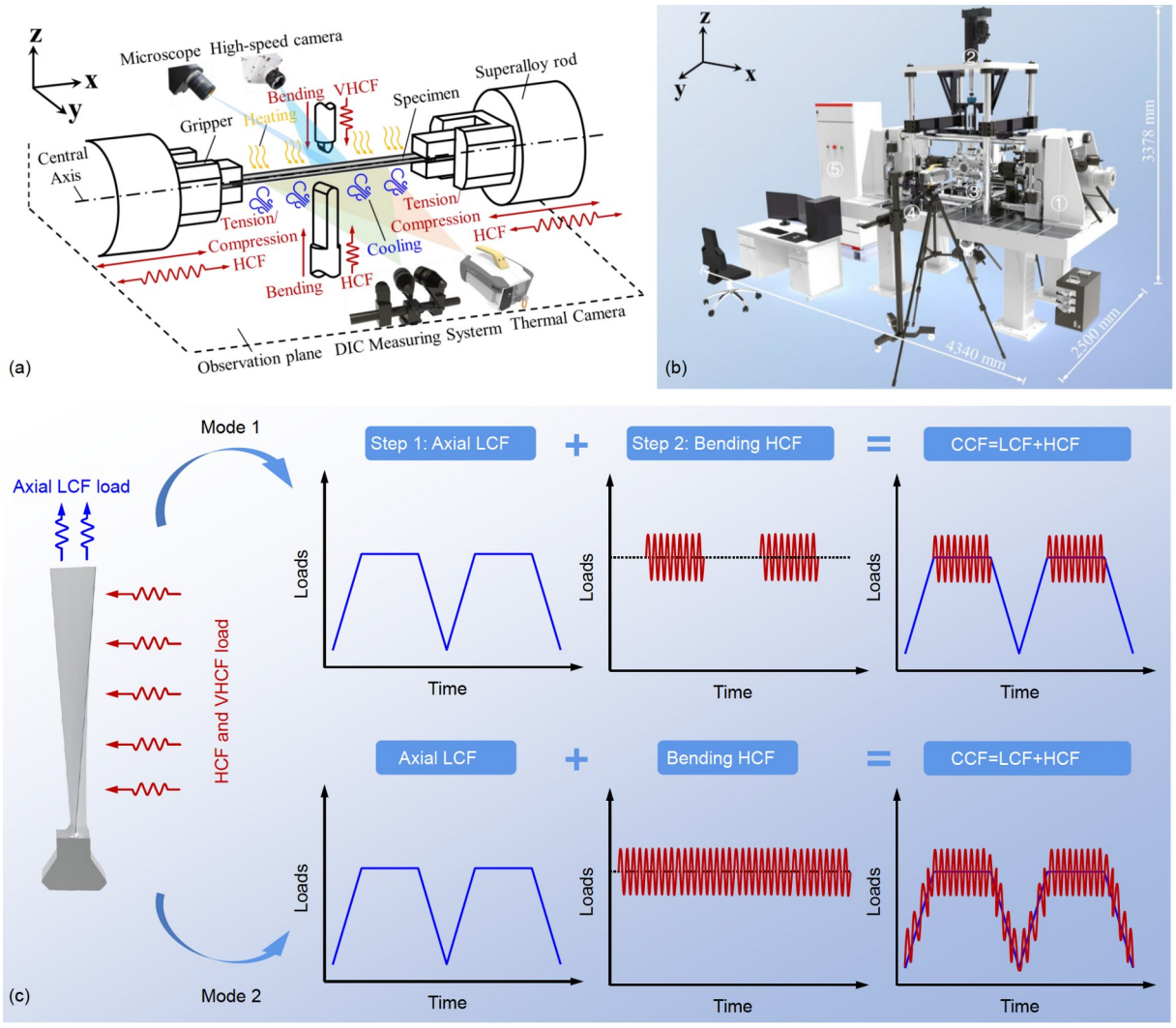

Figure 24 Shows (a) the test schematic of the machine and (b) the three-dimensional model of the machine [29]; (c) two modes of test spectrum used by the author to conduct the CTB-CCF test. Copyright©2021, IEEE.

test and was able to be excited to 20 kHz bending vibration in the case of clamping at both ends. When executing the CCF test spectrum for mode 1, the flow is: (1) The servo-cylinder assembly of the machine is activated to apply bending pre-contact to the specimen. Different from the three-point bending UFT, since the specimen is fixed at both ends, only a small pre-contact force (about a few N) needs to be applied to ensure continuous contact between the bending tip and the specimen surface during the test. (2) The servo-hydraulic assembly of the machine is activated and a low-frequency trapezoidal wave is applied in the axial direction of the specimen in a force control mode according to a pre-set program. The trapezoidal wave contains a rising phase, a load-holding phase, and a falling phase. (3) The output of the ultrasonic pulse spectrum block is triggered when the low-frequency load reaches the load-holding value. The amplitude of the ultrasonic pulse spectrum block is pre-set and remains constant during each pulse time. (4) Repeat steps (1)–(3) until the specimen breaks or reaches the run-out cycle. When performing the CCF test spectrum in mode 2, the flow is (1) Pre-contact, which is the same as mode 1. (2) Activation of the servo-hydraulic and ultrasonic assemblies to trigger the axial low-frequency trapezoidal wave and ultrasonic pulse spectrum blocks simultaneously until the specimen breaks or reaches the run-out cycle. Note that the possibility of superimposing axial low-frequency loads with ultrasonic loads in the bending direction was found to be based on an important prerequisite through experiments. First, axial low-frequency loading does not significantly change the resonant frequency of the specimen in the bending direction [135]. Second, because the amplitude of the ultrasonic pulse spectrum block is very small (about tens of μm), it does not interfere with axial low-frequency loads. In conclusion, no complex coupling effects occur between the different loading axes [2]. It is worth noting that, according to the author's experience, when developing an axial variable stress ratio VA-VHCF machine or CCF machine, a booster with a rigid connection method should be selected

(booster has three connection methods: rigid connection, elastic pin connection, and elastic washer). Furthermore, a highly rigid sleeve is used to connect the ultrasonic assembly to the hydraulic loading frame, thus increasing the axial stiffness of the axial load chain as much as possible.

5 Testing techniques in different environments

Blade materials are subjected to high-temperature and extreme atmospheric conditions (humidity and corrosive environments) during service, and their performance is significantly influenced by complex environmentally induced chemical processes. The final challenge in the laboratory simulation of blade material service conditions is the construction of complex environments, including high-temperature, humidity, and corrosive environments.

5.1 High-temperature

The earliest high-temperature UFT machine was developed by Yi et al. [31] in 2007. The induction heating device is integrated with the axial tension UF machine for high-temperature UFT purposes, as shown in Figure 25. In addition, to avoid the adverse effect of high-temperature conduction to the ultrasonic transducer, a full-wavelength rod is connected between the horn end and the specimen, and the rod is cooled by compressed cold air. For this type of machine, temperature control is a key point because the self-heating of the specimen is superimposed with induction heating. It is now common to use pulse-pause technology to avoid specimen self-heating, and to use an infrared thermometer for real-time monitoring and feedback of specimen temperature to achieve closed-loop control of temperature. A different approach is used by Cervellon et al. [150], who used a continuous loading method that allows the co-existence of self-heating and induction heating of the specimen. The temperature stability of the specimen is maintained by adjusting the PID closed-loop control parameters, which places higher demands on the temperature control system. But obviously, this approach has a higher loading efficiency. Specimen design is another key point. Due to the significant effect of high temperature on Young's modulus of the material, the presence of a large temperature gradient along the axial direction of the specimen makes it impossible to treat the specimen as a homogeneous material anymore. Thus the control equation for the specimen is rewritten as [31]

$$\frac{\partial^2 U(x,t)}{\partial x^2}+\frac{\mathrm{d}}{\mathrm{d}x}[\ln A(x)+\ln E(x)]\frac{\partial U(x,t)}{\partial x}+\left(\frac{2\pi}{\lambda}\right)^2 u=0, \tag{39}$$

where x is the position along the axial direction of the specimen, $U(x,t)$ is the displacement, ρ is the density of the material, and $A(x)$ is the cross-sectional area of the specimen. $E(x)$ is position-dependent due to the temperature-induced change in Young's modulus. There are two additional steps to be performed. The relationship between Young's modulus and the temperature of the specimen material is determined by axial tensile testing, and the empirical formula $E(T)$ is obtained by polynomial fitting. Then, the temperature distribution $T(x)$ in the axial direction of the specimen is measured using an infrared thermometer. The relationship $E(x)$ between the axial position of the specimen and Young's modulus is established by combining the empirical formula $E(T)$ with the temperature distribution curve $T(x)$. After this relationship is established, the dimensions of the specimen

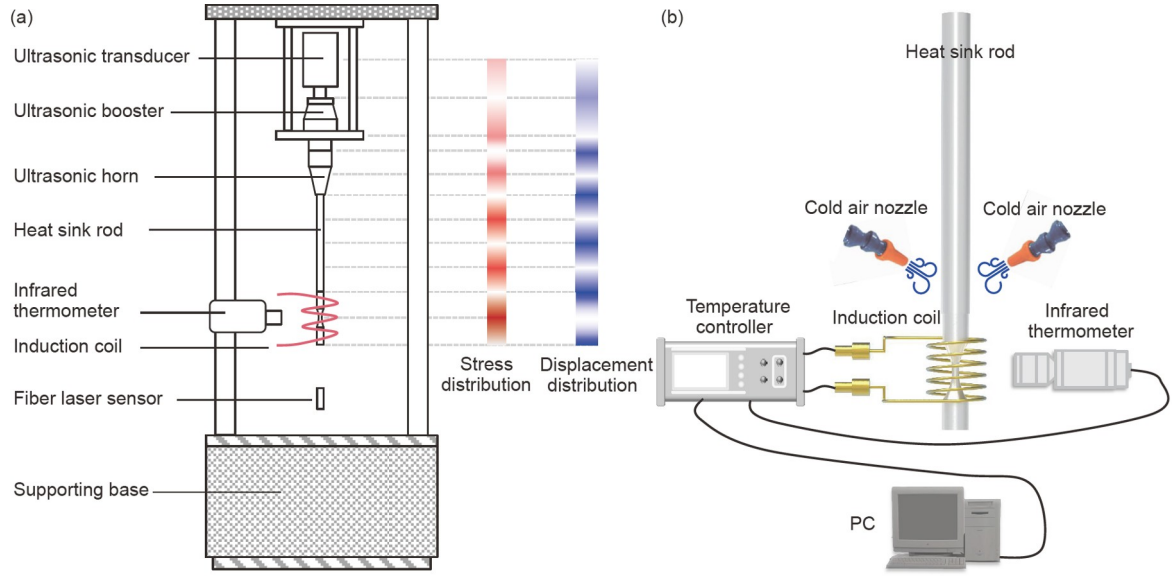

Figure 25 (Color online) (a) and (b) show the schematic of the high-temperature UFT instrument (Adopted high-frequency induction heating method).

can be obtained by eq. (39). Specimen dimensions can also be obtained by FEA methods. Zhang et al. [151] provided a simple method where specimens are designed based on parameters at room temperature and then a suitable frequency is achieved by reducing the end size.

However, the induction heating method has some problems that cannot be ignored. First, it leads to a large temperature gradient (~400°C@1000°C [31]). The large temperature gradient poses a challenge for specimen design. The gradient variation of Young's modulus of the specimen material makes it no longer considered homogeneous [31,152,153]. Furthermore, the coupling of temperature gradients and high-frequency vibrations makes it difficult to accurately evaluate the specimen stress. Second, the inherent limitations of induction heating make the temperature range of RT~300°C difficult to realize. However, the aircraft fan blades and the front two stages of low-pressure compressor blades are operating at this temperature. Third, this heating form has a great limitation, it is only applicable to conductive metals. Considering the above-mentioned problems, Schöne et al. [154] and Zhao et al. [29] developed the UFT technique in a high-temperature atmosphere. Figure 26 shows the high-temperature UFT machine developed by Schöne et al. [154]. The machine consists of a hot air furnace and an ultrasonic component. The airflow produced by the blower passes through the heating element to form hot air. The hot air flows over the specimen surface to realize the heating purpose. The hot air is recovered by a closed-loop system. The thermocouple arranged around the specimen measures and feeds back the specimen temperature, and the closed-loop control of the specimen temperature is realized by the PID controller. To avoid self-heating of the specimen, the pulse-pause technique is used. To avoid temperature conduction upwards along the ultrasonic component, the horn is cooled by compressed cold air above the hot air furnace. Compared with induction heating technology, this convection heating technology can heat specimens of any material.

Figure 27 shows the high-temperature UFT machine developed by Zhao et al. [29]. As shown in Figure 27(a), the machine consists of an ultrasonic module and a high-temperature module. Eight silicon molybdenum rods create a uniform high-temperature atmosphere (150°C–700°C) around the specimen using thermal radiation. The K-type thermocouple set close to the specimen measures and feedback the specimen temperature. The temperature controller enables closed-loop control of temperature by adjusting the voltage in the silicon molybdenum rod. The infrared thermal camera is used to monitor the temperature distribution on the specimen surface. The maximum temperature gradient in the full-length direction of the specimen does not exceed 20°C at 700°C. This is almost negligible compared with the huge temperature gradients caused by the induction heating method. Therefore, high-temperature specimens can be designed as homogenous materials. As shown in Figure 27(c), the external flange of the special horn is connected to the bellows flange of the high-temperature module with the end extending into the high-temperature module. As shown in Figure 27(d), the special horn is a full-wavelength cylindrical rod. The special horn is equipped with complex flow channels inside and cooling sleeves at the displacement nodes. During the test, the cooling sleeve is connected to the compressed cold air circulation system to enable effective cooling. To avoid self-heating of the specimen, the pulse-pause technique is used during the test. It is worth stating that this high-temperature module adopts the structural scheme of a vacuum cavity-wrapped heating furnace, which can realize high-temperature UFT under a vacuum environment or thin air.

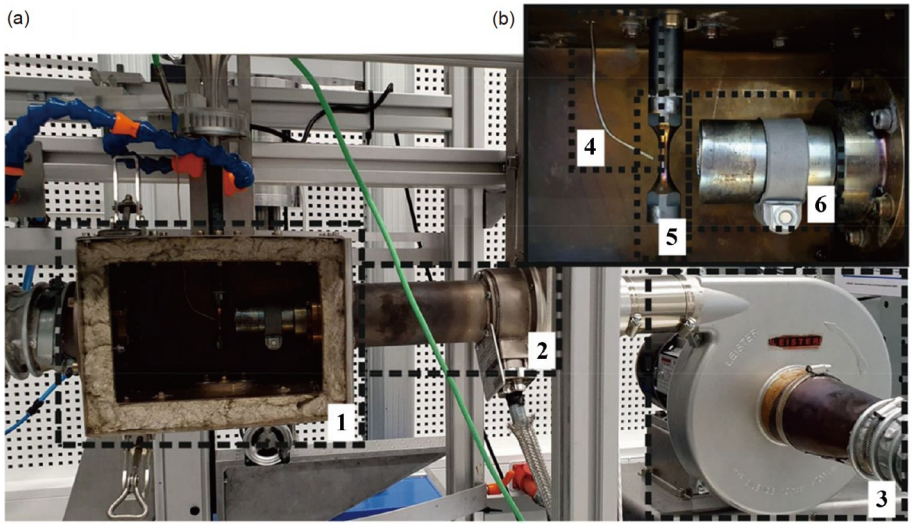

Figure 26 (Color online) (a) and (b) show a hot air furnace for high-temperature UFT [154]. (1) heating chamber, (2) heating element, (3) blower, (4) thermocouple, (5) ultrasonic specimen, and (6) hot air nozzle. Copyright©2022, MDPI.

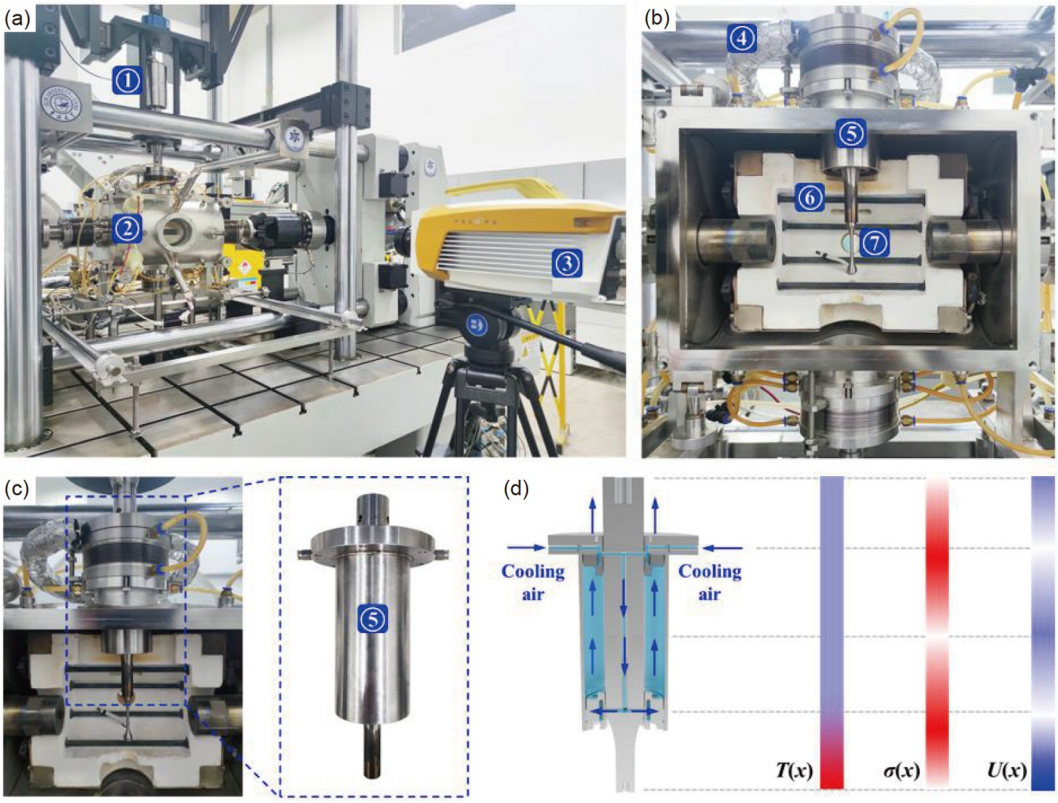

Figure 27 (a) High-temperature UFT machine developed by the author; (b) high-temperature module; (c) mounting relationship between special horn and high-temperature modules. The special horn designed by the author is shown in the blue dashed line; (d) shows the complex internal flow path of the special horn. The color bands on the right side indicate the temperature distribution $T(x)$, the stress distribution $\sigma(x)$, and the displacement distribution $U(x)$ along the length direction of the particular horn, respectively. (1) Ultrasonic module, (2) high-temperature module, (3) infrared thermal camera, (4) refrigerant tube, (5) special horn, (6) silicon molybdenum rod, and (7) ultrasonic specimen.

5.2 Vacuum and humidity environment

To investigate the effect of humidity on the near-threshold fatigue crack propagation of the material, Holper et al. [32] developed a UFT machine, as shown in Figure 28(a). The machine consists of a vacuum chamber and an ultrasonic component. The vacuum chamber consists of a stainless steel flange and a glass tube. A half-wavelength cylindrical rod is connected to the lower end of the ultrasonic horn, and a gasket is placed at the vibration node of the cylindrical rod to seal the vacuum chamber. The vacuum is evacuated using a mechanical pump and the vacuum level is monitored by a vacuum gauge. The output amplitude of the horn end is measured by a vibration meter. The sheet specimen with notched edges as shown in Figure 28(a) is fixed at the upper end of the half-wavelength cylindrical rod, and the lower end is free to realize full reverse loading. Video equipment with a magnifying lens is used for *in situ* measurement of the crack length during the test, with a resolution of up to 7 μm. It is worth noting that specimen cooling in a vacuum is a critical issue. In laboratory air, even without any forced cooling, the specimen temperature can be dissipated by air convection, heat conduction, and radiation. While in a vacuum, the least

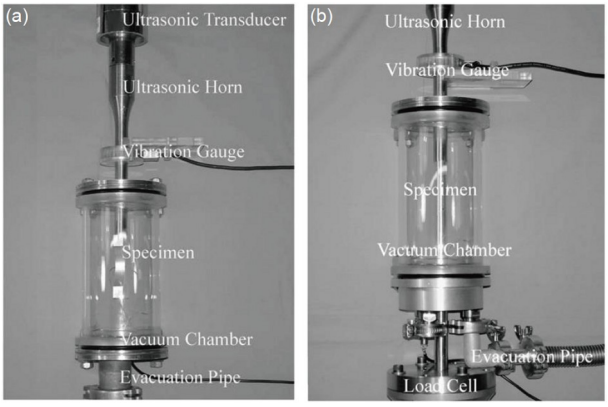

Figure 28 The vacuum UFT machine developed by Holper et al. [32,156]. (a) Test configuration at $R=-1$ [32]; (b) test configuration at $R\neq-1$ [156]. Copyright©2003, Elsevier; Copyright©2004, Elsevier.

efficient radiation cooling remains the only way to dissipate heat. Experiments by Geathers [155] in vacuum showed that even if the temperature rise in UF specimens is less than 10°C, it takes 90 min in the vacuum to cool to room temperature after stopping the loading. Therefore, only a smaller pulse loading time can be employed to avoid the temperature rise. Holper et al. [32] used a very short pulse loading time of

50 ms and a pause duration of 50–200 ms, which maintained the specimen temperature below 30°C in a vacuum. In subsequent work, Holper et al. [156] improved the machine to achieve UFT in a vacuum and under different stress ratios. As shown in Figure 28(b), a full-wavelength rod is added at the lower end of the specimen to the original machine. A gasket is placed at the vibration node at the upper end of the rod to seal the vacuum chamber, and the vibration node at the lower end is used to superimpose static loads. The test by Holper et al. [32,156] in vacuum and laboratory air (laboratory air at 18%–22°C and 40%–60% relative humidity) showed that humidity has a significant effect on the threshold stress intensity and crack propagation rate of aluminum alloys. In laboratory air, humidity reacts chemically with the newly formed surface of the crack tip, thereby reducing the threshold stress intensity and accelerating crack growth.

Geathers et al. [33,155] combined ultrasonic components with Philips XL30 ESEM to investigate the effect of different humidity on the crack propagation behavior of the material. Figure 29 shows the UFT machine developed by Geathers et al. [33,155], which consists of the ultrasonic component, the five-degree-of-freedom (DOF) manual displacement platform (McAllister Technical Services MB1500), and the Philips XL30 ESEM. Water vapor is introduced in the vacuumed ESEM chamber using a recirculation procedure to build a humidity environment. Water vapor is produced by heating a flask containing water. The specimen as shown in Figure 29 was used for the test. Three micro-notches of 30 μm long and approximately 15 μm deep are machined in the central area of the gauge section of each specimen using the FIB technique. The spacing between the notches is 1 mm. To avoid temperature rise in the vacuum, a pulse-pause ratio of 200 ms/3000 ms is used. The studies of Geathers et al. [33,155] based on this machine showed that the crack initiation time of Ti-6242S specimens decreased and the crack propagation rate increased with increasing water vapor pressure.

5.3 Corrosion environment

Schönbauer et al. [34] developed a novel machine to study the corrosion effect on the VHCF behavior of the material. As shown in Figure 30, the machine consists of an environmental simulation system and an axial UFT system. The axial UFT system consists of an ultrasonic component and a hydraulically loading frame. The ultrasonic component is connected to a hydraulically loading frame to realize a stress ratio range of −1 to 0.9. The environmental simulation system is a water circulation loop containing a 35 L reservoir, which consists of a solution reservoir, pump, test chamber, and various sensors. The fatigue crack propagation specimen as shown in Figure 30(b) is used. The specimen is a full wavelength tube with two displacement nodes at which the test chamber is connected. Schönbauer et al. [34,157] studied the fatigue life and near-threshold fatigue crack propagation of materials in different corrosive environments and at different stress ratios. The fatigue limits in air and degassed pure water are higher than those in the presence of chlorides and oxygen. However, the rate of near-threshold fatigue crack propagation in aqueous solutions is reduced due to the crack closure effect.

In addition to those reported in this review, several UFT machines have been developed in different environments. For example, low-temperature UFT machines [25,158], and high-pressure UFT machines [25].

6 *In situ* monitoring techniques of VHCF damage

The extremely short test time of the UFT machine and the development of the pulse-pause technique make it possible

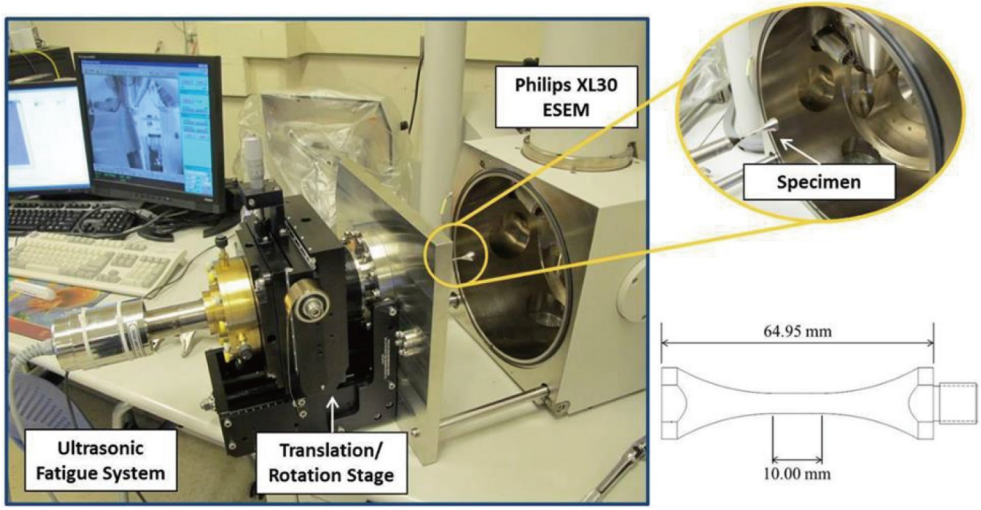

Figure 29 (Color online) *In situ* UFT machines for UFT in different gas environments [33,155]. Copyright©2014, Elsevier.

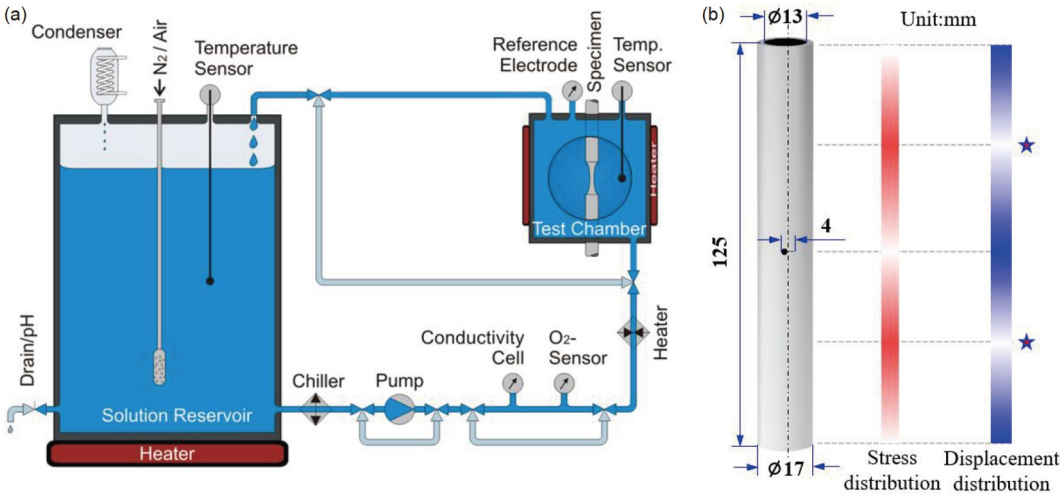

Figure 30 (Color online) (a) Shows the schematic diagram of the environmental simulation system [34]; (b) shape and size of fatigue crack propagation specimens. The blue pentagram shows the location of the displacement nodes, which are used to connect the test chambers. Copyright©2014, Elsevier.

to realize *in situ* monitors of VHCF damage during the entire VHCF test. *In situ* UFT machines based on optical microscopy (OM) [159,160] and scanning electron microscopy (SEM) [33,155] have been developed, which are applicable for the monitoring of surface crack initiation/expansion. However, subsurface crack initiation is a major feature of VHCF. When the crack appears inside the specimen, the above device is no longer applicable. *In situ* techniques capable of monitoring VHCF damage, both non-visualized and visualized, have been developed. This part of the review focuses on viable *in situ* testing techniques for monitoring VHCF damage during UFT.

6.1 DCPD technology

The direct current potential drop (DCPD) method is an important method used to monitor crack initiation and propagation in specimens [161]. The principle of DCPD is that the initiation and propagation of cracks in a metal specimen affect its resistance value, and the crack length can be deduced from the change in resistance value. DCPD shows good applicability and high accuracy in high-temperature, low-temperature, and corrosive environments. Therefore, DCPD is widely used in conventional low-frequency fatigue machines [162–166]. However, applying it to UFT is a challenge. Connecting a DCPD machine to a high-frequency vibrating load chain is difficult to achieve. Moreover, the ultrasonic vibration signal has a large interference with the DCPD signal. Müller and Sander [167] firstly developed the DCPD method that can be used at the ultrasonic frequency. As shown in Figure 31, a half-wavelength horn is connected in series at the lower end of the specimen. The purpose of that is to introduce a displacement node, which is necessary for fatigue testing either at R=−1 or R≠−1. A DC power supply is connected to the vibration nodes at the upper and lower horns of the specimen via copper clamps. A dog-bone specimen is used and the DCPD meter is attached to the surface of the specimen at a distance of 5 mm from the gauge center through narrow strips of self-adhesive copper films. This connection has been proven to be feasible without notch effects, and the additional mass introduced is negligible. Moreover, the specimen vibration will not cause the falling off or failure of copper films. The UFT is conducted with pulse-pause, where the DCPD measurement program is triggered during the pause, and the acquisition is stopped at the pulse time. This approach effectively avoids the interference of ultrasonic vibration signals to DCPD signals.

6.2 Acoustic emission

The phenomenon of releasing strain energy in the form of elastic waves when materials or components are deformed or cracked during loading is called acoustic emission (AE). AE technology is a technique for dynamic non-destructive testing of materials or components using received acoustic emission signals. The use of AE techniques in conventional low-frequency fatigue tests is a wide interest topic in AE research [168–172], but the application of AE methods in UFT has rarely been reported [173]. This is because the severe noise level of the UFT machine strongly interferes with the AE frequency response, and this noise cannot be suppressed by the cutoff or bandpass filters that most commercial AE systems are equipped with. In 2021, Seleznev et al. [174] developed an advanced AE technique applicable to UFT. The broadband AE sensor PICO was attached to the end of the ultrasonic horn. The AE system by Physical Acoustics Corp. (USA) was used to acquire AE waveforms. Real-time monitoring of output amplitude using a vibration meter. Seleznev et al. [174] determined the fatigue damage of the specimens effectively during UFT by the developed

technique. As shown in Figure 32, all the noise generated by resonance in AE was well filtered by adaptive STFT filtering, which is a more efficient and robust technique than resonance-based techniques.

6.3 Analysis of vibration properties

Analysis of vibration properties (AVP) is a method to assess fatigue damage of a specimen by monitoring its vibration properties [35], including methods based on nonlinear ultrasonic parameters, based on resonant frequencies, based on eigenmodes, and so on. Several studies in the 1990s demonstrated the possibility of nonlinear ultrasonic assessment of fatigue damage in materials [175–177]. The basic principle of the nonlinear ultrasonic technique is that microcracks generated during fatigue cause nonlinear distortions in the transmission of ultrasonic waves in the specimen, resulting in the second and higher harmonics of the fundamental frequency [178]. Studies by Kumar et al. [179,180] further refined such methods and demonstrated that nonlinear analysis of ultrasonic vibrometer signals for the detection of fatigue damage is feasible. The nonlinear ultrasonic parameter β is determined during the test by measuring the absolute amplitude of the fundamental displacement and second harmonic displacement signals [181–183]. The parameter β_{rel} is used as the parameter to evaluate the damage accumulation, $\beta_{rel}=\beta/\beta_0$ (β_0 indicates the undamaged material state). Mayer et al. [184] developed a high-precision vibration analysis system at Physics BOKU Vienna to monitor the variation of the nonlinear ultrasonic parameter β_{rel} specifically. Figure 33(a)–(c) shows the variation of β_{rel} during the UFT of 2024-T351 aluminum alloy.

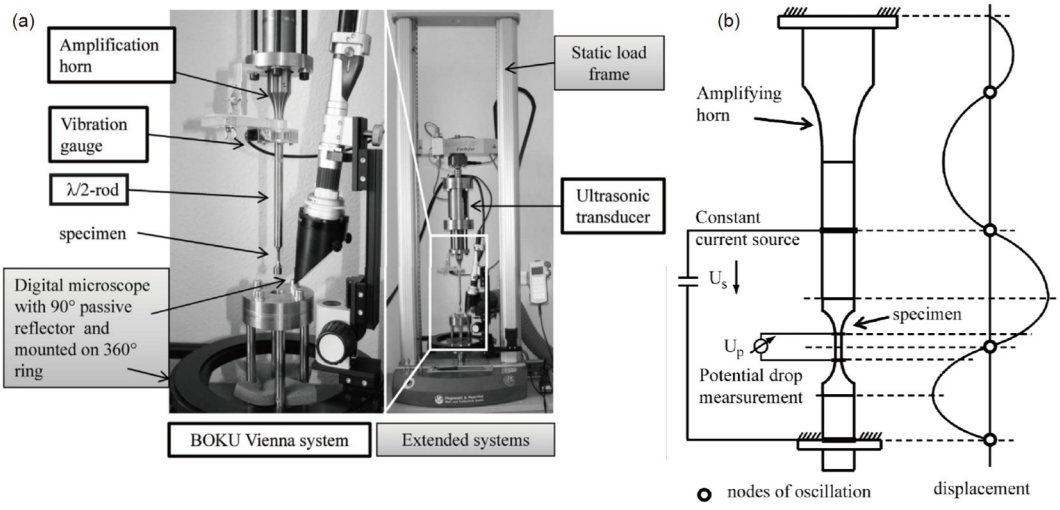

Figure 31 (a) Photograph and (b) schematic diagram of the DCPD technique applied in UFT [167]. Copyright©2013, Elsevier.

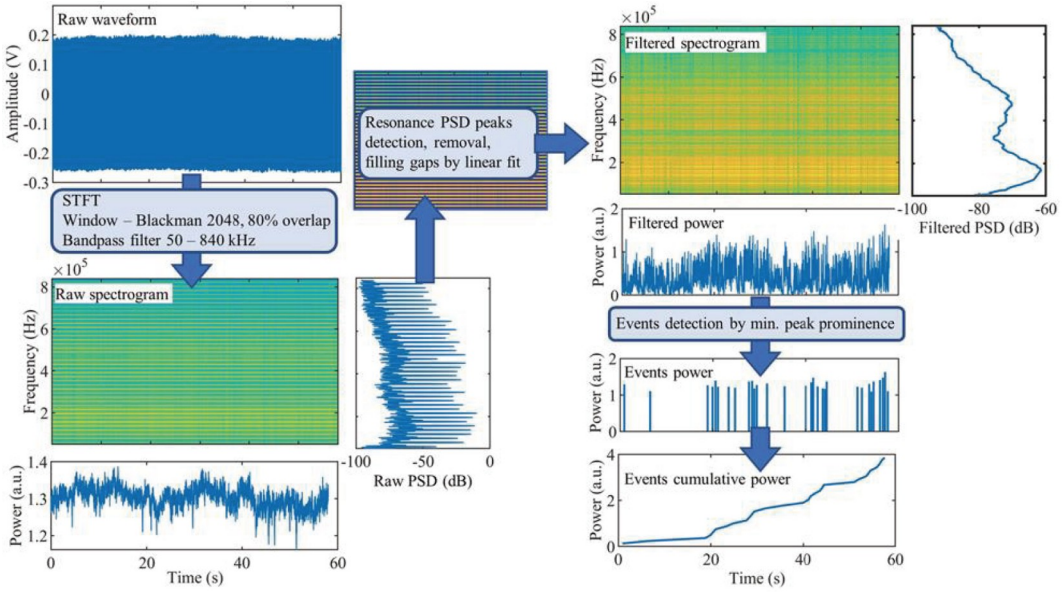

Figure 32 (Color online) Flowchart of the processing algorithm for analyzing the continuous AE signal [174]. Copyright©2021, Elsevier.

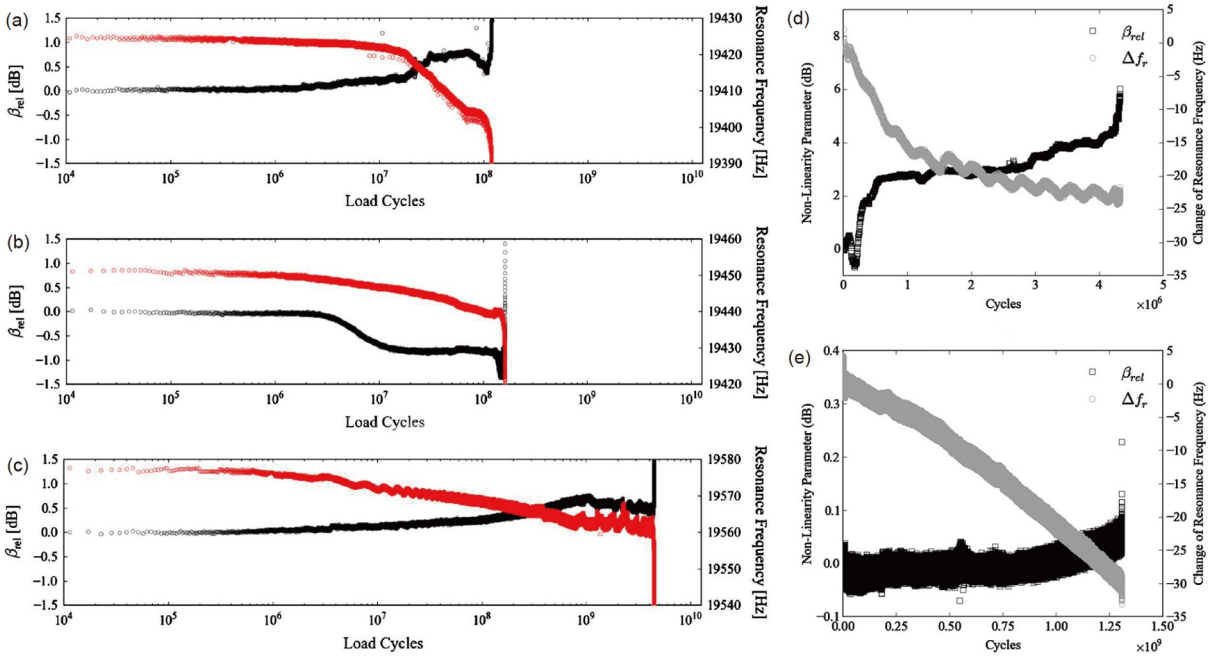

Figure 33 (Color online) (a)–(c) Variation of nonlinear ultrasonic parameters β_{rel} and resonant frequency during UFT of 2024-T351 aluminum alloy [184]; Copyright©2013, Elsevier. (d) and (e) show the results of *in situ* monitoring of the aluminum-silicon alloy DISPAL® S232 [185]. Copyright©2014, Wiley.

There was almost no change in β_{rel} before crack initiation, while a significant change in β_{rel} was observed before specimen failure. There is another novel method of *in situ* damage monitoring based on resonant frequency changes. The basic principle is that crack initiation and expansion lead to a stiffness reduction of the specimen and, thus a decrease in resonant frequency. The use of this method places higher demands on specimen temperature rise control, as even a low temperature rise of 0.4°C was shown to cause a frequency increase of 4 Hz. Mayer et al. [184] compared these two methods in an experiment conducted on 2024-T351 aluminum alloy. As shown in Figure 33(a)–(c), significant changes in the nonlinear ultrasonic parameters β_{rel} and resonant frequency associated with fatigue damage were monitored during the UFT. Figure 33(d) and (e) show the results of *in situ* monitoring of the aluminum-silicon alloy DISPAL® S232 by Fitzka et al. [185], where $\Delta\sigma/2$ is 259 MPa and 162 MPa, respectively, and the stress ratio R=−1. At different stress levels, the resonant frequency of the specimen exhibits the same trend, i.e., a continuous decreasing trend. The frequency fluctuation in Figure 33(d) is caused by the room temperature variation. In general, β_{rel} also exhibits a continuous rise and no stabilization phase. Both parameters together prove the fact that even in the VHCF stage, the fatigue damage of the aluminum-silicon alloy DISPAL®S232 is a complete crack propagation without a crack initiation stage. It is worth stating that β_{rel} is more sensitive to crack initiation and propagation compared with resonant frequencies [179,180].

In addition to the two types of vibration properties analysis methods mentioned above, Heinz et al. [186] provided a novel idea. Using a 3D laser scanning vibrometer (3D-SLV) by Polytec, Germany, three independent He-Ne laser heads are used to measure the oscillation velocity of the specimen surface in three orthogonal directions during the UFT process. As shown in Figure 34, the velocity distribution of the fatigue specimen in the Y-direction shows an asymmetric process due to the fatigue crack propagation and the change in oscillatory behavior. In addition, the inhomogeneous distribution of velocities in the X-direction locates the region where fatigue failure eventually occurs. This novel method allows for monitoring the eigenmodes of the specimen in different fatigue states and, thus, quickly locating fatigue damage areas.

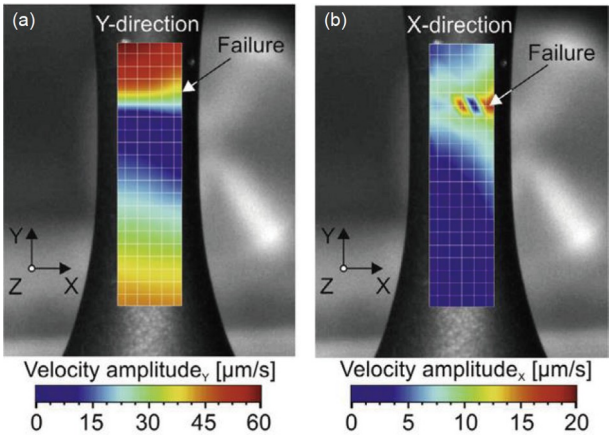

Figure 34 (Color online) Velocity amplitude distribution along the (a) Y-direction and the (b) X-direction of the gauge section of the UF specimen [186]. Copyright©2013, Elsevier.

6.4 Infrared thermal imager

The fatigue thermography method (also known as the Risitano method) is a method developed by Curti et al. [11] in 1986 for the rapid determination of fatigue limits of materials based on thermal imaging. This part of the review focuses on the application of infrared thermography as an *in situ* monitoring method in UFT, and the reader should be careful to distinguish the difference between the two. During the fatigue test, the evolution of the specimen's temperature can be divided into three stages [187–190]. Due to the presence of internal damping of the material, the temperature rise is inevitable at the beginning of fatigue loading [191]. The temperature will continue to increase until the value of heat conduction and natural heat dissipation is equal to the heat generated by the specimen [189], at which point the temperature value tends to stabilize. Subsequently, with the accumulation of microplasticity and the appearance of small cracks, the friction on the crack surface and the consumption of plastic work lead to a dramatic temperature rise [192]. Considering this, a large number of researchers have already applied infrared thermography for *in situ* monitoring of fatigue damage and crack initiation in materials [192–195]. In 2006, Xue et al. [193] conducted an early study by infrared thermography to *in situ* characterize the fatigue damage accumulated in steel (AISI 52100 and 42CD4) and cast iron (GS51) during UFT. During the steady loading stage, the maximum temperature region appears at the center gauge section due to the highest stress level there. Although the temperature distribution was not uniform here, no abrupt local temperature changes were observed. When the cracks sprouted, a distinct local temperature rise region was observed and the region expanded rapidly in a relatively short time period. This study shows that it seems feasible to determine the timing and location of crack initiation by *in situ* monitoring of specimen temperature changes with a high-resolution infrared thermography. Naoe et al. [195] studied the *in situ* UF behavior of 316L using infrared thermography. As shown in Figure 35(a), the temperature distribution in the specimen is measured in real time using an infrared thermography. As shown in Figure 35(b), a significant local temperature rise of the UF specimen was captured before the fracture of the UF specimen. The number of cracks and the crack location shown in the micrographs are almost consistent with the area of significant local temperature rise (as shown in Figure 35(c)). As shown in Figure 36, the study using notched plate specimens further confirms that the significant localized temperature rise for fatigue failure is attributed to crack initiation and propagation, and that the highest temperature point occurs at the tip of the crack.

In situ monitoring with single infrared thermography has two potential drawbacks. First, for conventional circular rod UF specimens, cracks appear randomly in the highly stressed volume within their gauge section. If the crack initiation point appears on the other side of the infrared thermography, it may lead to a delayed appearance of the local temperature rise, which may trigger a misjudgment of the crack initiation timing. Moreover, it seems infeasible to determine the lo-

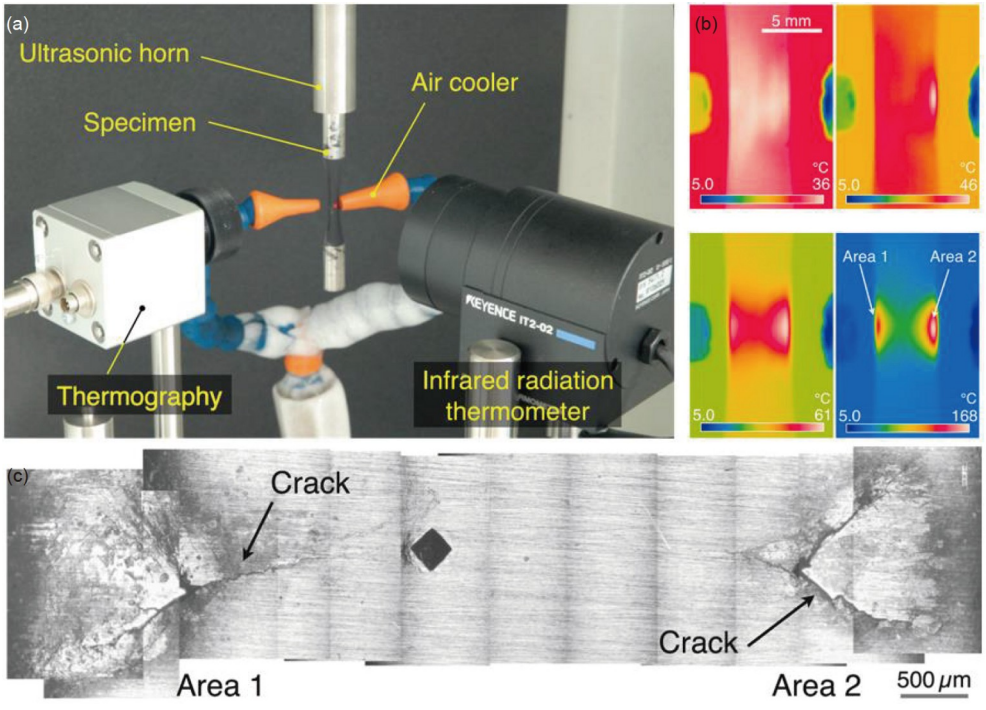

Figure 35 (Color online) (a) UFT machine based on infrared thermography for *in situ* monitoring [195]; (b) temperature distribution on the surface of the specimen, modified from [195]. (c) fatigue cracks on the surface of the specimen captured by a digital microscope [195]. Copyright©2018, Elsevier.

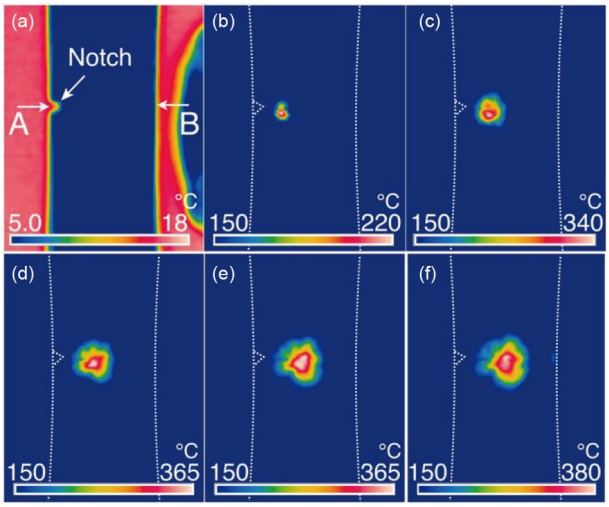

Figure 36 (Color online) (a)–(f) The temperature distribution on the surface of the notched plate specimen [195]. Copyright©2018, Elsevier.

cation of the crack initiation point based on one infrared thermography. It is necessary to arrange at least three infrared thermography in the circumferential direction of the specimen. But this is unacceptable from a cost perspective. To address these issues, Krewerth et al. [194] developed a full surface view *in situ* infrared thermography system. As shown in Figure 37, the system employs infrared thermography and two mirrors. The mirrors are made of ground and polished aluminum sheets (AlMgSi1, EN AW 6082). The mirrors are arranged at an angle of 45° toward the infrared thermography. During the test, the front side of the specimen is monitored directly by infrared thermography and the back side of the specimen is monitored indirectly by two mirrors. Figure 37(c) shows the different sizes of heat sources identified by direct and indirect thermography. The crack initiation point identified by visual illustration matched well with the final fracture location. Compared with conventional infrared thermography-based methods, this system can determine the crack initiation time more accurately, and can precisely locate the crack initiation location.

6.5 X-ray CT

X-ray computed tomography (X-ray CT) is a non-destructive method for the three-dimensional (3D) measurement of structures. The evolution of the structure over time is monitored by repeated image acquisition extensions [196]. Therefore, it is becoming an emerging method to investigate the damage accumulation, crack initiation, and propagation during the fatigue of materials [197–202]. X-ray CT is based on a series of digital radiographs captured with high spatial resolution. Between each photograph, the specimen is rotated by a small angular increment. Images are typically created with parallel beam, fan beam, or cone beam illumination. Image contrast is produced in the specimen by changes in attenuation. For phase contrast imaging, the image contrast is produced by the change in the refractive index. Generally, a projected photograph is taken over a 180° rotation angle, and then a 3D image with varying contrast is mathematically reconstructed.

The earliest *in situ* UFT conducted with X-ray CT dates back to 2008 [197]. Liu et al. [197] developed a portable UFT machine integrated into the Advanced Photon Source (APS) 32-ID synchrotron X-ray system at Argonne National Laboratory to conduct *in situ* X-ray CT for the fatigue crack propagation process. The portable UFT machine is mounted on a rotating positioning platform as shown in Figure 38. A combined specimen is used, where the carrier specimen is made of Ti-6Al-4V alloy and is designed to have a longitudinal vibration frequency of 20 kHz. Edge-notched microscopic specimen with a thickness of 140–170 μm is fixed on the carrier specimen to achieve UF load transfer. These microscopic specimens are thin enough to allow for at-

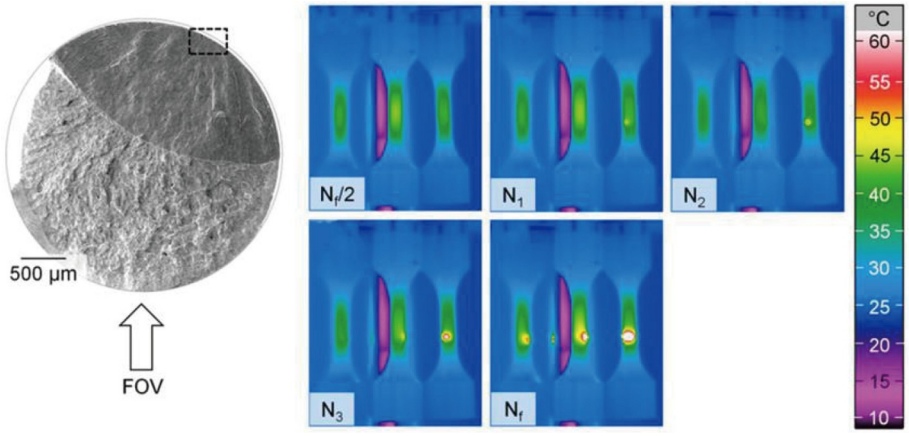

Figure 37 (Color online) (a) Schematic diagram of the full surface view *in situ* infrared thermography system; (b) experimental configuration for full surface view *in situ* infrared thermography during UFT [194]; (c) fracture morphology and representative full-surface thermal image of the specimen, modified from [194]. Copyright©2015, Elsevier.

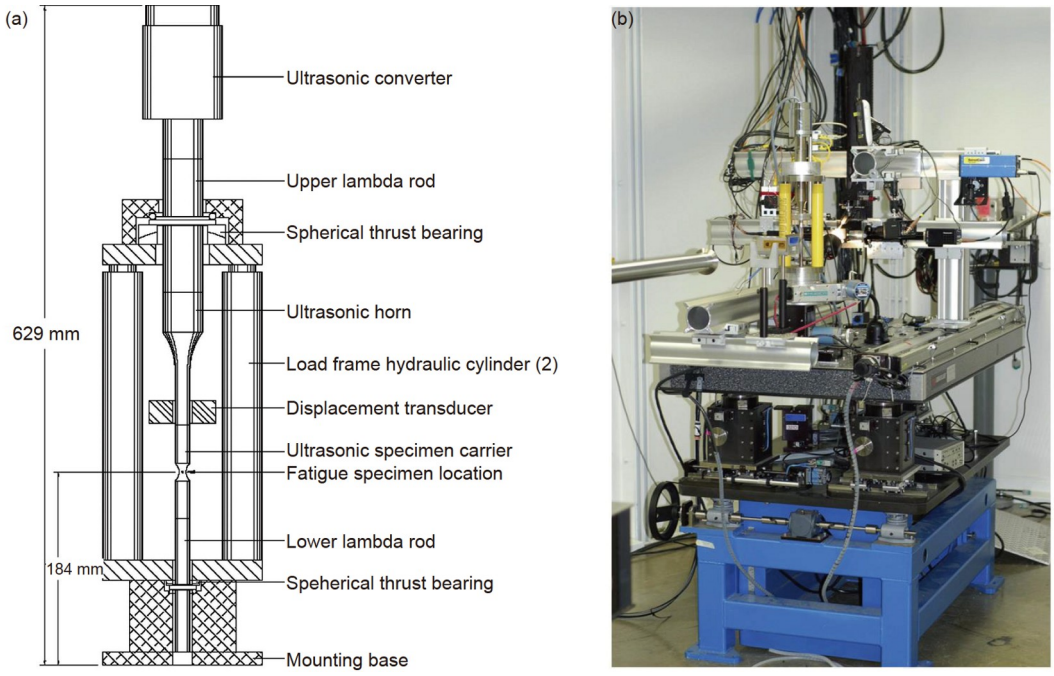

Figure 38 (Color online) (a) Schematic diagram and (b) photogram of *in situ* UFT using synchrotron X-rays, modified from [198]. Copyright©2011, Elsevier.

tenuation-free dynamic imaging in transmission using coherent, high-brightness X-rays. A 2 mm through-hole is provided in the middle of the carrier specimen to allow the penetration of the X-ray beam. This combination allows the carrier specimen to be used multiple times without failure. Preliminary tests based on this system proved that the system can successfully capture three-dimensional information about compositional segregation, microstructure, fracture topography, and fatigue crack propagation of the nickel-based single-crystal superalloy CMSX-4 [197,198].

In a recent study, Messager et al. [200] developed a novel *in situ* synchrotron UFT system. As shown in Figure 39(a) and (b), the system contains a UF module, static load module, and *in situ* monitoring module. The UF module is connected to the static load module by a vibrating node at the horn and a convex shoulder at the end of the specimen to keep the cracks open by applying a static load during imaging. The static load module and the *in situ* monitoring module are mounted on the rotating platform of the synchrotron to enable rotation around the loading axis. The *in situ* monitoring module mainly contains a synchrotron CT device, an infrared thermography camera, and a crack detection device based on FFT real-time analysis. To prevent the loss of the CT view, a polymethylmethacrylate (PMMA) tube is mounted on the sleeve holding the UF module. Multiple in situ monitoring processes based on the system are provided: (1) Start UF module for full reverse UFT in continuous loading mode. The temperature distribution of the specimen surface is monitored in real-time using an infrared thermography camera, and the crack initiation time is monitored in real-time using FFT analysis. Once the crack initiation is monitored, the loading process is quickly terminated. (2) CT and 3D reconstruction of cracks. Perform the load pulse-pause procedure shown in Figure 39(d) at this step. A static load of 80% of the cyclic stress amplitude is applied to keep the cracks open during the ultrasonic pause time, and the specimens are tomographed at the gauge volume. It takes about 20 min to rebuild the complete volume. Figure 39(c) shows the 3D rendering results of the internal defects and internal cracks of the specimen after different loading cycles. The system demonstrates significant advantages. Capable of automatically monitoring the initiation of small cracks in real-time, and able to perform three-dimensional reconstruction of cracks by a synchrotron. With the continuous development and improvement of *in situ* monitoring technology, the development of UFT technology based on multiple in situ imaging will be the future development direction.

6.6 Comparison of VHCF damage*in situ* monitoring techniques

In general, research on *in situ* monitoring techniques has increased in recent years. It has become a trend to pair UF testing with one or more *in situ* monitoring techniques to better understand the VHCF crack initiation and propagation behavior of the material. Table 4 compares the advantages and disadvantages of OM, SEM, DCPD, AE, AVP, Infrared thermal imager, and X-ray CT techniques.

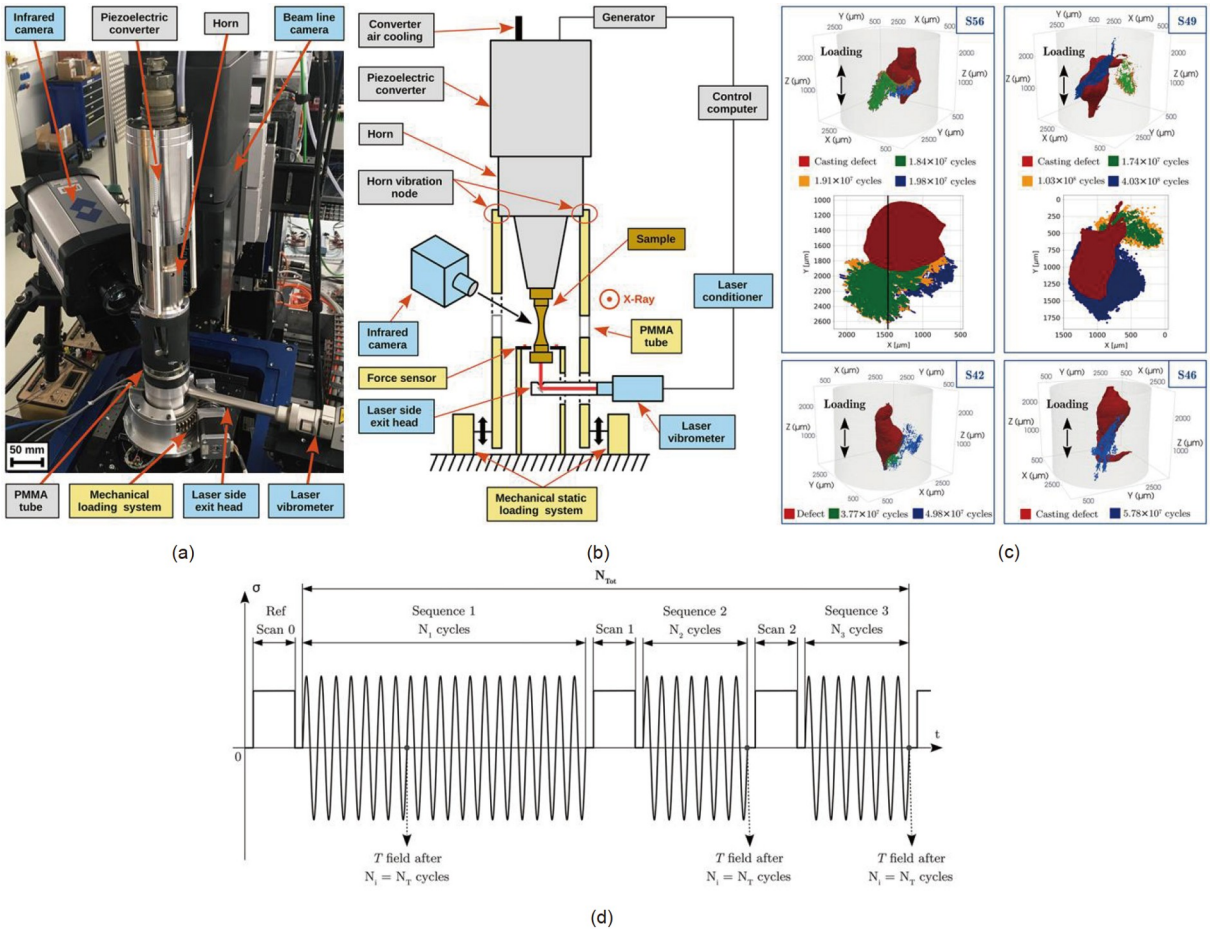

Figure 39 (Color online) (a) Photogram and (b) schematic diagram of the novel *in situ* synchrotron UFT machine [200]; (c) 3D rendering of internal defects and internal cracks in the specimen after different load cycles, modified from [200]; (d) loading procedure during tomography [200]. Copyright©2020, Wiley.

7 Key issues in ultrasonic fatigue testing

7.1 Estimation of specimen stress

The stress estimation of UF specimens is a key issue in UFT, which is directly related to the accuracy of UFT data. Accurate estimation of stress at such high frequencies is not easy, and four possible approaches are available. (1) The strain gauges are attached to the gauge section of the specimen to obtain the strain and the measured strain is converted to stress by Hooke's law [18,26,27]. The specimen is loaded with low-stress amplitude to obtain purely elastic deformation as far as possible, ignoring the possible plasticity. Although the strain gauge-based method has the highest accuracy, the strain gauges may accumulate damage or even fall off or fail during the stress estimation process. (2) The vibration amplitude at the end of the specimen is measured using a laser Doppler vibrometer or an induction coil assembly, and the stress amplitude of the gauge section is calculated by combining the stress displacement coefficients derived from FEA or theoretical methods [18,25,200]. It is worth stating that this is the most widely used method of stress estimation and is applicable for any shape and size of UF specimen. (3) Stress estimation method based on X-ray diffraction [201].(4) Stress estimation method based on 3D laser scanning vibrometer [186]. This method shows great advantages for stress estimation in orthotropic anisotropic composites. A study by Jacquemain et al. [205] showed that the uncertainties of the previous three stress estimation methods were 3%, 3.2%, and 10%, respectively.

7.2 Specimen heating

Different from testing at conventional frequencies, the heating of the specimen at ultrasonic frequencies is a problem that should not be ignored. In general, specimen heating under cyclic loading is caused by the internal damping of the material. The specimen heating depends on the material, test frequency, and stress level [193]. Weakening of the strength and microstructure changes (e.g., precipitate coarsening and grain growth) of the material due to heating may affect fatigue performance. To address this temperature increase, there are three possible methods. (1) The UFT is usually operating in pulsed pause mode, with specimens cooling off during the pause time. But it is worth stating that

Table 4 Comparison of VHCF damage *in situ* monitoring techniques[a)]

In situ monitoring techniques	Principle	Advantages	Disadvantages	Reference
OM	Capture microscopic images of the specimen surface damage by optical magnification	Non-contact Visualization Cheap equipment Easy operation Determine the location of crack initiation Determine the crack length and number of cycles Identifying crack propagation modes High sensitivity*	Cannot monitor internal cracks Need close to the specimen Need to determine the crack location in advance Need to interrupt UFT	[159]
SEM	The surface of the specimen is scanned using a high-energy electron beam and the detector captures the excitation information to produce a grayscale image of the surface damage	Non-contact Visualization Determine the location of crack initiation Determine the crack length and number of cycles Identifying crack propagation modes High sensitivity*	Cannot monitor internal cracks Equipment is expensive and SEM needs to be modified to accommodate UFT Need to determine the crack location in advance Need to interrupt UFT	[33,155,203]
DCPD	Monitor the voltage at the gauge section of the specimen and reflect the damage level of the specimen by the DC voltage drop	Can detect internal cracks Identifying the crack initiation time Determine the crack length and number of cycles Identifying crack propagation modes medium sensitive*	Difficulty in contacting high-frequency vibrating specimens Scattering due to contact Need to interrupt UFT	[167]
AE	Monitoring the damage level of a specimen by receiving and analyzing the acoustic emission signal from the specimen	Can detect internal cracks Identifying the crack initiation time Determine the crack length and number of cycles Identifying crack propagation modes No need to interrupt the test High sensitivity*	Difficulty in background noise suppression	[174]
AVP	Damage monitoring through analysis of specimen vibration characteristics	Can detect internal cracks Identifying the crack initiation time No need to interrupt the test medium sensitive*	Difficulty in determining crack length and number of cycles Difficulty in identifying crack propagation modes Sensitive to specimen temperature rise	[178–186]
Infrared thermal imager	Capture the time, location and extent of damage by temperature changes within the gauge section of the specimen	Non-contact Visualization Determine the location of crack initiation Can detect internal cracks Identifying the crack initiation time Determine the crack length and number of cycles	Difficulty in identifying crack propagation modes Poor sensitivity*	[192–195]
X-ray CT	X-ray penetration of the specimen, imaging through the detector, reconstructing the damage pattern of the specimen	Non-contact Visualization Determine the location of crack initiation Can detect internal cracks Crack morphology reconstruction	Expensive equipment, restricted access Medium sensitive* Need to interrupt UFT	[197–200]

a) *The length of identifiable cracks of several microns to 10 microns is considered to be highly sensitive, the length of identifiable cracks of 10 microns to 100 microns is considered to be medium sensitive, and the length of identifiable cracks above 100 microns is considered to be poor. For more information refer to the ref. [204].

the effect of the pulse-pause technique, the most widely used cooling technique, on the fatigue life of materials is highly controversial [150,206–208]. Sun et al. [208] showed that the pulse-pause technique significantly affects the lifetime of the material. However, Cervellon et al. [150] reached a different result on this. Given that the temperature rise is related to various factors such as material and stress levels, and different pulse-pause ratios have been used in different studies. Even, different pulse-pause ratios were set for different stress levels in one study [209]. An in-depth study of the effect mechanism on the fatigue life of the material is urgently needed. (2) Cooling by compressed cold air, low-temperature nitrogen, etc., to avoid such specimen heating. In general, a tem-perature rise below 40°C is considered to not affect the experimental results [193]. (3) Reduction of heating is achieved by using small-size thin-plate specimens or by optimizing the specimen geometry [210]. The available techniques that are feasible for specimen cooling are summarized in Table 5.

Table 5 Temperature rise and cooling method used as reported in ultrasonic fatigue testing

Load type	Test environment	Materials	Stress ratio R	Reported temperature rise (°C)	Cooling method	Reference
Axial tension-compression/ tension-tension	laboratory air	Ti-6Al-4V	−1, −0.5, −0.1, 0.1, 0.5	—	Compressed cold air	Liu et al. [211] (2015)
	laboratory air	Ti-8Al-1Mo-1V	−1, 0.1, 0.5	12–16	Compressed cold air	Yang et al. [212] (2017)
	laboratory air	Wrought and AM Inconel 718	−1	<30	Pulse-pause technique	Muhammad et al. [213] (2021)
	laboratory air	VR434GI96/EPI-KOTE 04,434 (Glass/Epoxy)	0.1	5	Pulse-pause technique	Flore et al. [214] (2017)
	laboratory air	GF30/PA66 (Glass/ Polyamide)	−1	<10	Pulse-pause technique + Peltier cooling device	Lee et al. [215] (2019)
	1000°C	PWA 1484	−1	<3	Pulse-pause technique	Yi et al. [31] (2007)
	650°C, 1000°C	12Cr-2W, CMSX-4, TMS138A	−1, 0	<5	Pulse-pause technique	Furuya et al. [216] (2012)
	750°C, 850°C	DZ125	−1	<5	Pulse-pause technique	Zhao et al. [209] (2020)
	laboratory air	TiAl alloy	0.5	—	Compressed cold air	Xue et al. [21] (2007)
	laboratory air	Ti-6Al-4V	0.4	~70	Sprayer with compressed air	Wang et al. [131] (2021)
Three-point bending	laboratory air	CF-PPS (Carbon/ Polyphenylene sulfide)	0.29–0.49	5–20	Pulse-pause technique	Backe et al. [91] (2015)
	laboratory air	CF-PPS (Carbon/ Polyphenylene sulfide) CF-EP (Carbon/ Epoxy)	0.05–0.51	<20	Pulse-pause technique	Weibel et al. [94] (2017)
	laboratory air	T300/ YPH-160	0.4	—	Compressed cold air-liquid nitrogen composite refrigeration method	Ding and Cheng [95] (2021)
Cantilever bending	laboratory air	TC17 Titanium Alloy	−1	—	Low-temperature nitrogen	Jiao et al. [101] (2016)
	laboratory air	Ti-6Al-4V	−1	<5	Compressed cold air	Yang et al. [23] (2022)
	laboratory air	VDSiCr spring steel	0.1, 0.35, 0.5	<5	Pulse-pause technique + Compressed cold air	Mayer et al. [105] (2015)
Torsion	laboratory air	38MnV5S	−1	<3	Compressed cold air	Marinesgarcia et al. [109] (2007)
	laboratory air	50CrV4 and 16MnCr5	−1	—	The continuous flow of water charged with an inhibitor against corrosion	Petit et al. [110] (2021)
Fretting	laboratory air	GCr15	−1	—	Compressed cold air	Teng et al. [119] (2019)
	laboratory air	FV520B	−1	—	Greenhouse water	Song et al. [100] (2016)
Biaxial bending	laboratory air	AlSi7Cu05Mg03 T7	0.1	40–60	Compressed cold air	Brugger et al. [26] (2017)
Combined tension-torsion	laboratory air	N 13262 + A1 metal	0.57	<30	Pulse-pause technique	Reis et al. [217] (2020)
Combined tension-bending	laboratory air	Ti-6Al-4V	0.4	—	Compressed cold air	Wang et al. [131] (2021)
	laboratory air	Ti-6Al-4V	0.4	—	Low-temperature nitrogen	Zhao et al. [29] (2021)

7.3 Frequency effect

The aviation gas turbine engine blade is subjected to vibration loads in the range of several thousand Hz during service, while the UFT technology, an accelerated test technique, operates at 20 kHz and uses extremely small specimen sizes. A natural question is whether the data obtained by UFT can be used to assess the fatigue performance of blade materials in service. A key issue with the availability of UFT data is the frequency effect. Strain rate and environmental effects are considered to be the main causes of frequency effects in UFT [218]. Frequency effects may occur for highly ductile and strain-rate sensitive materials or for time-dependent processes. In general, the frequency effect of materials with a body-centered cubic lattice (BCC) is explained by the strain rate sensitivity. For metals with face-centered cubic lattices (FCC), the frequency effects are explained by environmental effects [218,219]. It is worth stating that the fatigue properties of the material are influenced by multiple factors coupled. Therefore, other fictitious effects introduced due to the test procedure should be excluded before investigating frequency effects [4,18], such as the effects of the specimen shape and size, the effects of temperature rise, and the effects of load type. Significant frequency effects due to strain rate sensitivity have been found in BCC materials such as annealed cp tantalum [220,221], low carbon steel [35,222], and medium carbon ferritic steel [35,223]. In this case, UFT generally obtains a higher fatigue life, which is mainly attributed to the greater yield strength due to the increased strain rate. While for FCC materials such as aluminum alloys [18,32,35,219], high-strength steels [224], titanium alloys [5,225], and nickel alloys [226], environment-related frequency effects have been reported, which correspond to surface crack initiation cases. For subsurface crack initiation, environmental effects no longer work. Therefore, none of the above materials exhibited frequency effects [225,227–229]. A typical example is that for aluminum alloys 2024-T3 and 7075 [32], higher crack propagation rates at lower frequencies were observed in ambient air, which did not occur in vacuum. It is worth noting that data on the frequency effects of blade materials in the VHCF regime are still in the accumulation stage. Limited by the length of the article, more information about frequency effects can be found in recent important literature [230].

7.4 Size effect

Another key issue in UFT is the size effect, which here refers to the potential effect on fatigue performance due to differences in UF specimen size and shape from the actual blade. On this issue, some existing theories can address it well, for example, high-stress volume [231], weakest link theory [232–234], critical defect method [235,236], etc.

In 1961, Kuguel introduced the concept of high-stress volume V_{Ξ} [231]. V_{Ξ} refers to the volume of material subjected to a stress higher than Ξ times the maximum stress in the part or specimen under investigation. Typically, 90 or 95 percent volume is used. In the original article, Kuguel [231] pointed out the power-law correlation between the fatigue strength σ_{lim} of the material and the high-stress volume V_{Ξ}. For internal crack initiation within the VHCF regime, the above relationship is applicable. For most cases of surface crack initiation, the concept of high-stress surface area A_{Ξ} is considered [237–240]. Based on the above relations, some questions about geometric size effects can be well answered [232,241,242]. In general, the fatigue strength σ_{lim} decreases as the specimen size increases [243–246]. For more information on high stress volumes refer to the review by Jeddi and Palin-Luc [247]. The weakest link theory [232,233] can also provide a good answer to the size effect. In addition, the critical defect method has also proven to be effective [235,236]. Zhu et al. [248] introduced the weakest link theory and the critical defect method in detail in their review and compared the two. Readers who are interested in this can refer to the literature [248], which will not be repeated in this paper. The details of the size effect cannot be described in this paper due to the limitation of length, more information on this topic can be found in the following important special topics reviews [248,249].

To study the size effect, specimens with different geometric dimensions [250] or different geometric types [246,251–254] are generally used. For example, hourglass, dogbone, and Gaussian specimens [253]. The basic idea is to construct different risk volumes by the selection of specimen size and specimen type. In general, the Gaussian specimen has a significantly larger risk volume, followed by the dogbone type, and the hourglass type has the smallest. It is worth stating that when focusing on size effects, the interference of other factors, such as frequency effects, should be avoided to be introduced during the test. Unless the frequency effect is known without significant effect on the material under investigation.

8 Future trends

During the past 20 years, UFT technology has been rapidly developed. Existing UFT apparatus has been equipped with rich functional modes, which can meet the VHCF test of structural materials in aerospace, rail transportation, and nuclear industry better. In the author's opinion, for further development of UFT technology, more research needs to be invested in the following aspects in the next 10–20 years.

(1) Develop standardized ultrasonic fatigue testing methods based on consensus among researchers. Although a standard has been developed for UFT [255], this standard

only covers axial tension and torsion and does not apply to other load types. Therefore, when developing a standardized method, all load types should be included, and factors such as specimen size, setting of pulse-pause ratio, specimen temperature rise, and stress estimation also need to be carefully considered.

(2) In-depth investigation of frequency effects. Some studies have been reported on the effect of loading frequency on the fatigue life of blade materials in the VHCF regime, but it is still at the data accumulation stage. The frequency effects, especially frequency effects in different environments, need to receive continuous attention. It is worth noting that the introduction of potential influences such as geometric size effect, load size effect, and temperature rise effect should be avoided as much as possible when studying frequency effects.

(3) Further development of multiaxial loading technology. Multiaxial UFT technology is a novel technology developed in recent years, the multiaxial VHCF data of blade materials are still very scarce, and the effect pattern of multiaxial stress on the VHCF behavior of blade materials needs to be further revealed.

(4) Further development of variable amplitude (VA) loading technology and CCF testing technology. Further development of VA technology, the multiaxial CCF (such as the CTB-CCF technology proposed by the author) technology, VA-CCF technology, etc. The development of these techniques will provide the possibility for fatigue life testing of blade materials close to the real service spectrum.

(5) Development of advanced *in situ* monitoring techniques for VHCF damage. Development of advanced *in situ* monitoring methods to investigate the formation and evolution of crack initiation and initial propagation processes in VHCF, especially in the fine grain area (FGA) crack initiation features in the tens of μm range. For example, the development of advanced *in situ* techniques such as micro-CT, Nano CT, neutron diffraction applicable to UFT, and even the coupling of multi-modal *in situ* monitoring techniques [256,257].

9 Summary

The demand for very-high-cycle fatigue (VHCF) testing of aviation gas turbine engine blade materials under complex loads and extreme environments up to 10^{10} cycles has stimulated the development of VHCF machines and technologies. This paper systematically compares several feasible VHCF testing techniques and comprehensively reviews new advances in UFT technology in terms of mechanical loading, environment construction, and *in situ* characterization. Key issues in UFT are highlighted, followed by future trends in this field. The following important conclusions can be drawn.

(1) Several existing viable VHCF testing techniques are introduced and compared in this paper, including the rotation bending technique, electromagnetic/electrohydraulic resonance technique, vibration-based technique, and UFT technique. After a comprehensive comparison, the UFT technique operating in the 20 kHz range is considered the most suitable technique to study the VHCF properties of blade materials.

(2) New features and methods of UFT technology are systematically presented for mechanical loading, including axial tension, three-point bending, cantilever bending, torsion, fretting, and multiaxial fatigue. In addition, the variable amplitude (VA) loading technique, and the combined cyclic fatigue (CCF) technique, which have been actively developed in the last decade, are also reported.

(3) UFT technology is reported for different environments, including high-temperature, humidity, and corrosive environments.

(4) The development of *in situ* monitoring techniques that can be used in conjunction with UFT machines is also reviewed, which creates the conditions for real-time monitoring of VHCF damage in blade materials. Finally, several key issues existing in UFT technology are summarized.

(5) Several key issues in the UFT technique are summarized, including specimen stress estimation, specimen heating, frequency effects, and size effects.

(6) In addition, the future trends of the UFT technique in the next 10–20 years are proposed, which are of some reference value to researchers and engineering designers in this field.

Although the author has attempted to write a compact review, the wealth of testing techniques has greatly increased the length of the article. Studies on the fatigue mechanisms of materials are beyond the scope of this paper, and the reader can refer to some important reviews in recent years. Although this paper starts with the testing of aircraft blade materials, all the techniques reported in this paper are also applicable to metallic materials and most composite materials. It is worth stating that the author briefly describes the application of UFT in typical blade materials, titanium alloys and nickel-based superalloys in the Supplementary File.

This research was funded by the National Science Fund for Distinguished Young Scholars (Grant No. 51925504), the National Key R and D Program of China (Grant No. 2018YFF01012400), the National Key R&D Program of China (Grant No. 2022YFA1604000), the National Major Scientific Research Instrument Development Project (Grant No. 52227810), the Foundation for Innovative Research Groups of the National Natural Science Foundation of China (Grant No. 52021003), the National Natural Science Foundation of China (Grant No. 52075220), the Jilin Provincial Department of Science and Technology Fund Project (Grant No. 20210101056JC).

1 Cao J, Tian S, Yang Z, et al. Blade tip timing signal filtering method based on sampling aliasing frequency map. IEEE Trans Instrum

Meas, 2022, 71: 1–12
2 Zhao J, Wang K, Ren Z, et al. A novel composite deformation measurement method of materials under coupling of high-temperature and hybrid tensile-flexural loads. IEEE Trans Instrum Meas, 2022, 71: 1–11
3 Shanyavskiy A A. Very-high-cycle-fatigue of in-service air-engine blades, compressor and turbine. Sci China-Phys Mech Astron, 2014, 57: 19–29
4 Nicholas T. High Cycle Fatigue-A Mechanics of Materials Perspective. Oxford: Elsevier, 2006
5 Morrissey R J, McDowell D L, Nicholas T. Frequency and stress ratio effects in high cycle fatigue of Ti-6Al-4V. Int J Fatigue, 1999, 21: 679–685
6 Standard M. Engine structural integrity program (ENSIP). MIL-STD-1783, USAF, 1984
7 Nicholas T, Zuiker J R. On the use of the Goodman diagram for high cycle fatigue design. Int J Fract, 1996, 80: 219–235
8 Cowles B A. High cycle fatigue in aircraft gas turbines—An industry perspective. Int J Fract, 1996, 80: 147–163
9 Naito T, Ueda H, Kikuchi M. Observation of fatigue fracture surface of carburized steel. J Soc Mater Sci Jpn, 1983, 32: 1162–1166
10 Tanaka T, Iwaya T, Sakai T. Statistical distributions of fatigue life and fatigue strength of low carbon steel in long life region. J Soc Mater Sci Jpn, 1983, 32: 1038–1043
11 Curti G, La Rosa G, Orlando M, et al. Analisi tramite infrarosso termico della temperatura limite in prove di fatica. XIV Convegno Nazionale AIAS. Catania, 1986. 23–27
12 Stanzl S, Tschegg E, Mayer H. Lifetime measurements for random loading in the very high cycle fatigue range. Int J Fatigue, 1986, 8: 195–200
13 Engine Structural Integrity Program Military Handbook. MIL HDBK-1783B. United States Air Force, 2002
14 Yamaguchi K, Abe T, Kobayashi K, et al. Gigacycle fatigue data sheets for advanced engineering materials. Sci Tech Adv Mater, 2007, 8: 545–551
15 Morgan J M, Milligan W W. A 1 kHz servohydraulic fatigue testing system. High cycle fatigue of structural materials Warrendale, PA: TMS. 1997. 305–312
16 Nicholas T. Step loading for very high cycle fatigue. Fatigue Fract Eng Mat Struct, 2002, 25: 861–869
17 George T J, Seidt J, Shen M H H. Development of a novel vibration-based fatigue testing methodology. Int J Fatigue, 2004, 26: 477–486
18 Stanzl-Tschegg S. Very high cycle fatigue measuring techniques. Int J Fatigue, 2014, 60: 2–17
19 Mason W P, Baerwald H. Piezoelectric crystals and their applications to ultrasonics. Phys Today, 1951, 4: 23–24
20 Neppiras E. Techniques and equipment for fatigue testing at very high frequencies. Proc ASTM, 1959
21 Xue H Q, Tao H, Montembault F, et al. Development of a three-point bending fatigue testing methodology at 20 kHz frequency. Int J Fatigue, 2007, 29: 2085–2093
22 Cheng L, Gao C, Shen J, et al. Investigation of very high cycle fatigue behavior of TC17 alloy. In: Proceedings of the International Conference on Advanced Engineering Materials and Technology (AEMT2011). Sanya , 2011
23 Yang D, Tang S, Hu Y, et al. A novel model of ultrasonic fatigue test in pure bending. Materials, 2022, 15: 4864
24 Mayer H. Ultrasonic torsion and tension-compression fatigue testing: Measuring principles and investigations on 2024-T351 aluminium alloy. Int J Fatigue, 2006, 28: 1446–1455
25 Bathias C. Piezoelectric fatigue testing machines and devices. Int J Fatigue, 2006, 28: 1438–1445
26 Brugger C, Palin-Luc T, Osmond P, et al. A new ultrasonic fatigue testing device for biaxial bending in the gigacycle regime. Int J Fatigue, 2017, 100: 619–626
27 Vieira M, Reis L, Freitas M, et al. Strain measurements on specimens subjected to biaxial ultrasonic fatigue testing. Theor Appl Fract Mech, 2016, 85: 2–8
28 Bao X, Cheng L, Ding J, et al. The Effect of microstructure and axial tension on three-point bending fatigue behavior of TC4 in high cycle and very high cycle regimes. Materials, 2020, 13: 68
29 Zhao J, Zhang S, Wan J, et al. Development of *in situ* fatigue performance testing apparatus for materials under coupling conditions of high-temperature and combined mechanical loads. IEEE Trans Instrum Meas, 2021, 70: 1–14
30 Mayer H, Fitzka M, Schuller R. Variable amplitude loading of Al 2024-T351 at different load ratios using ultrasonic equipment. Int J Fatigue, 2014, 60: 34–42
31 Yi J Z, Torbet C J, Feng Q, et al. Ultrasonic fatigue of a single crystal Ni-base superalloy at 1000°C. Mater Sci Eng-A, 2007, 443: 142–149
32 Holper B, Mayer H, Vasudevan A, et al. Near threshold fatigue crack growth in aluminium alloys at low and ultrasonic frequency: Influences of specimen thickness, strain rate, slip behaviour and air humidity. Int J Fatigue, 2003, 25: 397–411
33 Geathers J, Torbet C J, Jones J W, et al. Investigating environmental effects on small fatigue crack growth in Ti-6242S using combined ultrasonic fatigue and scanning electron microscopy. Int J Fatigue, 2015, 70: 154–162
34 Schönbauer B M, Stanzl-Tschegg S E, Perlega A, et al. Fatigue life estimation of pitted 12% Cr steam turbine blade steel in different environments and at different stress ratios. Int J Fatigue, 2014, 65: 33–43
35 Mayer H. Recent developments in ultrasonic fatigue. Fatigue Fract Eng Mat Struct, 2016, 39: 3–29
36 Wöhler A. Bericht über die Versuche, welche auf der Königl. NiederschlesischMärkischen Eisenbahn mit Apparaten zum Messen der Biegung und Verdrehung von Eisenbahn-wagen-Achsen während der Fahrt, angestellt wurden. Zeitschrift fur Bauwwesen. 1858, 8: 642–651
37 Lu L, Shiozawa K. Effect of surface treatment on super-long-life fatigue behavior in high speed tool steel, JIS SKH51. TransJSME SerA, 2003, 69: 1195–1202
38 Lu LT, Shiozawa K, Jiang Y. Influence of deeply rolling process on ultra-long life fatigue behavior of high carbon-chromium bearing steel. Acta Metallurgica Sinica, 2006, 42: 515–520
39 Shiozawa K, Lu L T. Internal fatigue failure mechanism of high strength steels in gigacycle regime. KEM, 2008, 378–379: 65–80
40 Shiozawa K, Murai M. Axial loading fatitgue properties of low alloy steel, SNCM439, in very high cycle regime. Trans JSME SerA, 2008, 74: 885–893
41 Shiozawa K, Kashiwagi T, Murai T, et al. Gigacycle fatigue behaviour and fractography of extruded AZ80 magnesium alloy. JSMET, 2009, 75: 733–741
42 Li W, Sakai T, Wakita M, et al. Influence of microstructure and surface defect on very high cycle fatigue properties of clean spring steel. Int J Fatigue, 2014, 60: 48–56
43 Li W, Sakai T, Wang P. Influence of microstructural inhomogeneity and residual stress on very high cycle fatigue property of clean spring steel. J Materi Eng Perform, 2013, 22: 2594–2601
44 Goto M, Yamamoto T, Nisitani H, et al. Effect of removing surface hardened layer on the fatigue strength of bearing steel SUJ2 ground specimen in the long life field.. J Soc Mater Sci Jpn, 2000, 49: 786–792
45 Takeda M, Sakai T, Oguma N. Rotating bending fatigue property and fractography for high strength steels and carbon steel over ultra wide life region.. TransJSME SerA, 2002, 68: 977–984
46 Ha T K, Jeong H T, Sung H J. High temperature bending fatigue behavior of stainless steels for automotive exhaust. J Mater Process Tech, 2007, 187-188: 555–558
47 Chanyathunyaroj K, Moonrin N, Laungsopapun G, et al. Corrosion fatigue study of 6061 aluminum alloy: The effect of coatings on the fatigue characteristics. Metall Mater Trans A, 2022, 53: 2874–2889
48 ISO. Metallic materials—Rotating bar bending fatigue testing. 2021
49 Wan J, Zhao J, Zhou L, et al. A novel methodology for bending

ultrasonic fatigue testing in the VHCF regime. Int J Fatigue, 2023, 170: 107562
50 Bai Y, Yue H, Wang J, et al. Super-durable ultralong carbon nanotubes. Science, 2020, 369: 1104–1106
51 Muhlstein C L, Brown S B, Ritchie R O. High-cycle fatigue of single-crystal silicon thin films. J Microelectromech Syst, 2001, 10: 593–600
52 Pierron O N, Abnet C C, Muhlstein C L. Methodology for low- and high-cycle fatigue characterization with kHz-frequency resonators. Sens Actuat A-Phys, 2006, 128: 140–150
53 Fehr RO SC. Resonant vibration testing. Steel, 1941, 109: 64–65, 96, 102
54 Milošević I, Renhart P, Winter G, et al. A new high frequency testing method for steels under tension/compression loading in the VHCF regime. Int J Fatigue, 2017, 104: 150–157
55 Hu D, Meng F, Liu H, et al. Experimental investigation of fatigue crack growth behavior of GH2036 under combined high and low cycle fatigue. Int J Fatigue, 2016, 85: 1–10
56 Hu D, Yang Q, Liu H, et al. Crack closure effect and crack growth behavior in GH2036 superalloy plates under combined high and low cycle fatigue. Int J Fatigue, 2017, 95: 90–103
57 Li Z, Xu H, Shi D, et al. Combined tensile and bending fatigue behavior and failure mechanism of a blade-like specimen at elevated temperature. Int J Fatigue, 2022, 164: 107163
58 Han L, Wang Y, Zhang Y, et al. Competitive cracking behavior and microscopic mechanism of Ni-based superalloy blade respecting accelerated CCF failure. Int J Fatigue, 2021, 150: 106306
59 Hu D, Yan L, Gao Y, et al. Crack growth behavior of full-scale turbine attachment under combined high and low cycle fatigue. J Eng Gas Turbines Power, 2019, 141
60 Han L, Huang D, Yan X, et al. Combined high and low cycle fatigue life prediction model based on damage mechanics and its application in determining the aluminized location of turbine blade. Int J Fatigue, 2019, 127: 120–130
61 Ding X, Huang D, Yan X, et al. Effect of pneumatic shot peening on the high and low cycle combined fatigue life of K403 turbine blades. Fatigue Fract Eng Mat Struct, 2021, 44: 1439–1454
62 Chen C, Yan X, Zhang X, et al. Effect of aluminized coating on combined low and high cycle fatigue life of turbine blade at elevated temperature. J Eng Gas Turbines Power, 2019, 141
63 Wang R, Wei J, Hu D, et al. Investigation on experimental load spectrum for high and low cycle combined fatigue test. Propulsion Power Res, 2013, 2: 235–242
64 Yakui Z, Shuxiang G. Research on the fatigue performance of TC6 compressor blade under the CCF effect. Int J Aerospace Eng, 2018, 2018: 1–10
65 Villasante M. Predictive methods for combined cycle fatigue in gas turbine blades. Aerodays, 2011, 30: 1–8
66 Rawlins R E. Fatigue tests at resonant speed. Metal Prog, 1947, 47: 265–267
67 Zimmermann M, Christ H. Experimentelle Herausforderungen bei der Versuchsführung zur Charakterisierung des Ermüdungsverhaltens im Übergang von HCF zu VHCF. Konstruktion, Qualitätssicherung und Schadensanalyse, Herausgeber: M Pohl, Verlag Stahleisen GmbH, Düsseldorf. 2007, 385–391
68 Ritchie R O, Boyce B L, Campbell J P, et al. Thresholds for high-cycle fatigue in a turbine engine Ti-6Al-4V alloy. Int J Fatigue, 1999, 21: 653–662
69 Campbell J P, Ritchie R O. Mixed-mode, high-cycle fatigue-crack growth thresholds in Ti-6Al-4V. Eng Fract Mech, 2000, 67: 209–227
70 Campbell J P, Ritchie R O. Mixed-mode, high-cycle fatigue-crack growth thresholds in Ti-6Al-4V. Eng Fract Mech, 2000, 67: 229–249
71 Hill B D. Calibration procedure for DIC strain measurements during vibration-based fatigue testing. Salt lake: Utah State University, 2022
72 Bruns J, Zearley A, George T, et al. Vibration-based bending fatigue of a hybrid insert-plate system. Exp Mech, 2015, 55: 1067–1080
73 Xu W, Yang X, Zhong B, et al. Multiaxial fatigue investigation of titanium alloy annular discs by a vibration-based fatigue test. Int J Fatigue, 2017, 95: 29–37
74 Hu H T, Li Y L, Suo T, et al. Fatigue behavior of aluminum stiffened plate subjected to random vibration loading. Trans Nonferrous Met Soc China, 2014, 24: 1331–1336
75 Ellyson B, Brochu M, Brochu M. Characterization of bending vibration fatigue of SLM fabricated Ti-6Al-4V. Int J Fatigue, 2017, 99: 25–34
76 Ellyson B, Chekir N, Brochu M, et al. Characterization of bending vibration fatigue of WBD fabricated Ti-6Al-4V. Int J Fatigue, 2017, 101: 36–44
77 Česnik M, Slavič J, Boltežar M. Uninterrupted and accelerated vibrational fatigue testing with simultaneous monitoring of the natural frequency and damping. J Sound Vib, 2012, 331: 5370–5382
78 Capponi L, Česnik M, Slavič J, et al. Non-stationarity index in vibration fatigue: Theoretical and experimental research. Int J Fatigue, 2017, 104: 221–230
79 Xu W, Yang X, Zhong B, et al. Failure criterion of titanium alloy irregular sheet specimens for vibration-based bending fatigue testing. Eng Fract Mech, 2018, 195: 44–56
80 Furman B A, Hill B D, German E E, et al. Shape optimization of rectangular plates for vibration-based fatigue testing. J Appl Mech, 2021, 88
81 Scott-Emuakpor O, Shen M H H, George T, et al. Development of an improved high cycle fatigue criterion. J Eng Gas Turbines Power, 2007, 129: 162–169
82 Yun G J, Abdullah A B M, Binienda W. Development of a closed-loop high-cycle resonant fatigue testing system. Exp Mech, 2012, 52: 275–288
83 Xu W, Chen X, Gao Z, et al. Fatigue behaviors of a titanium alloy in the VHCF regime based on a vibration-based bending fatigue test. Fatigue Fract Eng Mat Struct, 2022, 45: 2549–2562
84 Mitsche R, Stanzl S, Burkert D. Hochfrequenzkinematographie in der Metallforschung. Wissenschaftlicher Film. 1973, 14: 10
85 Yazdian A, Karafi M R. An analytical approach to design horns and boosters of ultrasonic welding machines. SN Appl Sci, 2022, 4: 166
86 Matikas T E. Specimen design for fatigue testing at very high frequencies. J Sound Vib, 2001, 247: 673–681
87 Bajons P, Kromp W. Determination of magnification and resonance length of samples used in ultrasonic fatigue tests. Ultrasonics, 1978, 16: 213–217
88 McMillan T J. The design and implementation of an ultra high cycle fatigue testing machine. Johannesburg: University of the Witwatersrand, 2015
89 Bathias C, Paris P C. Gigacycle Fatigue in Mechanical Practice. Boca Raton: CRC Press, 2004
90 Shabani P, Taheri-Behrooz F, Samareh-Mousavi S S, et al. Very high cycle and gigacycle fatigue of fiber-reinforced composites: A review on experimental approaches and fatigue damage mechanisms. Prog Mater Sci, 2021, 118: 100762
91 Backe D, Balle F, Eifler D. Fatigue testing of CFRP in the very high cycle fatigue (VHCF) regime at ultrasonic frequencies. Compos Sci Tech, 2015, 106: 93–99
92 Backe D, Balle F. Ultrasonic fatigue and microstructural characterization of carbon fiber fabric reinforced polyphenylene sulfide in the very high cycle fatigue regime. Compos Sci Tech, 2016, 126: 115–121
93 Backe D, Balle F, Helfen T, et al. Ultrasonic fatigue testing system combined with online nondestructive testing for carbon fiber reinforced composites. Supplemental Proceedings: Materials Properties, Characterization, and Modeling. 2012, 1: 855–862
94 Weibel D, Balle F, Backe D. Ultrasonic fatigue of CFRP-experimental principle, damage analysis and very high cycle fatigue properties. KEM, 2017, 742: 621–628
95 Ding J, Cheng L. Experimental study on ultrasonic three-point bending fatigue of CFRP under ultraviolet radiation. Eng Fract Mech, 2021, 242: 107435

96 Balle F, Backe D. Very high cycle fatigue of carbon fiber reinforced polyphenylene sulfide at ultrasonic frequencies. In: Christ H J, eds. Fatigue of Materials at Very High Numbers of Loading Cycles. Berlin: Springer, 2018. 441–461
97 Wan J, Zhao J, Song M, et al. Free and steady-state forced vibrations of a base-excited nonuniform cantilever Timoshenko beam with internal damping. Acta Mech, 2022, 233: 4209–4229
98 Meirovitch L. Analytical Methods in Vibrations, McMillan Pub. Co. Inc. New York, 1967
99 Sorrentino S, Fasana A, Marchesiello S. Analysis of non-homogeneous Timoshenko beams with generalized damping distributions. J Sound Vib, 2007, 304: 779–792
100 Song Y N, Wang H D, Xu B S, et al. Effect of fretting wear on very high cycle bending fatigue behaviors of FV520B steel. Tribol Int, 2016, 103: 132–138
101 Jiao S, Gao C, Cheng L, et al. A very high-cycle fatigue test and fatigue properties of TC17 titanium alloy. J Materi Eng Perform, 2016, 25: 1085–1093
102 Ghadimi H, Jirandehi A P, Nemati S, et al. Small-sized specimen design with the provision for high-frequency bending-fatigue testing. Fatigue Fract Eng Mat Struct, 2021, 44: 3517–3537
103 Kou H J, Lin J S, Zhang J H, et al. Dynamic and fatigue compressor blade characteristics during fluid-structure interaction: Part I—Blade modelling and vibration analysis. Eng Fail Anal, 2017, 76: 80–98
104 Stanzl-Tschegg S E, Mayer H R, Tschegg E K. High frequency method for torsion fatigue testing. Ultrasonics, 1993, 31: 275–280
105 Mayer H, Schuller R, Karr U, et al. Cyclic torsion very high cycle fatigue of VDSiCr spring steel at different load ratios. Int J Fatigue, 2015, 70: 322–327
106 Mayer H, Schuller R, Karr U, et al. Mean stress sensitivity and crack initiation mechanisms of spring steel for torsional and axial VHCF loading. Int J Fatigue, 2016, 93: 309–317
107 Karr U, Schönbauer B, Fitzka M, et al. Inclusion initiated fracture under cyclic torsion very high cycle fatigue at different load ratios. Int J Fatigue, 2019, 122: 199–207
108 Karr U, Schönbauer B M, Sandaiji Y, et al. Influence of load ratio on torsion very high cycle fatigue of high-strength spring steel in the presence of detrimental defects. Fatigue Fract Eng Mat Struct, 2021, 44: 2356–2371
109 Marinesgarcia I, Doucet J P, Bathias C. Development of a new device to perform torsional ultrasonic fatigue testing. Int J Fatigue, 2007, 29: 2094–2101
110 Petit J, Jiang Z, Polit O, et al. Optimisation of an ultrasonic torsion fatigue system for high strength materials. Int J Fatigue, 2021, 151: 106395
111 Filgueiras P F, Bathias C, Palma E S, et al. Inducing very high cycle fretting-fatigue in the ultrasonic regime. Tribol Int, 2014, 76: 57–62
112 Lee Y L, Pan J, Hathaway R, et al. Fatigue Testing and Analysis: Theory and Practice. Oxford: Butterworth-Heinemann, 2005
113 Rajasekaran R, Nowell D. Fretting fatigue in dovetail blade roots: Experiment and analysis. Tribol Int, 2006, 39: 1277–1285
114 Tang H, Cao D, Yao H, et al. Fretting fatigue failure of an aero engine turbine blade. Eng Fail Anal, 2009, 16: 2004–2008
115 Murthy H, Garcia D B, Matlik J F, et al. Fretting fatigue of single crystal/polycrystalline nickel subjected to blade/disk contact loading. Acta Astronaut, 2005, 57: 1–9
116 Xu Z B, Peng J F, Liu J H, et al. Effect of contact pressure on torsional fretting fatigue damage of 316L austenitic stainless steel. Wear, 2017, 376–377: 680–689
117 Li Z Y, Liu X L, Wu G Q, et al. Observation of fretting fatigue cracks of Ti6Al4V titanium alloy. Mater Sci Eng-A, 2017, 707: 51–57
118 Mason W. Use of high amplitude strains in studying wear and ultrasonic fatigue in metals. Ultrasonic fatigue, 1982, 647–657
119 Teng Z, Liu H, Wang Q, et al. Fretting behaviors of a steel up to very high cycle fatigue. Wear, 2019, 438-439: 203078
120 Huang Z, Zhang Z, Teng Z, et al. Effect of fretting damage on characteristics of high strength bearing steel up to very high cycle fatigue. Eng Fract Mech, 2019, 217: 106526
121 Zhai Y, Huang Z Y, Zhu S P, et al. Very high cycle fretting fatigue damage and crack path investigation of Nimonic 80 A at elevated temperature. Int J Fatigue, 2020, 132: 105345
122 Song Y N, Xing Z G, Wang H D, et al. Very high cycle bending fatigue behaviors of FV520B steel under fretting wear. J Mater Res, 2016, 31: 1748–1754
123 Lukas P, Kunz L, Svoboda M. High-temperature ultra-high cycle fatigue damage of notched single crystal superalloys at high mean stresses. Int J Fatigue, 2005, 27: 1535–1540
124 Luo S, Wu S. Fatigue failure analysis of rotor compressor blades concerning the effect of rotating stall and surge. Eng Fail Anal, 2016, 68: 1–9
125 Nikitin A D, Stratula B A, Publishing I O P, et al. Analytical and numerical study of biaxial bending on VHCF testing machine. In: Proceedings of the 22nd Winter School on Continuous Media Mechanics (WSCMM). Ural, 2021
126 da Costa P R, Soares H, Reis L, et al. Ultrasonic fatigue testing under multiaxial loading on a railway steel. Int J Fatigue, 2020, 136: 105581
127 Liu Q. Manufacturing Technology and Failure Analysis of Aero-engine Titanium Alloy Blades. Beijing: Aviation Industry Press, 2018
128 Liu C, Zhao H, Ma Z, et al. Novel instrument for characterizing comprehensive physical properties under multi-mechanical loads and multi-physical field coupling conditions. Rev Sci Instrum, 2018, 89
129 Nam K W, Ando K, Ogura N, et al. Fatigue life and penetration behaviour of a surface-cracked plate under combined tension and bending. Fatigue Fract Eng Mat Struct, 1994, 17: 873–882
130 Zhao J, Wan J, Liu C, et al. The study on *in situ* asymmetric bending behavior of structural bamboo materials under combined tension-bending loads. J Mater Sci, 2022, 57: 17304–17324
131 Wang B, Cheng L, Cui W, et al. Effect of forging process on high cycle and very high cycle fatigue properties of TC4 titanium alloy under three-point bending. Fatigue Fract Eng Mat Struct, 2021, 44: 2054–2069
132 Gaenser H P. Some notes on gradient, volumetric and weakest link concepts in fatigue. Comput Mater Sci, 2008, 44: 230–239
133 Wozney G P. Resonant-vibration fatigue testing. Exp Mech, 1962, 2: 1–8
134 French R F. Mechanical evaluation of gas-turbine blades in their actual centrifugal field. Exp Mech, 1962, 2: 122–128
135 Wang B, Cheng L, Ding J, et al. Effects of geometric parameters and axial tension on vibration characteristics. J of Phys: Confer Ser, 2020, IOP Publishing, doi: 10.1088/1742-6596/1637/1/012049
136 Montalvão D, Wren A. Redesigning axial-axial (biaxial) cruciform specimens for very high cycle fatigue ultrasonic testing machines. Heliyon, 2017, 3: e00466
137 Costa P R, Montalvão D, Freitas M, et al. Cruciform specimens' experimental analysis in ultrasonic fatigue testing. Fatigue Fract Eng Mat Struct, 2019, 42: 2496–2508
138 da Costa P R, Reis L, Montalvão D, et al. A new method for ultrasonic fatigue testing of equibiaxial and pure shear cruciform specimens. Int J Fatigue, 2021, 152: 106423
139 Nwawe R, Grasso M, Chen Y, et al. Optimisation of a gigacycle biaxial fatigue specimen for ultrasonic testing. In: Proceedings of the Engineering and Computer Science Research Conference. Hatfield, 2019
140 Kaul H. Statistische Erhebungen über Betriebsbeanspruchungen von Flugzeugflügeln. Jahrbuch der Deutschen Luftfahrtforschung, Ergänzungsband. 1938, 307–313
141 Gaßner E. Festigkeitsversuche mit wiederholter Beanspruchung im Flugzeugbau. Luftwissen. 1939, 6: 61–64
142 Bhattacharyya M, Dureisseix D, Faverjon B. A unified approach based on temporal homogenisation and cycle jump for thermo-mechanical combined cycle fatigue. Int J Fatigue, 2020, 131: 105320
143 Qiu S, Cui H, Zhang H, et al. A dual-threshold modelling approach for fatigue life prediction under combined high and low cycle fatigue.

Int J Fatigue, 2022, 164: 107110
144 Dungey C, Bowen P. The effect of combined cycle fatigue upon the fatigue performance of TI-6AL-4V fan blade material. J Mater Process Tech, 2004, 153-154: 374–379
145 Filippini M, Foletti S, Pasquero G. Combined cycle fatigue of gas turbine blade materials at elevated temperature. Strain, 2010, 46: 374–381
146 Matikas T E. A high-cycle fatigue apparatus at 20 kHz for low-cycle fatigue/high-cycle fatigue interaction testing. Fatigue Fract Eng Mat Struct, 2001, 24: 687–697
147 Arcari A, Apetre N, Dowling N, et al. Variable amplitude fatigue life in VHCF and probabilistic life predictions. Procedia Eng, 2015, 114: 574–582
148 Meischel M, Stanzl-Tschegg S E, Arcari A, et al. Constant and variable-amplitude loading of aluminum alloy 7075 in the VHCF regime. Procedia Eng, 2015, 101: 501–508
149 Stanzl-Tschegg S E, Meischel M, Arcari A, et al. Combined cycle fatigue of 7075 aluminum alloy-fracture surface characterization and short crack propagation. Int J Fatigue, 2016, 91: 352–362
150 Cervellon A, Cormier J, Mauget F, et al. VHCF life evolution after microstructure degradation of a Ni-based single crystal superalloy. Int J Fatigue, 2017, 104: 251–262
151 Zhang Z, Teng Z, Wang J, et al. Very high cycle fatigue behaviors of GH4169 superalloy at room and high temperatures. Fatigue Fract Eng Mat Struct, 2022, 45: 1796–1806
152 Cervellon A, Hémery S, Kürnsteiner P, et al. Crack initiation mechanisms during very high cycle fatigue of Ni-based single crystal superalloys at high temperature. Acta Mater, 2020, 188: 131–144
153 Liu F, Chen Y, He C, et al. Tensile and very high cycle fatigue behaviors of a compressor blade titanium alloy at room and high temperatures. Mater Sci Eng-A, 2021, 811: 141049
154 Schöne S, Schettler S, Kuczyk M, et al. VHCF behavior of inconel 718 in different heat treatment conditions in a hot air environment. Metals, 2022, 12: 1062
155 Geathers J. Investigating microstructural and environmental effects on the very high cycle fatigue behavior of Ti-6242S. Dissertation for Doctoral Degree. 2Ann Arbor: University of Michigan, 2016
156 Holper B, Mayer H, Vasudevan A, et al. Near threshold fatigue crack growth at positive load ratio in aluminium alloys at low and ultrasonic frequency: Influences of strain rate, slip behaviour and air humidity. Int J Fatigue, 2004, 26: 27–38
157 Schönbauer B M, Perlega A, Karr U P, et al. Pit-to-crack transition under cyclic loading in 12% Cr steam turbine blade steel. Int J Fatigue, 2015, 76: 19–32
158 Ebara R. Corrosion fatigue in practical problems. Comp and Exp Fract Mech UK: Comp Mech Publ. 1994: 347–376
159 Pu X, Petit J, Darbord-Ranc I, et al. Thermal response of iron and C-Mn steels with different ferrite/pearlite phase fraction under ultrasonic fatigue loading. Mater Sci Eng-A, 2019, 749: 96–105
160 Tan K, Postel V, Liu Y, et al. Development of a photomicroscope method for *in situ* damage monitoring under ultrasonic fatigue test. IJSI, 2022, 13: 237–250
161 Merah N. Detecting and measuring flaws using electric potential techniques. J Qual Maint Eng, 2003, 9: 160–175
162 Na S, Yoon D, Kim J, et al. An evaluation of the fatigue crack propagation rate for powder metallurgical nickel-based superalloys using the DCPD method at elevated temperatures. Int J Fatigue, 2017, 101: 27–35
163 Shrestha S, Kannan M, Morscher G N, et al. *In-situ* fatigue life analysis by modal acoustic emission, direct current potential drop and digital image correlation for steel. Int J Fatigue, 2021, 142: 105924
164 Shrestha S, El Rassi J, Kannan M, et al. Fracture toughness and fatigue crack growth rate properties of AM repaired Ti-6Al-4V by direct energy deposition. Mater Sci Eng-A, 2021, 823: 141701
165 Ramachandran, N, Arakere, N, Goswami, T. Recording of elevated temperature fatigue crack growth data by DCPD system. High Temp Mater Processes, 2000, 19: 357–370
166 Elayeb A A, Grbović A, Kastratović G, et al. Fatigue crack growth in a structure exposed to high temperature. Eng Fail Anal, 2021, 127: 105493
167 Müller T, Sander M. On the use of ultrasonic fatigue testing technique—Variable amplitude loadings and crack growth monitoring. Ultrasonics, 2013, 53: 1417–1424
168 Chai M, Zhang Z, Duan Q. A new qualitative acoustic emission parameter based on Shannon's entropy for damage monitoring. Mech Syst Signal Proc, 2018, 100: 617–629
169 Al-Jumaili S K, Eaton M J, Holford K M, et al. Characterisation of fatigue damage in composites using an acoustic emission parameter correction technique. Compos Part B-Eng, 2018, 151: 237–244
170 Morton T M, Harrington R M, Bjeletich J G. Acoustic emissions of fatigue crack growth. Eng Fract Mech, 1973, 5: 691–697
171 Pascoe J A, Zarouchas D S, Alderliesten R C, et al. Using acoustic emission to understand fatigue crack growth within a single load cycle. Eng Fract Mech, 2018, 194: 281–300
172 Vshivkov A N, Iziumova A Y, Panteleev I A, et al. The study of a fatigue crack propagation in titanium Grade 2 using analysis of energy dissipation and acoustic emission data. Eng Fract Mech, 2019, 210: 312–319
173 Shiwa M, Furuya Y, Yamawaki H, et al. Fatigue process evaluation of ultrasonic fatigue testing in high strength steel analyzed by acoustic emission and non-linear ultrasonic. Mater Trans, 2010, 51: 1404–1408
174 Seleznev M, Weidner A, Biermann H, et al. Novel method for *in situ* damage monitoring during ultrasonic fatigue testing by the advanced acoustic emission technique. Int J Fatigue, 2021, 142: 105918
175 Yost W T, Cantrell J H. The effects of fatigue on acoustic nonlinearity in aluminum alloys. In: Proceedings of the IEEE 1992 Ultrasonics Symposium Proceedings. Tucson, 1992
176 Na J K, Cantrell J H, Yost W T. Linear and nonlinear ultrasonic properties of fatigued 410CB stainless steel. Review of progress in quantitative nondestructive evaluation, Springer, 1996. 1347–1352
177 Barnard D J, Dace G E, Buck O. Acoustic harmonic generation due to thermal embrittlement of inconel 718. J Nondestruct Eval, 1997, 16: 67–75
178 Kim J Y, Jacobs L J, Qu J, et al. Experimental characterization of fatigue damage in a nickel-base superalloy using nonlinear ultrasonic waves. J Acoust Soc Am, 2006, 120: 1266–1273
179 Kumar A, Torbet C J, Jones J W, et al. Nonlinear ultrasonics for *in situ* damage detection during high frequency fatigue. J Appl Phys, 2009, 106
180 Kumar A, Torbet C J, Pollock T M, et al. In situ characterization of fatigue damage evolution in a cast Al alloy via nonlinear ultrasonic measurements. Acta Mater, 2010, 58: 2143–2154
181 Herrmann J, Kim J Y, Jacobs L J, et al. Assessment of material damage in a nickel-base superalloy using nonlinear Rayleigh surface waves. J Appl Phys, 2006, 99: 124913
182 Frouin J, Matikas T E, Na J K, et al. *In-situ* monitoring of acoustic linear and nonlinear behavior of titanium alloys during cycling loading. In: Proceedings of the Nondestructive Evaluation of Aging Materials and Composites. Newport, 1999
183 Cantrell J H, Yost W T. Nonlinear ultrasonic characterization of fatigue microstructures. Int J Fatigue, 2001, 23: 487–490
184 Mayer H, Fitzka M, Schuller R. Constant and variable amplitude ultrasonic fatigue of 2024-T351 aluminium alloy at different load ratios. Ultrasonics, 2013, 53: 1425–1432
185 Fitzka M, Mayer H, Schuller R, et al. Variable amplitude loading of spray-formed hypereutectic aluminium silicon alloy DISPAL® S232 in the VHCF regime. Fatigue Fract Eng Mat Struct, 2014, 37: 945–957
186 Heinz S, Balle F, Wagner G, et al. Analysis of fatigue properties and failure mechanisms of Ti6Al4V in the very high cycle fatigue regime using ultrasonic technology and 3D laser scanning vibrometry. Ultrasonics, 2013, 53: 1433–1440

187 Yang W, Guo X, Guo Q, et al. Rapid evaluation for high-cycle fatigue reliability of metallic materials through quantitative thermography methodology. Int J Fatigue, 2019, 124: 461–472
188 Luong M P. Fatigue limit evaluation of metals using an infrared thermographic technique. Mech Mater, 1998, 28: 155–163
189 La Rosa G, Risitano A. Thermographic methodology for rapid determination of the fatigue limit of materials and mechanical components. Int J Fatigue, 2000, 22: 65–73
190 Micone N, De Waele W. On the application of infrared thermography and potential drop for the accelerated determination of an S-N curve. Exp Mech, 2017, 57: 143–153
191 Yan Z F, Zhang H X, Wang W X, et al. Temperature evolution and fatigue life evaluation of AZ31B magnesium alloy based on infrared thermography. Trans Nonferrous Met Soc China, 2013, 23: 1942–1948
192 Wagner D, Ranc N, Bathias C, et al. Fatigue crack initiation detection by an infrared thermography method. Fatigue Fract Eng Mat Struct, 2010, 33: 12–21
193 Xue H, Wagner D, Ranc N, et al. Thermographic analysis in ultrasonic fatigue tests. Fatigue Fract Eng Mat Struct, 2006, 29: 573–580
194 Krewerth D, Lippmann T, Weidner A, et al. Application of full-surface view *in situ* thermography measurements during ultrasonic fatigue of cast steel G42CrMo4. Int J Fatigue, 2015, 80: 459–467
195 Naoe T, Xiong Z, Futakawa M. Temperature measurement for *in-situ* crack monitoring under high-frequency loading. J Nucl Mater, 2018, 506: 12–18
196 Withers P J, Preuss M. Fatigue and damage in structural materials studied by X-Ray tomography. Annu Rev Mater Res, 2012, 42: 81–103
197 Liu L, Husseini N S, Torbet C J, et al. In situ imaging of high cycle fatigue crack growth in single crystal nickel-base superalloys by synchrotron X-radiation. J Eng Mater Tech, 2008, 130
198 Liu L, Husseini N S, Torbet C J, et al. In situ synchrotron X-ray imaging of high-cycle fatigue crack propagation in single-crystal nickel-base alloys. Acta Mater, 2011, 59: 5103–5115
199 Istomin K, Dönges B, Schell N, et al. Analysis of VHCF damage in a duplex stainless steel using hard X-ray diffraction techniques. Int J Fatigue, 2014, 66: 177–182
200 Messager A, Junet A, Palin-Luc T, et al. *In situ* synchrotron ultrasonic fatigue testing device for 3D characterisation of internal crack initiation and growth. Fatigue Fract Eng Mat Struct, 2020, 43: 558–567
201 Ors T, Ranc N, Pelerin M, et al. Microsecond time-resolved X-ray diffraction for the investigation of fatigue behavior during ultrasonic fatigue loading. J Synchrotron Rad, 2019, 26: 1660–1670
202 Liu L, Hou N, Li B, et al. Structure characterization within the vicinity of the fine granular area by synchrotron radiation nano-CT. Fatigue Fract Eng Mat Struct, 2020, 43: 1597–1605
203 Su Y, Han Q N, Qiu W, et al. High temperature *in-situ* SEM observation and crystal plasticity simulation on fretting fatigue of Ni-based single crystal superalloys. Int J Plast, 2020, 127: 102645
204 Kong Y, Bennett C J, Hyde C J. A review of non-destructive testing techniques for the *in-situ* investigation of fretting fatigue cracks. Mater Des, 2020, 196: 109093
205 Jacquemain V, Ranc N, Cheuleu C, et al. Estimation of stress in specimens loaded with ultrasonic fatigue machines. Int J Fatigue, 2021, 153: 106474
206 Premanand A, Balle F. Influence of pulse-pause sequences on the self-heating behavior in continuous carbon fiber-reinforced composites under ultrasonic cyclic three-point bending loads. Materials, 2022, 15: 3527
207 Peng W, Zhang Y, Qiu B, et al. A brief review of the application and problems in ultrasonic fatigue testing. In: Proceedings of the AASRI Conference on Power and Energy Systems (PES). Hong Kong, 2012
208 Sun C, Song Q, Hu Y, et al. Effects of intermittent loading on fatigue life of a high strength steel in very high cycle fatigue regime. Int J Fatigue, 2018, 117: 9–12
209 Zhao Z, Zhang F, Dong C, et al. Initiation and early-stage growth of internal fatigue cracking under very-high-cycle fatigue regime at high temperature. Metall Mater Trans A, 2020, 51: 1575–1592
210 Bach J, Höppel H W, Bitzek E, et al. Influence of specimen geometry on temperature increase during ultrasonic fatigue testing. Ultrasonics, 2013, 53: 1412–1416
211 Liu X, Sun C, Hong Y. Effects of stress ratio on high-cycle and very-high-cycle fatigue behavior of a Ti-6Al-4V alloy. Mater Sci Eng-A, 2015, 622: 228–235
212 Yang K, He C, Huang Q, et al. Very high cycle fatigue behaviors of a turbine engine blade alloy at various stress ratios. Int J Fatigue, 2017, 99: 35–43
213 Muhammad M, Frye P, Simsiriwong J, et al. An investigation into the effects of cyclic strain rate on the high cycle and very high cycle fatigue behaviors of wrought and additively manufactured Inconel 718. Int J Fatigue, 2021, 144: 106038
214 Flore D, Wegener K, Mayer H, et al. Investigation of the high and very high cycle fatigue behaviour of continuous fibre reinforced plastics by conventional and ultrasonic fatigue testing. Compos Sci Tech, 2017, 141: 130–136
215 Lee C S, Kim H J, Amanov A, et al. Investigation on very high cycle fatigue of PA66-GF30 GFRP based on fiber orientation. Compos Sci Tech, 2019, 180: 94–100
216 Furuya Y, Kobayashi K, Hayakawa M, et al. High-temperature ultrasonic fatigue testing of single-crystal superalloys. Mater Lett, 2012, 69: 1–3
217 Reis L, Da Costa P R, Pereira R, et al. Crack path and fracture surface analysis of ultrasonic fatigue testing under multiaxial loadings. Eng Fail Anal, 2022, 142: 106785
218 Torabian N, Favier V, Dirrenberger J, et al. Correlation of the high and very high cycle fatigue response of ferrite based steels with strain rate-temperature conditions. Acta Mater, 2017, 134: 40–52
219 Schneider N, Bödecker J, Berger C, et al. Frequency effect and influence of testing technique on the fatigue behaviour of quenched and tempered steel and aluminium alloy. Int J Fatigue, 2016, 93: 224–231
220 Papakyriacou M, Mayer H, Plenk Jr H, et al. Cyclic plastic deformation of tantalum and niobium at very high numbers of cycles. Mater Sci Eng-A, 2002, 325: 520–524
221 Papakyriacou M, Mayer H, Pypen C, et al. Influence of loading frequency on high cycle fatigue properties of b.c.c. and h.c.p. metals. Mater Sci Eng-A, 2001, 308: 143–152
222 Tsutsumi N, Murakami Y, Doquet V. Effect of test frequency on fatigue strength of low carbon steel. Fatigue Fract Eng Mat Struct, 2009, 32: 473–483
223 Nonaka I, Setowaki S, Ichikawa Y. Effect of load frequency on high cycle fatigue strength of bullet train axle steel. Int J Fatigue, 2014, 60: 43–47
224 Milošević I, Renhart P, Winter G, et al. Validation of a new high frequency testing technique in the VHCF regime—Fatigue properties of a 42CrMoS4 and X5CrNiCuNb16-4 steel. Int J Fatigue, 2018, 112: 198–205
225 Takeuchi E, Furuya Y, Nagashima N, et al. The effect of frequency on the giga-cycle fatigue properties of a Ti-6Al-4V alloy. Fatigue Fract Eng Mat Struct, 2008, 31: 599–605
226 Chen Q, Kawagoishi N, Wang Q Y, et al. Small crack behavior and fracture of nickel-based superalloy under ultrasonic fatigue. Int J Fatigue, 2005, 27: 1227–1232
227 Furuya Y, Matsuoka S, Abe T, et al. Gigacycle fatigue properties for high-strength low-alloy steel at 100 Hz, 600 Hz, and 20 kHz. Scripta Mater, 2002, 46: 157–162
228 Abe T, Furuya Y, Matsuoka S. 10^{10}-cycle Fatigue Properties for SUP7 Spring Steels Tempered at 430 and 500°C. Tetsu-to-Hagane, 2002, 88: 786–792
229 Furuya Y, Hirukawa H, Takeuchi E. Gigacycle fatigue in high strength steels. Sci Tech Adv Mater, 2019, 20: 643–656
230 Hong Y, Hu Y, Zhao A. Effects of loading frequency on fatigue

behavior of metallic materials—A literature review. Fatigue Fract Eng Mat Struct, 2023, 46: 3077–3098
231 Kuguel R. A relation between theoretical stress concentration factor and fatigue notch factor deduced from the concept of highly stressed volume. ASTM Proc, 1961
232 Aigner R, Pomberger S, Leitner M, et al. On the statistical size effect of cast aluminium. Materials, 2019, 12: 1578
233 Alava M J, Nukala P K V V, Zapperi S. Size effects in statistical fracture. J Phys D-Appl Phys, 2009, 42: 214012
234 Wang W, Zhong Y, Lu K, et al. Size effects and strength fluctuation in nanoscale plasticity. Acta Mater, 2012, 60: 3302–3309
235 Fjeldstad A, Wormsen A, Härkegård G. Simulation of fatigue crack growth in components with random defects. Eng Fract Mech, 2008, 75: 1184–1203
236 El Khoukhi D, Morel F, Saintier N, et al. Experimental investigation of the size effect in high cycle fatigue: Role of the defect population in cast aluminium alloys. Int J Fatigue, 2019, 129: 105222
237 Böhm J. Zur Vorhersage von dauerschwingfestigkeiten ungekerbter und gekerbter Bauteile unter Berücksichtigung des statistichen Grösseneinflusses. Technische Universität München, 1980
238 Makkonen M. Notch size effects in the fatigue limit of steel. Int J Fatigue, 2003, 25: 17–26
239 Taylor D, Makkonen M. Comment on "Notch Size Effects in the Fatigue Limit of Steel" by M. Makkonen [Int J Fatigue 25 (2003) 17–26]. Int J Fatigue, 2003, 25: 779–780
240 Makkonen M. Response to comments by Prof. Taylor on "Notch Size Effects in the Fatigue Limit of Steel" by M. Makkonen [Int J Fatigue 25 (2003) 17–26]. Int J Fatigue, 2003, 25: 781–783
241 Leitner M, Garb C, Remes H, et al. Microporosity and statistical size effect on the fatigue strength of cast aluminium alloys EN AC-45500 and 46200. Mater Sci Eng-A, 2017, 707: 567–575
242 Shirani M, Härkegård G. Fatigue life distribution and size effect in ductile cast iron for wind turbine components. Eng Fail Anal, 2011, 18: 12–24
243 Phillips C E, Heywood R B. The Size Effect in Fatigue of Plain and Notched Steel Specimens Loaded under Reversed Direct Stress. Proc Institution Mech Engineers, 1951, 165: 113–124
244 Carpinteri A, Spagnoli A, Vantadori S. Size effect in S-N curves: A fractal approach to finite-life fatigue strength. Int J Fatigue, 2009, 31: 927–933
245 Liao D, Zhu S P, Keshtegar B, et al. Probabilistic framework for fatigue life assessment of notched components under size effects. Int J Mech Sci, 2020, 181: 105685
246 Furuya Y. Specimen size effects on gigacycle fatigue properties of high-strength steel under ultrasonic fatigue testing. Scripta Mater, 2008, 58: 1014–1017
247 Jeddi D, Palin-Luc T. A review about the effects of structural and operational factors on the gigacycle fatigue of steels. Fatigue Fract Eng Mat Struct, 2018, 41: 969–990
248 Zhu S P, Ai Y, Liao D, et al. Recent advances on size effect in metal fatigue under defects: A review. Int J Fract, 2022, 234: 21–43
249 Tridello A, Niutta C B, Berto F, et al. Size-effect in very high cycle fatigue: A review. Int J Fatigue, 2021, 153: 106462
250 Xue H, Sun Z, Zhang X, et al. Very high cycle fatigue of a cast aluminum alloy: Size effect and crack initiation. J Materi Eng Perform, 2018, 27: 5406–5416
251 Invernizzi S, Montagnoli F, Carpinteri A. Experimental evidence of specimen-size effects on EN-AW6082 aluminum alloy in VHCF regime. Appl Sci, 2021, 11: 4272
252 Peng W J, Xue H, Ge R, et al. The influential factors on very high cycle fatigue testing results. In: Proceedings of the 12th International Fatigue Congress (FATIGUE). Poitiers, 2018
253 Tridello A, Paolino D S, Rossetto M. Ultrasonic VHCF tests on very large specimens with risk-volume up to 5000 mm^3. Appl Sci, 2020, 10: 2210
254 Tridello A, Fiocchi J, Biffi C A, et al. Size-effects affecting the fatigue response up to 109 cycles (VHCF) of SLM AlSi10Mg specimens produced in horizontal and vertical directions. Int J Fatigue, 2022, 160: 106825
255 Furuya Y, Shimamura Y, Takanashi M, et al. Standardization of an ultrasonic fatigue testing method in Japan. Fatigue Fract Eng Mat Struct, 2022, 45: 2415–2420
256 Banhart J, Borbély A, Dzieciol K, et al. X-ray and neutron imaging—Complementary techniques for materials science and engineering. Int J Mater Res, 2010, 101: 1069–1079
257 LaManna J M, Hussey D S, Baltic E, et al. Neutron and X-ray Tomography (NeXT) system for simultaneous, dual modality tomography. Rev Sci Instrum, 2017, 88